



## 저작자표시-비영리-변경금지 2.0 대한민국

이용자는 아래의 조건을 따르는 경우에 한하여 자유롭게

- 이 저작물을 복제, 배포, 전송, 전시, 공연 및 방송할 수 있습니다.

다음과 같은 조건을 따라야 합니다:



저작자표시. 귀하는 원저작자를 표시하여야 합니다.



비영리. 귀하는 이 저작물을 영리 목적으로 이용할 수 없습니다.



변경금지. 귀하는 이 저작물을 개작, 변형 또는 가공할 수 없습니다.

- 귀하는, 이 저작물의 재이용이나 배포의 경우, 이 저작물에 적용된 이용허락조건을 명확하게 나타내어야 합니다.
- 저작권자로부터 별도의 허가를 받으면 이러한 조건들은 적용되지 않습니다.

저작권법에 따른 이용자의 권리는 위의 내용에 의하여 영향을 받지 않습니다.

이것은 [이용허락규약\(Legal Code\)](#)을 이해하기 쉽게 요약한 것입니다.

[Disclaimer](#)

공학박사 학위논문

**Development of Advanced Time-  
dependent Monte Carlo Neutron  
Transport Methods for Reactor  
Transient Analysis**

노심 과도해석을 위한 시간종속 몬테칼로 중성자  
수송해석법 고도화 개발

2022년 2월

서울대학교 대학원

에너지시스템공학부

장 상 훈

**Development of Advanced Time-dependent Monte  
Carlo Neutron Transport Methods for Reactor  
Transient Analysis**

노심 과도해석을 위한 시간종속 몬테칼로 중성자  
수송해석법 고도화 개발

지도 교수 심 형 진

이 논문을 공학박사 학위논문으로 제출함  
2022년 2월

서울대학교 대학원  
에너지시스템공학부  
장 상 훈

장상훈의 공학박사 학위논문을 인준함  
2022년 2월

위 원 장 \_\_\_\_\_ 김 은 희 (인)

부위원장 \_\_\_\_\_ 심 형 진 (인)

위 원 \_\_\_\_\_ 조 형 규 (인)

위 원 \_\_\_\_\_ 김 용 희 (인)

위 원 \_\_\_\_\_ 서 철 교 (인)

# Abstract

The analysis of the time-dependent neutron behavior is essential to understanding the kinetic properties of reactor cores in various application fields including reactor start-up analyses, reactivity measurements, accident analysis, and experiments in research reactors. Since the reactor transient analysis requires a lot of computational time compared to the steady-state analysis, it has mainly relied on deterministic or quasi-static methods. However, these methods can lead to inaccurate results due to inherent differential approximations to space, energy, or time domains. Recently, thanks to the ever-advancing computing power and the development of high-reliability methodologies, the time-dependent Monte Carlo (TDMC) neutron transport method without any approximation is being actively studied and has become an applicable alternative for reactor transient analysis in a practical time range. The development of Monte Carlo transient analysis method is very important because it can provide reference solutions for the transient analysis of various reactors such as gen-IV reactors and research reactors as well as commercial reactors. In domestic, McCARD, a Monte Carlo code developed by Seoul National University, has equipped with the capability of the TDMC simulation and performed alpha eigenvalue calculations and transient analysis. However, the existing code is limited to two-dimensional analysis and lacks the capability for an accurate and reliable reactor transient analysis such as an unbiased variance estimation. Therefore, motivated by the necessity of developing such high-reliability transient analysis code, this thesis aims to advance the TDMC algorithms for reactor transient analysis and to extend the applicability of the TDMC simulation to practical problems.

The TDMC method enables sustainable neutron simulation by introducing time intervals to the conventional Monte Carlo simulation, conducting time bin-by-bin neutron simulation, and then controlling the neutron population at the end of each time interval. In McCARD, the analog MC branching method that simulates the branching of particles as it is, and the combing method, which samples the exact number of neutrons without bias, are used as neutron population control methods. The efficiency of the algorithm is improved by removing the scale factor previously used for weight normalization and introducing a dynamic weight window. The

TDMC method which allows sustainable simulation of neutrons over time is applied to the PNS experiments to estimate the prompt neutron decay constant  $\alpha$ . In the PNS experiment, it has been reported that the different  $\alpha$  values are measured depending on the detector position and detection time due to the initial source and geometry effect. Utilizing the TDMC method which can accurately simulate the space- and time-dependent behavior of neutrons, an optimum detector position search algorithm is developed for the PNS  $\alpha$  measurement. The developed method is applied to the Pb-Bi-zoned experimental benchmark at KUCA and numerical experiments at AGN-201K. In the KUCA experimental benchmark, the spallation source effect is well reflected so the relative  $\alpha$  convergence at different detector positions is well predicted. As for the AGN-201K simulation, the sensitivity of the optimum detector position to the initial source location is evaluated. By comparing the detector signals at convergence times according to positions, the optimum detector position is determined where the detector signal is highest. The application results are expected to be a good reference for designing and performing actual PNS  $\alpha$  measurement experiments.

Along with the neutron population control method, the methodologically important parts of the reactor transient simulation are the delayed neutron simulation and the steady-state modeling. Since the prompt neutron and the delayed neutron have a large difference in generation time, the conventional method of directly sampling the delayed neutron from the fission event causes a large statistical error. In addition, a method that can simulate the distribution of the prompt neutron and delayed neutron sources in the initial steady-state is needed because most transient analysis starts from the steady-state. Therefore, the forced decay algorithm through precursor simulation is introduced for efficient delayed neutron simulation. As the initial steady-state modeling method, the TDMC steady-state simulation method is employed, which consistently uses the TDMC simulation method from the initial state to the transient state without changing the calculation mode. In this process, the algorithm for normalizing the initial number of precursors is improved, and a new feature of moving geometry treatment to deal with more realistic three-dimensional transient scenarios is developed. The developed McCARD transient analysis capability is verified for the 2D and 3D problems of the C5G7-TD reactor transient benchmark and compared with nTRACER. In the 3D problems, the axial insertion

and withdrawal of the control rods are well simulated, and the trends of the core dynamic reactivity and relative fission rate show good agreement with the results of nTRACER within the stochastic errors.

The Monte Carlo calculation usually provides the accuracy and reliability of the calculation result through the sample mean and the variance of the sample mean. In the course of verifying the capability of McCARD transient analysis modules, it is found that the sample variance of a TDMC tally mean obtained from the conventional stochastic processing is highly biased. This is because correlation is made between neutrons during the branching process or population control of the TDMC calculation. The biased variance gives distorted information for judging the accuracy and reliability of Monte Carlo calculation results. Moreover, there is a problem of how to allocate and statistically process the contribution of the delayed neutrons when estimating the variance of tally mean. To address these issues and to estimate accurate variance, a history-based batch method for the TDMC simulation is developed. In the history-based batch method, the neutrons and precursors are grouped in several batches to simulate separately, and the results are statistically processed batch-wisely to break the correlation between the estimates. At the same time, the allocation problem of the delayed neutron contributions can be solved naturally by assigning the contribution to the included batch tally. The developed method is verified in infinite homogeneous two-group problems and C5G7-TD benchmark problems. It gives unbiased variances for the tally means if the batch size is sufficient. In addition, error propagation is observed in the TDMC simulation. It is demonstrated that it stems from the weight normalization scheme in the population control and propagates through the weight of survival neutrons. On the other hand, in the system in which the delayed neutrons are more dominant than the survival neutrons, the error does not propagate significantly because the neutrons are not survived for a long time interval and the delayed neutrons contribution is relatively large.

When establishing point kinetics model for reactor transient analysis or performing a reactivity measurement experiment, it is necessary to calculate kinetics parameters of the core. In general, since it is difficult to obtain an accurate neutron flux distribution in a transient state, kinetics parameters are calculated by assuming solutions of the steady-state transport equation and its adjoint equation as the shape

function and weighting function. However, as it becomes possible to simulate the accurate time-dependent neutron flux distribution through the TDMC method, a time-dependent kinetics parameters estimation method is developed based on the exact point kinetics equations utilizing TDMC simulation. In particular, Monte Carlo algorithms that can efficiently calculate the adjoint response during TDMC forward simulation are developed instead of the conventional Contribution method, which is computationally quite burdensome. To verify the developed methods, the time-dependent kinetics parameters are evaluated in infinite homogeneous two-group problems, and the results show good agreement with the analytic solutions. In addition, it shows more than 1,000 times the computational efficiency for problems near the critical when comparing with the Contribution method. Then to check the applicability of the estimated time-dependent kinetics parameters, the point kinetics equation is established using them and the transient behavior of the system is predicted. The point kinetics analyses are performed on the C5G7-TD problem in which the initial state is critical and the beam trip simulation of the thorium-loaded ADS system at KUCA in which the initial state is subcritical. The PKEs with different kinetics parameters estimated from the  $k$ -eigenvalue calculation, fixed source calculation, and TDMC calculation are compared to each other. It is noted that the developed method can calculate the kinetics parameters reflecting the accurate neutron flux distribution regardless of the system and it provides a framework for the point kinetics analysis in the generalized time domain including the conventional steady-state and arbitrary transient states.

Finally, McCARD/CUPID coupled transient analysis system is established using TCP/IP socket communication to provide transient analysis capabilities for more practical problems considering the thermal-hydraulic feedback. CUPID is a three-dimensional sub-channel code developed by KEARI, and by coupling it with McCARD, it is possible to conduct transient analysis considering the effect of coolant mixing in the sub-channels. The coupled analysis system is verified in the VERA #6 HFP assembly problem by comparing it with the existing McCARD/MATRA coupled steady-state analysis system. The steady-state results match well with the McCARD/MATRA system with a maximum difference of 0.17% in power distribution, 0.06% in coolant exit temperature, and 1.55% in fuel temperature. As for the coupled transient analysis, a simple rod ejection accident is

analyzed in the modified VERA #6 problem under the HZP condition. From the temperature and power trend, the Doppler effect of the fuel temperature feedback is observed, and thus the integrity of the coupled transient analysis system is verified.

**Keyword :**

**Time-dependent Monte Carlo neutron transport method**

**PNS alpha measurement**

**Reactor transient analysis**

**Real variance estimation**

**Time-dependent kinetics parameter estimation**

**T/H coupled transient analysis**

**Student Number : 2014-21424**



# Contents

Chapter 1. Introduction.....	1
1.1. Background.....	1
1.2. Purpose and Scope .....	3
Chapter 2. Time-dependent Monte Carlo Neutron Transport Method .....	6
2.1. TDMC Algorithm with Population Control .....	6
2.2. Alpha Estimation Using TDMC Simulation .....	9
2.2.1. Alpha Estimation by Exponential Fitting .....	1 0
2.2.2. Determination of an Optimum Detector Position .....	1 2
2.3. Application Results .....	1 3
2.3.1. KUCA Pb-Bi-Zoned Experimental Benchmark .....	1 3
2.3.2. AGN-201K Numerical PNS Experiments .....	1 9
Chapter 3. Monte Carlo Transient Analysis .....	2 4
3.1. Delayed Neutron Treatment.....	2 4
3.2. Initial Steady State Modeling.....	3 1
3.3. Moving Geometry Treatment.....	3 3
3.4. Numerical Results.....	3 5
Chapter 4. Real Variance Estimation in TDMC Simulation.....	4 8
4.1. Bias of the Sample Variance in TDMC Simulation .....	4 8
4.2. History-based Batch Method in TDMC Simulation .....	5 1
4.3. Numerical Results.....	5 4
4.3.1. Infinite Homogeneous Two-group Problems.....	5 4
4.3.2. C5G7-TD Benchmark Problems.....	6 1
4.4. Error Propagation in TDMC Method.....	7 0

Chapter 5. Time-dependent Kinetics Parameter Estimation in TDMC Simulation.....	7	6
5.1. Kinetics Parameter Estimation.....	7	6
5.1.1. Exact Point Kinetics Equations.....	7	6
5.1.2. Physical Meaning of Adjoint Response.....	7	8
5.1.3. MC Algorithm for Kinetics Parameter Estimation .....	8	1
5.2. Verification Results .....	8	8
5.2.1. Infinite Homogeneous Two-group Steady-state Problems .....	8	8
5.2.2. Infinite Homogeneous Two-group Transient Problems .....	9	2
5.3. Point Kinetics Analysis .....	9	6
5.3.1. C5G7-TD Benchmark Problem .....	9	6
5.3.2. Numerical Beam Trip Experiment in KUCA .....	1	0 0
 Chapter 6. Neutronics and Thermal-hydraulic Coupled Transient Analysis System .....	1	0 6
6.1. McCARD/CUPID Coupled Analysis System.....	1	0 6
6.2. Verification Results .....	1	1 0
6.2.1. VERA Benchmark Steady-state Problem .....	1	1 0
6.2.2. VERA Benchmark Transient Problem .....	1	1 7
 Chapter 7. Conclusion .....	1	2 1
 Bibliography .....	1	2 4
 Abstract in Korean.....	1	2 7

# **List of Tables**

Table 2.1 Core specifications of AGN-201K.....	2	0
Table 3.1 <sup>235</sup> U delayed neutron parameters [28].....	2	7
Table 3.2 Dimensions of C5G7-TD benchmark .....	3	7
Table 4.1 Two-group cross section data.....	5	4
Table 4.2 Results of the normality test in C5G7-TD0-5 problem.....	6	9
Table 5.1 Two-group cross section data with delayed neutron .....	8	9
Table 5.2 Comparison results of the estimated kinetics parameters in steady-state .....	9	1
Table 5.3 Comparison of FOM in kinetics parameter estimation in steady-state .....	9	2
Table 6.1 Coupling variables of McCARD/CUPID coupled analysis system .....	1	0 8
Table 6.2 Operation condition of VERA #6 HFP assembly problem .....	1	1 2

## List of Figures

Figure 2.1 Schematics of the multiplicative reaction treatment in TDMC .....	7
Figure 2.2 Schematic of the combing method .....	8
Figure 2.3 Fall sideways view of Pb-Bi loaded fuel assembly .....	1 4
Figure 2.4 Fall sideways view of enriched uranium fuel assembly .....	1 4
Figure 2.5 Core configuration of the Pb-Bi-zoned benchmark case 6.....	1 5
Figure 2.6 Angular distribution and energy spectra of the spallation neutron .....	1 6
Figure 2.7 Comparison results of the alpha trends .....	1 8
Figure 2.8 Convergence time and relative detector signal maps .....	1 9
Figure 2.9 Cross-sectional and vertical view of AGN-201K.....	2 0
Figure 2.10 Initial rod positions (left) and initial source positions (right) of the numerical PNS experiments at AGN-201K.....	2 1
Figure 2.11 Convergence time and relative detector signal (source at the center) .....	2 2
Figure 2.12 Convergence time and relative detector signal (source at 30cm) .....	2 3
Figure 2.13 Convergence time and relative detector signal (source at 60cm) .....	2 3
Figure 3.1 Delayed neutron generation according to the sampling methods .....	2 7
Figure 3.2 RSD of the delayed neutron generation according to the sampling methods using the fixed time interval.....	2 8
Figure 3.3 FOM of the delayed neutron generation according to the sampling methods using the fixed time interval .....	2 8
Figure 3.4 Delayed neutron generation according to the sampling methods .....	2 9
Figure 3.5 RSD of the delayed neutron generation according to the sampling methods using the fixed number of precursors .....	2 9
Figure 3.6 FOM of the delayed neutron generation according to the sampling methods using the fixed number of precursors .....	3 0
Figure 3.7 Flow chart of the McCARD transient analysis module.....	3 5
Figure 3.8 Radial core configuration of C5G7-TD benchmark.....	3 6
Figure 3.9 Axial core configuration of C5G7-TD benchmark.....	3 7

Figure 3.10 Transient scenario of TD0 problems .....	3 8
Figure 3.11 Core dynamic reactivity of TD0 problems .....	3 9
Figure 3.12 Fractional core fission rate of TD0 problems .....	4 0
Figure 3.13 Assembly-wise fractional fission rate of TD0-3.....	4 0
Figure 3.14 Assembly-wise fractional fission rate of TD0-5.....	4 1
Figure 3.15 Transient scenario of TD4-1 .....	4 2
Figure 3.16 Transient scenario of TD4-3.....	4 2
Figure 3.17 Transient scenario of TD4-4.....	4 3
Figure 3.18 Core dynamic reactivity of TD4 problems .....	4 4
Figure 3.19 Fractional core fission rate of TD4 problems .....	4 4
Figure 3.20 Trend of assembly-wise fractional fission rate at the top layer (TD4-1).....	4 5
Figure 3.21 Distribution of assembly-wise fractional fission rate .....	4 5
Figure 3.22 Trend of assembly-wise fractional fission rate at the top layer (TD4-3).....	4 6
Figure 3.23 Distribution of assembly-wise fractional fission rate .....	4 6
Figure 3.24 Trend of assembly-wise fractional fission rate at the top layer (TD4-4).....	4 7
Figure 3.25 Distribution of assembly-wise fractional fission rate .....	4 7
Figure 4.1 Schematic diagram of the history-based batch method in TDMC .....	5 3
Figure 4.2 Comparison of $\bar{Q}_{HB}$ trends according to the batch size (subcritical) .....	5 5
Figure 4.3 Comparison of $\bar{Q}_{HB}$ at 50 ms according to the batch size (subcritical).....	5 6
Figure 4.4 Comparison of RSD trends according to the batch size (subcritical) .....	5 7
Figure 4.5 Comparison of the SDs according to the history-based batch method (subcritical) .....	5 7
Figure 4.6 Comparison of the real to apparent SD ratio according to the history-based batch method (subcritical).....	5 8
Figure 4.7 Comparison of $\bar{Q}_{HB}$ trends according to the batch size (supercritical) .....	5 9
Figure 4.8 Comparison of $\bar{Q}_{HB}$ at 9 ms according to the batch size (supercritical).....	5 9

Figure 4.9 Comparison of RSD trends according to the batch size (supercritical).....	6 0
Figure 4.10 Comparison of the SDs according to the history-based batch method (supercritical).....	6 0
Figure 4.11 Comparison of the real to apparent SD ratio according to the history-based batch method (supercritical) .....	6 1
Figure 4.12 Comparison of $\bar{Q}_{HB}$ trends according to the batch size with delayed neutrons (TD0-5).....	6 2
Figure 4.13 Comparison of $\bar{Q}_{HB}$ at 3 ms according to the batch size with delayed neutrons (TD0-5).....	6 2
Figure 4.14 Comparison of RSD trends according to the batch size with delayed neutron (TD0-5).....	6 3
Figure 4.15 Comparison of the SDs according to the history-based batch method with delayed neutron (TD0-5) .....	6 4
Figure 4.16 Trend of the number of independent branches (TD0-5).....	6 5
Figure 4.17 Comparison of the real to apparent SD ratio according to the history-based batch method with delayed neutron (TD0-5).....	6 5
Figure 4.18 Comparison of the estimated variance in TD0-4 problem.....	6 6
Figure 4.19 Comparison of the estimated variance in TD4-4 problem.....	6 6
Figure 4.20 Trend of RSDs in 0D 2G supercritical system without delayed neutrons ....	7 2
Figure 4.21 Trend of RSDs in TD0-5 subcritical problem .....	7 4
Figure 4.22 Trend of RSDs in modified TD0-4 supercritical problem.....	7 4
Figure 4.23 Reaction rate contributions in TD0-5 subcritical problem .....	7 5
Figure 4.24 Reaction rate contributions in modified TD0-4 supercritical problem.....	7 5
Figure 5.1 Tally algorithm for the estimation of kinetics parameters in fixed source mode calculation .....	8 3
Figure 5.2 Modified tally algorithm for the estimation of kinetics parameters .....	8 5
Figure 5.3 Comparison results of the estimated kinetics parameters in steady-state ( $k_{inf} = 0.6$ ) .....	9 0
Figure 5.4 Comparison results of the estimated kinetics parameters in steady-state ( $k_{inf} = 1.0$ ) .....	9 0

Figure 5.5 Comparison results of the estimated kinetics parameters in steady-state ( $k_{inf} = 1.002$ ).....	9	1
Figure 5.6 Transient scenario of material mixing in 0D 2G problem .....	9	3
Figure 5.7 Comparison results of $\Lambda$ regarding $L$ ( $\Delta t = 1 \times 10^{-4}$ sec).....	9	4
Figure 5.8 Comparison results of $\beta_{eff}$ regarding $L$ ( $\Delta t = 1 \times 10^{-4}$ sec) .....	9	4
Figure 5.9 Comparison results of $\Lambda$ regarding $\Delta t$ ( $L = 1 \times 10^{-3}$ sec).....	9	5
Figure 5.10 Comparison results of $\beta_{eff}$ regarding $\Delta t$ ( $L = 1 \times 10^{-3}$ sec) .....	9	5
Figure 5.11 Transient scenario of TD2 problems .....	9	6
Figure 5.12 Estimated $\Lambda$ from the TDMC simulation for TD2-1 .....	9	7
Figure 5.13 Estimated $\beta_{eff}$ from the TDMC simulation for TD2-1 .....	9	7
Figure 5.14 Comparison of PKEs with different kinetics parameters for TD2-1 .....	9	9
Figure 5.15 Comparison of PKEs with different kinetics parameters for TD2-1 (enlarged) 9	9	
Figure 5.16 Fall sideways view of Th-HEU-Gr-PE fuel assembly.....	1	0 1
Figure 5.17 Configuration of the Th-HEU-Gr-PE core .....	1	0 1
Figure 5.18 Estimated $\Lambda$ for the beam trip experiment in Th-HEU-Gr-PE core .....	1	0 2
Figure 5.19 Estimated $\beta_{eff}$ for the beam trip experiment in Th-HEU-Gr-PE core ....	1	0 3
Figure 5.20 Comparison of PKEs with different kinetics parameters for the beam trip experiment in Th-HEU-Gr-PE core.....	1	0 4
Figure 6.1 McCARD/CUPID coupled analysis system.....	1	0 7
Figure 6.2 Radial lattice and data mapping .....	1	0 9
Figure 6.3 Axial lattice and data mapping .....	1	1 0
Figure 6.4 Radial cross-sectional view of the VERA #6 assembly .....	1	1 1
Figure 6.5 Axial cross-sectional view of the VERA #6 assembly .....	1	1 1
Figure 6.6 Trend of the fuel temperature convergence in VERA #6 problem .....	1	1 3
Figure 6.7 Trend of the coolant temperature convergence in VERA #6 problem.....	1	1 4

Figure 6.8 Comparison of the axial power distribution in VERA #6 problem .....	1	1	5
Figure 6.9 Comparison of radial power distribution in VERA #6 problem.....	1	1	5
Figure 6.10 Comparison of the coolant exit temperature in VERA #6 problem.....	1	1	6
Figure 6.11 Comparison of the fuel temperature in VERA #6 problem .....	1	1	6
Figure 6.12 Location of the postulated control rods ejection (red colored).....	1	1	7
Figure 6.13 Trend of the power after the rod ejection .....	1	1	9
Figure 6.14 Trends of the fuel and coolant temperature after the rod ejection .....	1	1	9
Figure 6.15 Power distribution at 0.23 second .....	1	2	0
Figure 6.16 Fuel temperature profile at 0.23 second .....	1	2	0





# Chapter 1. Introduction

## 1.1. Background

Monte Carlo (MC) method has been a reference solver for a long time in the nuclear reactor physics field in that it has no approximation in dealing with complex geometry and directly utilizing a continuous-energy nuclear cross section libraries. In the 2010s, with the development of various methodologies such as Doppler broadened cross section generation, pin-wise tally capability, depletion module, efficient parallel computation and multi-physics coupled analysis system, the whole-core steady-state neutron transport methods for a commercial reactor have almost reached its final stage. In addition to this, as computation power continues to enhance, MC transient neutron transport method for a high-fidelity reactor transient analysis has emerged as a hot topic and researches are actively being conducted. Since MC method can provide reference solutions for various transient analyses including accident analysis of commercial reactor, gen-IV reactor and research reactor, reactor startup analysis, and kinetics experiments analysis, it is imperative to develop MC transient neutron transport methods.

There are two approaches in MC transient neutron transport methods, a quasi-static method [1-3] and a time-dependent Monte Carlo (TDMC) method. The quasi-static method solves the time-dependent neutron flux as the factorization of a shape function and an amplitude function. The shape function is obtained by the MC neutron transport simulation while the amplitude function is calculated by the point kinetics equations (PKE). This method is efficient in that the temporal variation of neutron population or amplitude is treated simply by solving the PKE, but it implies

potential inaccuracies due to the discretization of the time domain. The TDMC method directly tracks neutrons by time bin-by-bin simulation with population control at the end of each time bin to sustain the number of neutrons. Though it divides time into the bins for the population control, the particle simulation is conducted in the continuous time domain without any approximation. However, TDMC method requires high computational cost, and there have been several methodological hurdles for its application, which are the population control, delayed neutron treatment and steady-state initial condition modeling.

Recently, these issues are resolved with the development of noble methods and it becomes viable to simulate neutrons within more practical time ranges. The population control of the particles is essential for TDMC simulation because the number of particles keeps changing to cause a memory shortage in supercritical cases or termination due to the lack of particles in subcritical cases. Kaplan [4] first proposed the TDMC simulation with population control at the time boundaries adjusting weight window and collision biasing. Booth [5] developed the combing algorithm to maintain neutron population by uniformly increasing or decreasing the survival neutrons at the end of time interval. As for the delayed neutron treatment, the issue was the high statistical uncertainty in the direct delayed neutron simulation due to significantly different lifetime of the prompt neutrons and precursors. This was resolved with the idea of Legrady [6] and Sjnitzer [7] to simulate the delayed neutrons via the precursor simulation with the forced decay algorithm. The last is the steady-state initial condition modeling which is represented by the modeling of the neutron and precursor (or delayed neutron) source distribution prior to performing a transient calculation. Sjnitzer [7] demonstrated the steady-state initial condition modeling using conventional MC power iteration scheme in the  $k$ -eigenvalue

calculation. Shaukat [8] proposed a TDMC steady-state simulation method for an initial condition modeling by consistently using TDMC algorithms.

The TDMC methods have been utilized mainly in the field of experiments in research reactors to estimate kinetics parameters such as the prompt neutron decay constant by conducting numerical noise experiments or pulsed neutron source (PNS) experiments [4, 9, 10]. Thanks to the development of methodologies mentioned above and improved computer performances, many reactor physics groups are focusing on the development of a TDMC code for the high-fidelity reactor transient analysis. From the previous study of Shaukat [11], McCARD [12], a Monte Carlo neutron-photon transport code developed in Seoul National University, has equipped with the capability of the TDMC simulation. However, the existing code is limited to the two-dimensional transient analysis which is represented by the change in cross sections and lacks of the parallel computation algorithm. Shaukat also introduces a scale factor as a weight normalization factor multiplied to tally values which may complicate the error quantification. As for the variance estimation, the conventional statistical process conducted for the tally values per neutron as in the fixed source mode calculation may result in the biased variance due to the highly correlated neutrons. Thus, it is highly required to develop advanced TDMC algorithms to perform an accurate and reliable analysis for the realistic reactor transient problems.

## **1.2. Purpose and Scope**

The purpose of this research is to develop advanced time-dependent Monte Carlo algorithms for reactor transient analysis and to extend the applicability of the time-dependent McCARD simulation to realistic problems. The developed advanced

TDMC algorithms include improved TDMC simulation scheme with variance reduction and parallel computation, handling of three-dimensional geometry changes, unbiased variance estimation, efficient adjoint weighted kinetics parameter calculation and thermal-hydraulic coupled transient analysis system.

In chapter 2, the conventional TDMC algorithm using an analog MC branching method with the combing method [5] for population control is described. The scale factor is removed for the simplification and a dynamic weight window is introduced to maintain the efficiency of the particle simulation at each time step. The TMDC simulation using the population control is applied to estimate alpha from the PNS experiment. To resolve the dependency issues regarding the detection position and time of the PNS alpha measurement, an optimum detector position search algorithm is developed based on the TDMC simulation, and applied to the Pb-Bi-zoned experimental benchmark [13] at Kyoto University Critical Assembly (KUCA) and numerical experiments at AGN-201K [14].

In chapter 3, the TDMC methods for the MC transient analysis are presented. For the delayed neutron treatment, the forced decay algorithm with precursor simulation is introduced and the TDMC steady-state simulation method is used for the initial condition modeling. The new feature of moving geometry treatment based on surface representation is implemented to treat realistic three-dimensional transient scenarios. The capability of MC transient analysis is verified for the C5G7-TD benchmark [15] 2-D and 3-D problems by comparing with the deterministic transport code, nTRACER [16].

In chapter 4, the real variance estimation method for TDMC simulation based on the history-based batch method [17] is developed. The source of variance bias in TDMC simulation is explored and the effectiveness of the proposed method is

verified in infinite homogeneous two-group problems and C5G7-TD benchmark problems. In addition, the propagation of the errors in TDMC simulation through the time bin-by-bin weight normalization scheme in the population control is observed and examined in terms of the error propagation formula.

In chapter 5, the time-dependent kinetics parameters are estimated based on the exact point kinetics equations. In the exact point kinetics equations, the kinetics parameters are defined as the ratio between the integrals of the time-dependent shape functions and operators weighted by the adjoint function. By introducing an arbitrary detector response from the adjoint equation of the out-coming collision density equation as a weight function, the time-dependent kinetics parameters can be obtained through the TDMC simulation. The adjoint calculation in TDMC simulation is equivalent with the Contribution method [18] which is quite burdensome for the practical application, so a more efficient MC algorithm is developed with an assumption to fix the time and get the average scheme within a time step. The developed method is verified in infinite homogeneous two-group problems, and applied to a C5G7-TD problem and numerical beam trip simulation at KUCA with the point kinetics analysis using the estimated kinetics parameters.

In chapter 6, a neutronics and thermal-hydraulic coupled transient analysis system, McCARD/CUPID, is established by combining McCARD with a 3D sub-channel code CUPID [19]. McCARD/CUPID is coupled externally using TCP/IP socket communication and a server program. The coupling scheme is verified in comparison with McCARD/MATRA [20] coupled system for the steady-state VERA benchmark [21] HFP assembly problem, and its capability for transient analysis is preliminarily tested for the postulated transient scenario in the same VERA assembly problem.

## Chapter 2. Time-dependent Monte Carlo Neutron Transport Method

### 2.1. TDMC Algorithm with Population Control

To sustain the number of neutrons tracked in an off-critical system, population control is required during the simulation to prevent the everlasting increase or decrease in the neutron population. TDMC neutron transport method employs the time bin-by-bin simulation with the population control at the end of each time step. Within a time step, the neutron time is updated with the sampled track length until it crosses the upper time boundary as

$$t_k^{i,j} = t_{k-1}^{i,j} + \frac{l_k^{i,j}}{\sqrt{2E_k^{i,j} / m_n}} , \quad (2.1)$$

where  $i, j$ , and  $k$  are the time step, history, and track index.  $t_k^{i,j}$ ,  $l_k^{i,j}$ , and  $E_k^{i,j}$  are the time, sampled track length, and energy after the  $k$ -th flight of history  $j$  at time step  $i$ .  $m_n$  is the neutron mass. When the sampled neutron time exceeds the upper time boundary,  $T_{i+1}$ , the neutron is stopped and stored with its information at  $T_{i+1}$  as

$$l_k^{i,j} = (T_{i+1} - t_{k-1}^{i,j}) \sqrt{2E_k^{i,j} / m_n} \quad (t_k^{i,j} > T_{i+1}) . \quad (2.2)$$

There are two approaches in dealing with the multiplicative reactions in TDMC simulation. One is the analog method to let the multiplicative reactions make new branches. The other is the branchless method [7] which adjusts the neutron weight

instead of making new branches in accordance with the expected number of neutrons at each collision and uses a dynamic weight window to keep the neutron weight during the simulation. In both methods, population control is needed at the end of each time step since the number of neutrons is not kept constant and their weights differ from each other. After all neutrons in the  $i$ -th time step are simulated, the survival neutrons are discarded or split to maintain the number of neutrons while preserving the total weights.

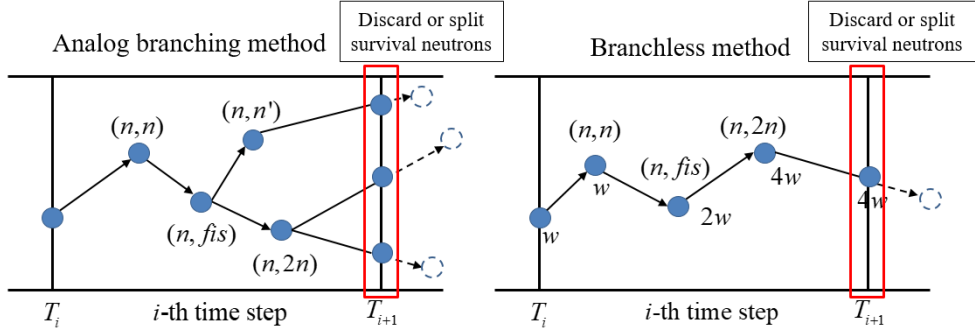


Figure 2.1 Schematics of the multiplicative reaction treatment in TDMC

The well-known population control algorithms are the Russian roulette/splitting and combing method. The number of neutrons and their weights after population control is set as below to preserve the total weights of neutrons.

$$\bar{w}_{i+1} = \frac{\sum_{j=1}^{n_{s,i}} w_{ij}}{N} \quad (2.3)$$

In the above equation,  $n_{s,i}$  and  $N$  indicate the number of survival neutron at the end of  $i$ -th time step and the inputted number of neutrons to preserve. When a neutron



weight is larger than the average weight, the neutron is split into  $\left\lfloor \frac{w_{ij}}{\bar{w}_{i+1}} \right\rfloor + 1$  neutrons with the probability of  $\frac{w_{ij}}{\bar{w}_{i+1}} - \left\lfloor \frac{w_{ij}}{\bar{w}_{i+1}} \right\rfloor$ , else it is split into  $\left\lfloor \frac{w_{ij}}{\bar{w}_{i+1}} \right\rfloor$  neutrons. When a neutron weight is smaller than the average weight, the neutron is survived with the probability of  $\frac{w_{ij}}{\bar{w}_{i+1}}$  or it dies. The difference between the Russian roulette/splitting and combining method is the usage of a random number. In Russian roulette/splitting method, a random number is sampled for every particle and thus the number of neutrons to be sampled is not always to be exactly  $N$ . On the other hand, only one random number is sampled in the combining method and it always samples the exact targeted number of  $N$  neutrons. The probability of how many neutrons to be sampled at each neutron is same in both methods and both are known to be unbiased method. The below figure shows the schematic of the combining method.

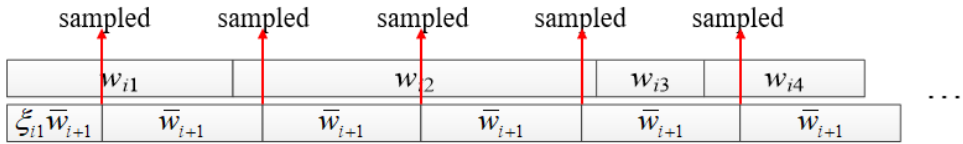


Figure 2.2 Schematic of the combining method

McCARD employs the analog MC branching scheme with the combining method at the end of the time step for TDMC simulation. To ensure the efficient simulation according to the changing average neutron weight after the population control, McCARD adjusts the dynamic weight window used in the implicit capture before it starts the next time step simulation as

$$W_{S,i+1} = \frac{1}{2} \bar{w}_{i+1}, \quad W_{L,i+1} = \frac{1}{4} \bar{w}_{i+1}. \quad (2.4)$$

In the above equations,  $W_{S,i+1}$  and  $W_{L,i+1}$  denote the survival weight and the lower weight boundary of the implicit capture at  $(i+1)$ -th time step.  $\bar{w}_{i+1}$  is the average neutron weight at  $(i+1)$ -th time step after the population control.

## 2.2. Alpha Estimation Using TDMC Simulation

The prompt neutron decay constant,  $\alpha$ , has played a key role in reactor kinetics analyses in that it gives an intuitive understanding of asymptotic behaviors and it can be directly measured from the experiments. One of the well-known alpha measurement methods is the pulsed-neutron-source (PNS) method, which obtains the alpha by the exponential regression of the time-dependent detector signals after injecting a short burst of neutrons. After the higher mode terms decay out, one can fit the time-dependent detector signals to a single exponential function and get the fundamental mode alpha independent of the energy characteristic and positioning of a detector. However, it has been reported [22, 23] that inconsistent alpha values are measured from different detector positions, which is attributed to the remaining space- and time-dependent higher mode effects. In the same context, how to determine a good detector position and time for PNS alpha measurement is still an issue.

There have been several approaches to reduce the higher mode terms from detector signals by the post-processing methods. Taninaka [24] suggested the masking technique to exclude the initial parts of detector signals which contain the

higher mode effects when conducting alpha fitting. In addition to the temporal masking of signals from a detector, Katano [25] devised the estimation method to reduce higher mode effects by the linear combination of signals from multiple detectors. These methods give clever ideas to eliminate higher mode effects from fitting data, but they cannot be used to predict and choose the optimum detector position before the experiment.

Based on the time bin-by-bin simulation with the population control algorithm, the TDMC method can track the temporal behavior of neutrons with sufficiently low stochastic errors even if the system is far from the critical state. Therefore, by utilizing TDMC simulation for the PNS alpha measurement, an optimum detector position search algorithm is developed to resolve the dependency issues.

### 2.2.1. Alpha Estimation by Exponential Fitting

From the TDMC simulation of the PNS experiment, one can obtain the time-dependent detector signals at the desired positions by tallying the responses from prompt neutrons as

$$R_D(\mathbf{r}, \bar{t}_i) = \sum_m \sum_r \int_{V_D} \int_E \int_{4\pi} \int_{\bar{t}_i - \Delta t/2}^{\bar{t}_i + \Delta t/2} \Sigma_r^m(\mathbf{r}, E) \Phi_p(\mathbf{r}, E, \boldsymbol{\Omega}, t) d\mathbf{r} dE d\boldsymbol{\Omega} dt \quad (2.5)$$

where  $m$  and  $r$  present the isotope and the reaction type respectively.  $V_D$  is the volume of a detector and  $\Delta t$  is the time interval of the tally. Subscript  $p$  of the angular flux denotes the prompt neutron. Then the time-dependent tally results can be fitted to the exponential function as [26]

$$R_D(\mathbf{r}, t) = C_1 \cdot \exp[-\tilde{\alpha}_0(\mathbf{r} | t_s) \cdot (t - t_s)] + C_2. \quad (2.6)$$

In the equation,  $C_1$  and  $C_2$  are fitting constants, and  $t_s$  is the starting time of the fitting. Since the remaining higher mode components decay out differently over time, different alpha values are estimated according to the starting time of fitting.  $\tilde{\alpha}_0(\mathbf{r} | t_s)$  indicates the alpha estimate of the detector located at  $\mathbf{r}$  using its detector signals starting from  $t_s$  and is expected to converge to the fundamental alpha as the higher modes disappear.

The convergence of the alpha estimates can be diagnosed by simply comparing the estimates to the reference alpha. The onset time of the convergence is determined when the relative difference between the mean of alpha estimates and the reference alpha becomes less than the prescribed convergence criterion,  $\varepsilon$ , as

$$t_0(\mathbf{r}) = \min \left\{ t_s; \left| \frac{\bar{\alpha}_0(\mathbf{r} | t) - \alpha_{\text{ref}}}{\alpha_{\text{ref}}} \right| < \varepsilon + 2\sigma \right\}. \quad (2.7)$$

$\bar{\alpha}_0(\mathbf{r} | t)$  and  $\sigma$  are the mean of alpha estimates and the standard deviation of the relative difference respectively which are introduced to consider the stochastic error of the MC simulation for convergence diagnosis. The convergence time of the detector located at  $\mathbf{r}$ ,  $t_0(\mathbf{r})$ , is then defined as the minimum starting time of the fitting in which the mean of alpha estimates,  $\bar{\alpha}_0(\mathbf{r} | t)$ , satisfy the convergence criterion including stochastic errors.

The reference fundamental alpha,  $\alpha_{\text{ref}}$ , is calculated using the MC  $\alpha$ -iteration method [27] implemented in McCARD. The MC  $\alpha$ -iteration method is one of the  $\alpha$ -

static MC methods which solve the following  $\alpha$ -mode eigenvalue equation with the MC power method. In the integral form of the collision density equation, the  $\alpha$ -mode eigenvalue equation can be expressed as

$$S_t = \alpha \mathbf{R} S_t, \quad (2.8)$$

$$\mathbf{R} S_t \equiv \frac{1}{v(E) \Sigma_t(\mathbf{r}, E)} \sum_{j=0}^{\infty} \int d\mathbf{r}' \int dE_0 \int d\mathbf{\Omega}_0 \cdot K_{p,j}(\mathbf{r}', E_0, \mathbf{\Omega}_0 \rightarrow \mathbf{r}, E, \mathbf{\Omega}) \int d\mathbf{r}_0 \cdot T(E_0, \mathbf{\Omega}_0; \mathbf{r}_0 \rightarrow \mathbf{r}') S_t(\mathbf{r}_0, E_0, \mathbf{\Omega}_0), \quad (2.9)$$

$$S_t \equiv \frac{\alpha}{v(E)} \Phi_p(\mathbf{r}, E, \mathbf{\Omega}), \quad (2.10)$$

where  $S_t$  is named as the time source. All other notations follow the convention except that the delayed fission neutron is ignored in the transition kernel  $K_p$  and angular flux  $\Phi_p$ . In the same way that the fundamental mode  $k$  is calculated with the iterative fission source updates by the MC power method, the fundamental mode  $\alpha$  can be obtained with the iterative time source updates.

### 2.2.2. Determination of an Optimum Detector Position

In terms of experimental measurement, the optimum detector position in the PNS experiment is where the estimated alpha value has high reliability. Since the detector counting is a Poisson process, the detector count rate has stochastic uncertainty inversely proportional to the average count rate. This means the higher the signal of the detector, the more reliable the results are. Then one can determine

the optimum detector position as to where it shows the highest detector signal after it converges to the fundamental mode alpha. The detector signals after it converges can be calculated from TDMC simulation as

$$\bar{R}_D(\mathbf{r}) = \sum_m \sum_r \int_{V_D} \int_E \int_{4\pi} \int_{t_0(\mathbf{r})}^{t_0(\mathbf{r})+\Delta T} \Sigma_r^m(\mathbf{r}, E) \phi_p(\mathbf{r}, E, \mathbf{\Omega}, t) d\mathbf{r} dE d\mathbf{\Omega} dt, \quad (2.11)$$

where  $t_0(\mathbf{r})$  is the onset time of the convergence at the detector located at  $\mathbf{r}$  and  $\Delta T$  is the fitting time interval.

## 2.3. Application Results

### 2.3.1. KUCA Pb-Bi-Zoned Experimental Benchmark

The developed method is applied to the Pb-Bi-zoned experimental benchmark at KUCA which is a multi-core type critical assembly in Kyoto University Research Reactor Institute operated with zero power condition. The core consists of Pb-Bi loaded 93% enriched uranium fuel and polyethylene moderator and reflector, each of which has coupon-shaped plates stacked inside the aluminum sheath. Each plate has a  $5.08 \times 5.08$  cm dimension and the aluminum sheath has a  $5.53 \times 5.53$  cm dimension with 1 mm thickness. The overall height of the assembly is 152.40 cm with the upper and lower polyethylene reflector layers of more than 50 cm long and the fuel layers of approximately 40 cm long. There are 3 control rods and 3 safety rods composed of  $B_2O_3$  along the side of the core region. The benchmark provides 6 types of subcritical core configurations with a different number of fuel assemblies. The PNS experiments are conducted with the spallation neutron sources generated by injecting 100 MeV protons to the Pb-Bi target at the center of the core. The alpha

is measured with optical fiber detectors at three different detector positions. Among the core configurations, case 6 is selected for the application which has the deepest subcriticality. Figures below show two types of the fuel assemblies of the case 6 core and its core configuration. The core consists of 20 enriched uranium fuel assemblies and 8 Pb-Bi loaded fuel assemblies surrounding the Pb-Bi spallation source target. The fuel region is surrounded by polyethylene moderator and all control rods and safety rods are fully withdrawn. From the core configuration, one can expect the spallation source will make different detector signals depending on the location and time, which results in inconsistent alpha measurements.

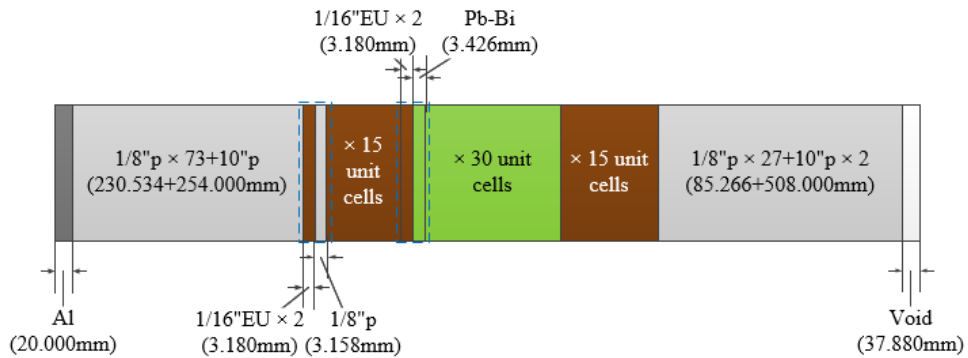


Figure 2.3 Fall sideways view of Pb-Bi loaded fuel assembly

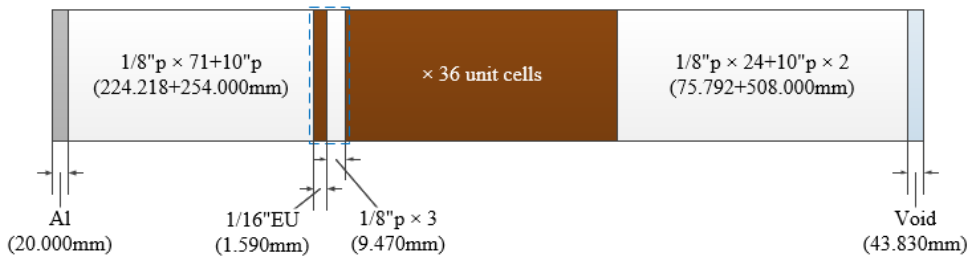


Figure 2.4 Fall sideways view of enriched uranium fuel assembly

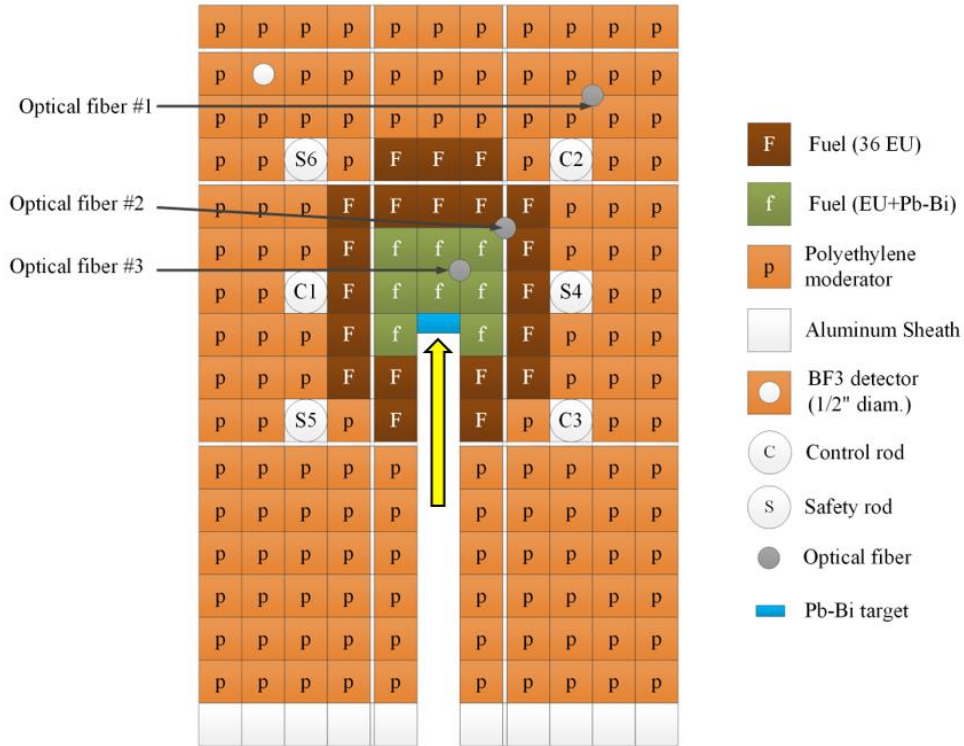


Figure 2.5 Core configuration of the Pb-Bi-zoned benchmark case 6

For the TDMC PNS simulation, the initial spallation neutron source is modeled using MCNPX2.6.0 proton simulation. The spallation neutron spectra and angular distribution are obtained by tallying the neutrons leaving the Pb-Bi target. The neutron spectra at every 15 degrees with respect to the proton beam are normalized respectively and inputted to McCARD TDMC simulation as initial source information. The calculated spallation neutron angular distribution and energy spectra are given in figure below. One can see the overall angular distribution is



biased to the beam direction and the energy spectrum is more hardened as the outgoing angle with respect to the beam direction is small.

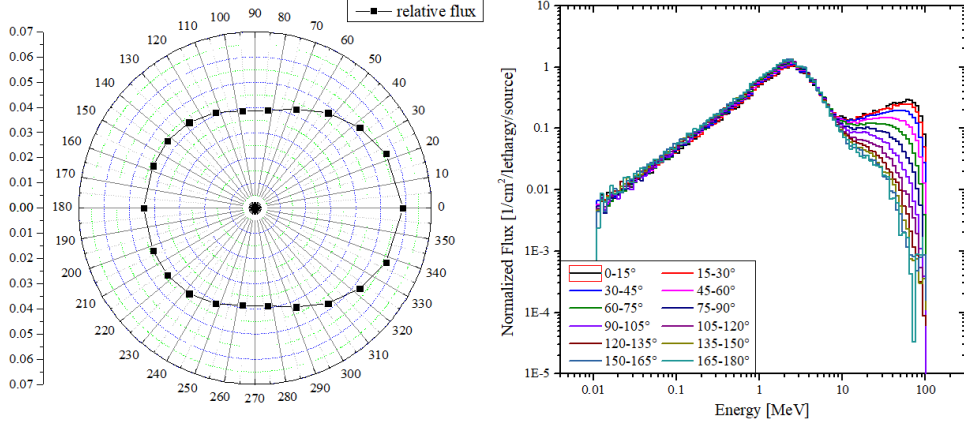


Figure 2.6 Angular distribution and energy spectra of the spallation neutron

McCARD TDMC simulation is done using 100 million histories and 0.1 ms time interval up to 5.0 ms. To estimate stochastic errors, the history-based batch method is used with 100 batches. The time-dependent detector signals for the exponential alpha fitting are tallied as the sum of  $(n, \alpha)$  and  $(n, p)$  reactions, which are the charged particle emission reactions of the optical fiber detector used in the experiment. All available locations between assemblies are selected as candidate detector positions where the convergence of alpha and amplitude of detector signals are evaluated. To avoid the distortion of the neutron tracking, the reaction rate is tallied with the virtual detector material not influencing the real simulation.  $\alpha_{\text{ref}}$  is calculated by the  $\alpha$ -iteration method using 100,000 histories and 100 active cycles.

In both TDMC and  $\alpha$ -iteration calculations, ENDF/B-VII.1 cross section library is used.

To verify the effectiveness of the developed method, the trends of alpha at the detector locations designated in figure 2.5 are compared with the experimental results. Among the three detectors, detector #3 is excluded for the comparison because the detector signals seem to be contaminated with gamma-ray induced by high energy neutrons emitted from the target. Figure 2.7 shows the comparison results of the alpha trend at the two detector positions. The solid lines and the dashed lines are the alpha trends estimated with the TDMC simulation and the experiment. The reference alpha is calculated as 1950.0 with its standard deviation of 2.0. All results show the convergence to the reference alpha as the higher modes decay out, but the convergence trend varies depending on the detector position. There is some discrepancy between the TDMC and experimental results in the initial trend and its convergence time, which is attributed to be due to the difference in the energy sensitivity to the neutron yield of the detector. It is meaningful, however, in that both results show the same difference of 0.4 ms in the convergence times between two detectors. In the TDMC results, detectors #1 and #2 converge to the reference alpha within stochastic error at 1.0 ms and 0.6 ms, while they converge at 1.7 ms and 1.3 ms in the experimental results. This demonstrates that the TDMC simulation can predict the relative convergence time of alpha at different detector positions quite accurately.

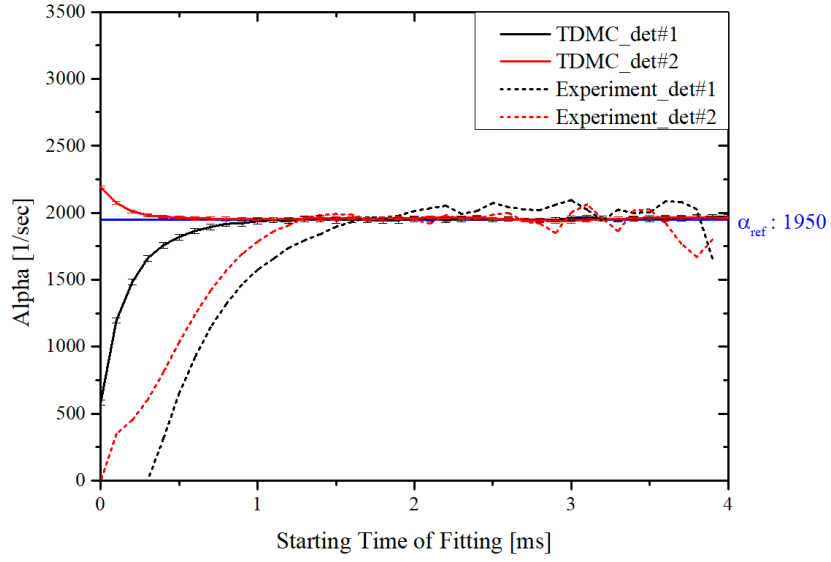


Figure 2.7 Comparison results of the alpha trends  
from TDMC and experimental data

The convergence time and the amplitude of the detector signal are compared to determine the optimum detector position at candidate detector positions. The convergence criterion  $\varepsilon$  of 0.02 is used for the convergence diagnosis. Figure 2.8 is the map of the convergence time and the relative amplitude of detector signals. The results show faster convergence time at the front regions surrounding the spallation neutron source and the polyethylene moderator regions adjacent to fuel regions are determined as the optimum detector positions showing the highest detector signals.

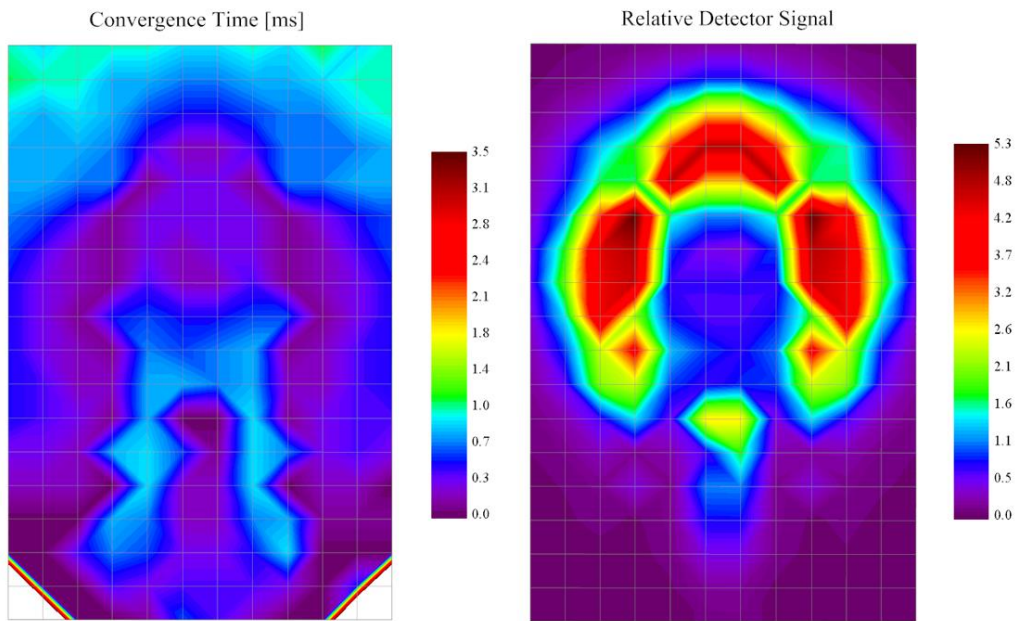


Figure 2.8 Convergence time and relative detector signal maps  
of the case 6 core

### 2.3.2. AGN-201K Numerical PNS Experiments

The proposed method is examined in numerical PNS experiments at AGN-201K, a research and educational reactor at Kyung Hee University. The reactor is operated with 10 Watt power condition where the maximum neutron flux is about  $4.5 \times 10^8 \text{ \#/cm}^2\text{-sec}$ . The core comprises a stack of 9 solid fuel disks surrounded by a graphite reflector and lead shield in a water tank. The fuel disks are made of a homogenous material of 19.5 w/o  $\text{UO}_2$  and polyethylene moderator. As for safety and control devices, there are two safety rods and one coarse and one fine control rod, which are made of the same fuel material and inserted from the bottom of the core. In addition, there are a glory hole and four access ports in which a source or

detectors can be placed respectively. The core configuration of AGN-201K is shown in Figure 2.9 and the core specifications are given in the table below.

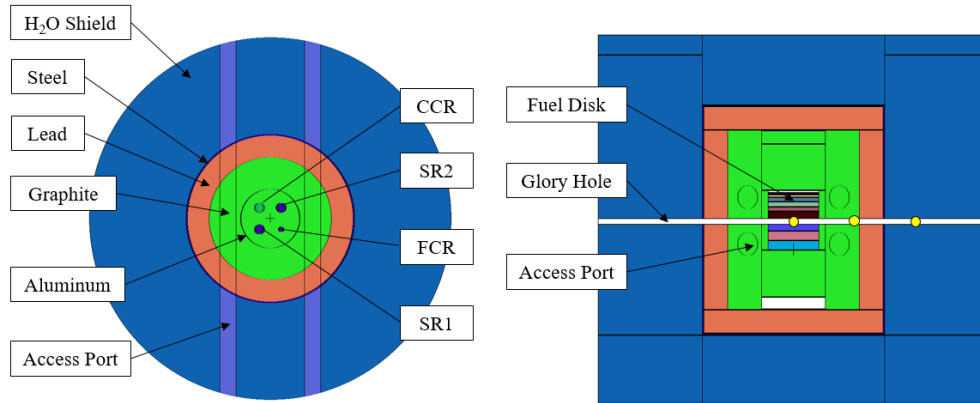


Figure 2.9 Cross-sectional and vertical view of AGN-201K

Table 2.1 Core specifications of AGN-201K

Contents	Value [cm]	Contents	Value [cm]
Fuel disk radius	12.800	Fine CR radius	1.000
Aluminum radius	16.100	Coarse CR and SR radius	2.250
Graphite reflector radius	33.120	Glory hole radius	1.185
Lead shield radius	44.926	Access port radius	5.000
Water reflector radius	98.000	Active core height	24.500

The numerical PNS experiments are conducted with all control rods and safety rods fully ejected from the core to postulate the deepest subcritical state. All rods are ejected and located 7cm below the bottom disk, and the effective multiplication factor of the core is  $0.97906 \pm 0.00009$ . Since the initial source position can be easily adjusted along the glory hole, AGN-201K is suitable for examining the sensitivity of

the optimum detector position to the initial source position. The initial source is assumed to be a Cf-252 source located at a prescribed position, 0cm, 30cm, and 60cm away from the center of the core, and then jerked immediately to make a pulsed neutron source. The initial control rod and safety rod positions and source locations are depicted in Figure 2.10.

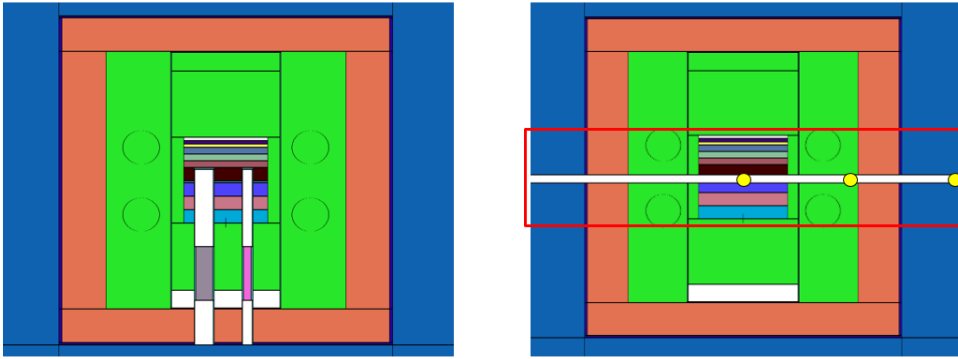


Figure 2.10 Initial rod positions (left) and initial source positions (right) of the numerical PNS experiments at AGN-201K

McCARD TDMC calculation is done with 100 million histories and 100 history-based batches. The simulation time is set to 5.0 ms with a 0.1 ms time interval. The time-dependent alpha is estimated with charged particle emission reaction tally of the optical fiber detector in cylindrical meshes surrounding the active core region. The reference alpha is estimate as  $-333 \pm 10$  from the  $\alpha$ -iteration method, and the convergence criterion is set to 0.02.

Figure 2.11 to 2.13 are the map of the convergence time and relative detector signals according to the initial source position. In the left figures, where the source is located at the center of the core, the boundary region between the core and graphite reflector shows the fastest convergence but the relative detector signal is larger inside

the core, indicating the optimum detector position. When the source is located 30cm away from the center, the far side of the core is determined to be the optimum position among the fast convergence regions. On the other hand, when the source is located at a 60cm position, the near side of the core is shown to be the optimum position. In all results, the convergence trends at each region come from the combination of the neutron sources propagated from the initial source location and the fission sources propagated from the core region. Although this method does not analyze higher modes in the combined equation term by term, it can simply but effectively specify the positions where the higher mode effects disappear faster and determine the optimum position where shows the highest detector signals using TDMC simulation.

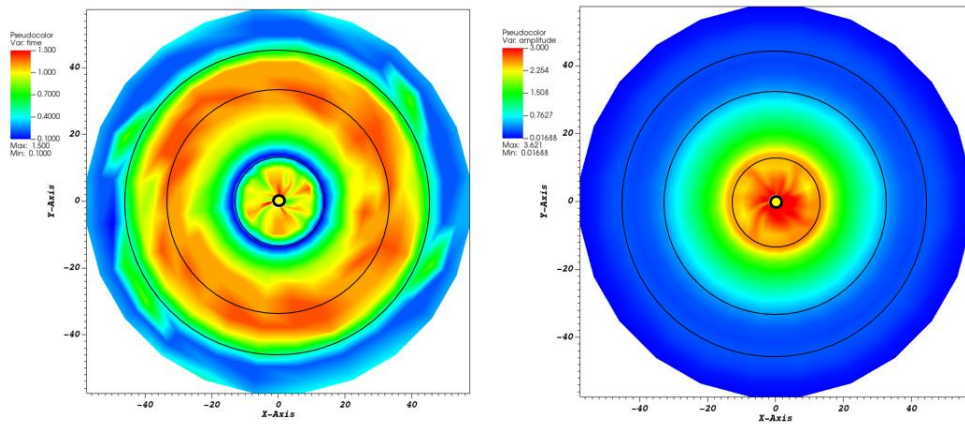


Figure 2.11 Convergence time and relative detector signal (source at the center)

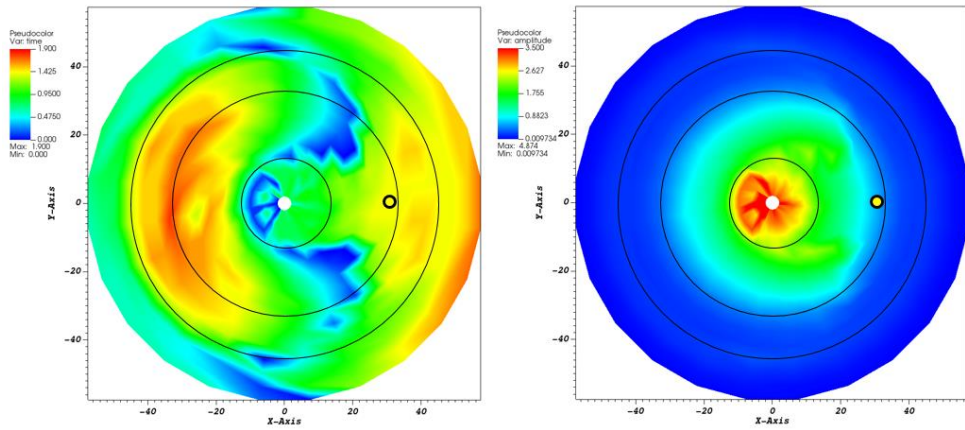


Figure 2.12 Convergence time and relative detector signal (source at 30cm)

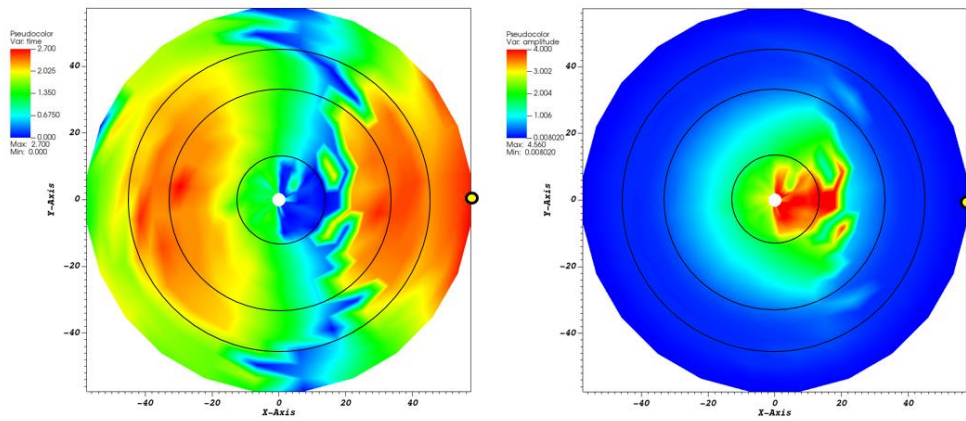


Figure 2.13 Convergence time and relative detector signal (source at 60cm)



## Chapter 3. Monte Carlo Transient Analysis

### 3.1. Delayed Neutron Treatment

In the conventional MC methods, the delayed neutrons are sampled directly from the fission events. When a delayed neutron is sampled, a precursor family is determined first and then time and energy are sampled according to its precursor family. Since the lifetime of the prompt neutrons and precursors are significantly different, the direct simulation of delayed neutrons causes a large statistical fluctuation in the delayed neutron population. In general, the life time of the prompt neutron is about  $10^{-4}$  second order, while the life time of precursors ranges from  $10^{-1}$  to 100 second order.

The drawbacks of the direct delayed neutron simulation are originated from the limited resources and one-time use of a delayed neutron. To overcome the large fluctuation problem, a forced decay algorithm [6, 7] with precursor simulation is proposed by Hoogenboom's group. When a fission event occurs during the simulation, precursors are sampled and stored as many as

$$M_{C,ijk} = \left\lfloor \frac{\nu_{d,ijk}}{k_0} + \xi \right\rfloor, \quad (3.1)$$

where  $\nu_{d,ijk}$  is the average number of delayed neutrons produced from a fission at the  $k$ -th collision of the  $j$ -th neutron in the  $i$ -th time step.  $k_0$  and  $\xi$  are the  $k$ -eigenvalue at the initial steady state and a random number.  $\lfloor x \rfloor$  indicates the largest integer not exceeding  $x$ . The sampled precursors are treated as a combined precursor which presents all the contributions from precursor families to reduce stochastic

fluctuation due to different decay characteristics. Since the precursors are accumulated during the simulation, the precursor population is controlled by the combing method at the end of each time step to maintain the prescribed number of precursors. All the stored precursors are forced to decay and generate delayed neutron in the next time step conserving the expected weight of a delayed neutron. The probability of a precursor created at  $t_0$  decays at time  $t$  is

$$P_d(t) = \sum_l f_l \lambda_l e^{-\lambda_l(t-t_0)}, \quad (3.2)$$

where  $f_l$  and  $\lambda_l$  are the fraction and the decay constant of  $l$ -th precursor family. time step conserving the expected weight of a delayed neutron. One can see that instead of fixing a precursor family all contributions from each family are reflected when the properties of a delayed neutron is sampled. Each precursor is forced to decay within the next time step uniformly and the weight is determined by the importance sampling technique to preserve the expected weight.

$$P_d^*(t) = \frac{1}{T_{i+1} - T_i} = \frac{1}{\Delta T_i}, \quad (T_i < t < T_{i+1}) \quad (3.3)$$

$$w_{d,ij} = \bar{w}_i^C \frac{P_d(t)}{P_d^*(t)} = \bar{w}_i^C \Delta T_i \sum_l f_{l,j} \lambda_{l,j} e^{-\lambda_{l,j}(t-t_{0,j})} \quad (3.4)$$

In the above equations,  $\Delta T_i$  is the  $i$ -th time step interval and  $\bar{w}_i^C$  is the weight of precursors in  $i$ -th time step after population control. After the time and weight of a delayed neutron is sampled, the energy is sampled from the delayed chi-distribution of a precursor family which is determined from the probability as

$$P_i(t) = f_i \lambda_i e^{-\lambda_i(t-t_0)} / \sum_{i'} f_{i'} \lambda_{i'} e^{-\lambda_{i'}(t-t_0)} . \quad (3.5)$$

To examine the effectiveness of the forced decay algorithm compared to the direct sampling method, the generation of the delayed neutron per precursor or fission event within a time interval is compared. An initially steady-state condition is assumed with the decay constants and delayed neutron fractions of the precursor families given in the table below. The comparison is conducted by varying the total number of precursors and the time interval. Figures 3.1 to 3.3 are the comparison results using the fixed time interval of 0.1 ms. In both methods, the stochastic uncertainty becomes smaller as the number of precursors increases but it shows much lower relative standard deviation (RSD) in the forced decay cases. In the direct sampling method, the RSDs slowly increase over time because the delayed neutrons are rarely sampled in a distant time interval. On the other hand, the RSDs decrease over time in the forced decay method because the deviation between neutron weights becomes smaller while the number of neutrons to be sampled is kept constant. In terms of the figure of merits (FOM), the forced decay algorithm shows much higher FOM than the direct sampling method and both FOM results show the same trend regardless of the number of precursors since the time is proportional and the variance is inversely proportional to the number of precursors. Figures 3.4 to 3.6 are the comparison results using 100 million fixed number of precursors. In the direct sampling method, more delayed neutrons are sampled within the time interval as the size of the time interval increases, resulting in a smaller RSD. On the other hand, the deviation of the delayed neutron weight becomes larger as the size of the time interval increases in the forced decay algorithm, resulting in a larger RSD. However, it is shown that the FOM is much larger for all cases in the forced decay algorithm.

Table 3.1  $^{235}\text{U}$  delayed neutron parameters [28]

Family	Decay constant $\lambda_i$ [ $\text{s}^{-1}$ ]	Fraction $\beta_i$
1	0.0124	0.000215
2	0.0305	0.001424
3	0.1110	0.001274
4	0.3010	0.002568
5	1.1400	0.000748
6	3.0100	0.000273
Sum		0.006475

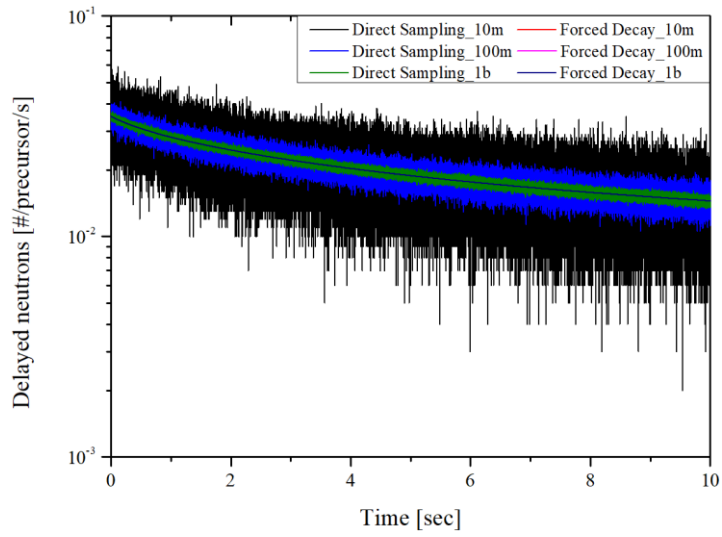


Figure 3.1 Delayed neutron generation according to the sampling methods  
using the fixed time interval

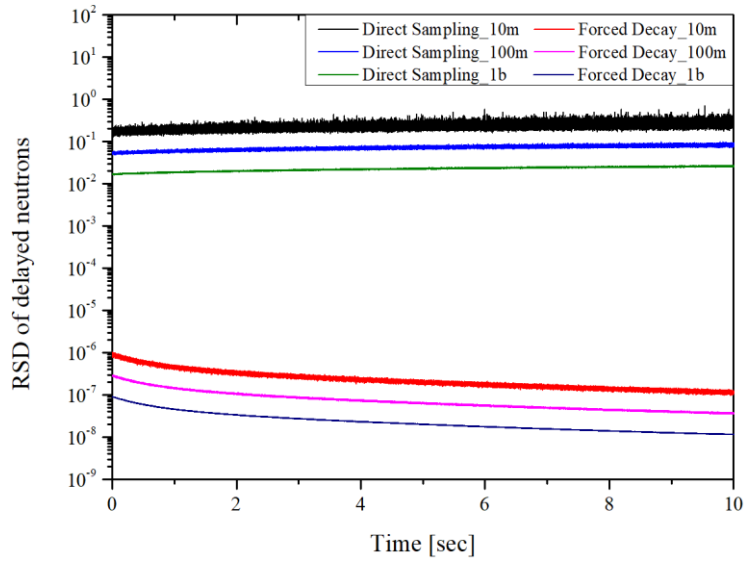


Figure 3.2 RSD of the delayed neutron generation according to the sampling methods using the fixed time interval

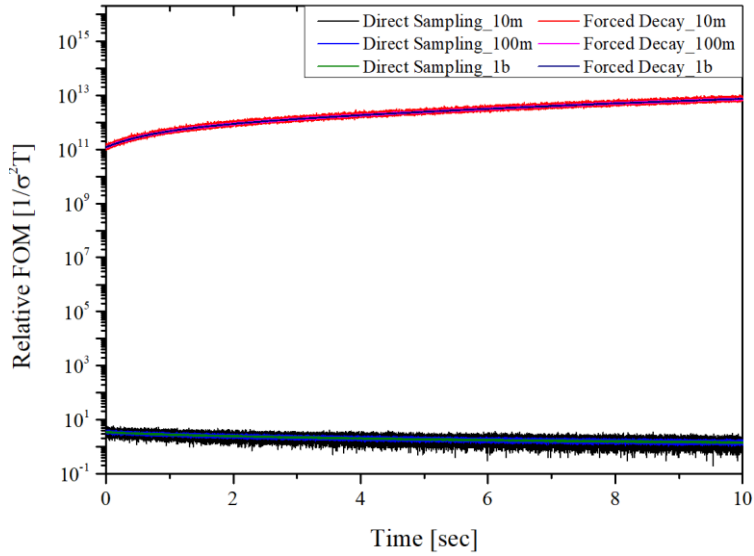


Figure 3.3 FOM of the delayed neutron generation according to the sampling methods using the fixed time interval

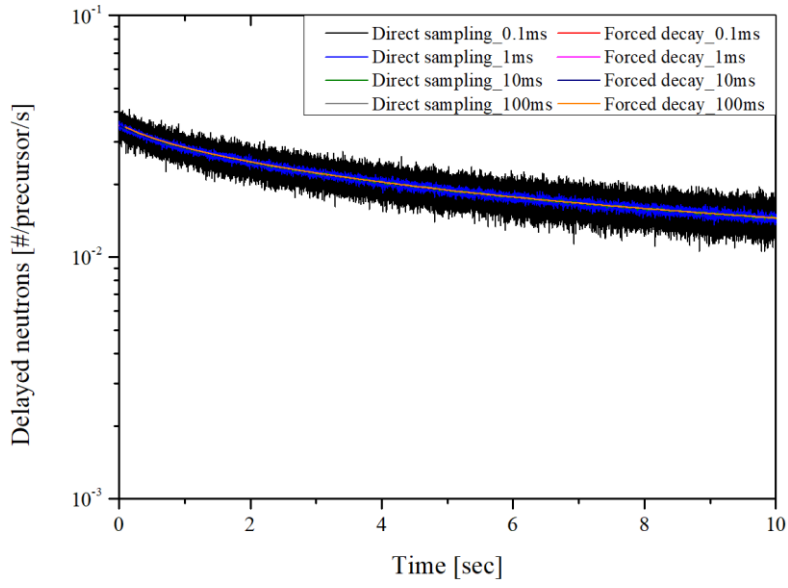


Figure 3.4 Delayed neutron generation according to the sampling methods using the fixed number of precursors

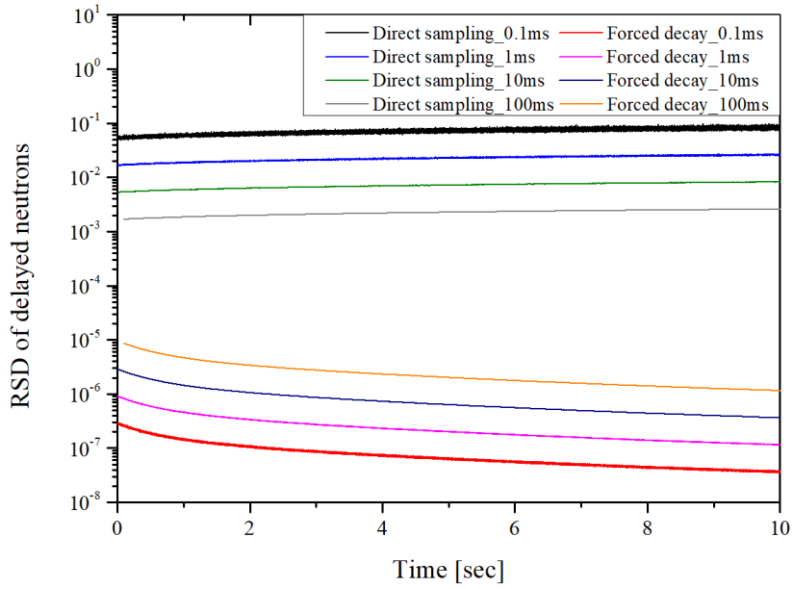


Figure 3.5 RSD of the delayed neutron generation according to the sampling methods using the fixed number of precursors

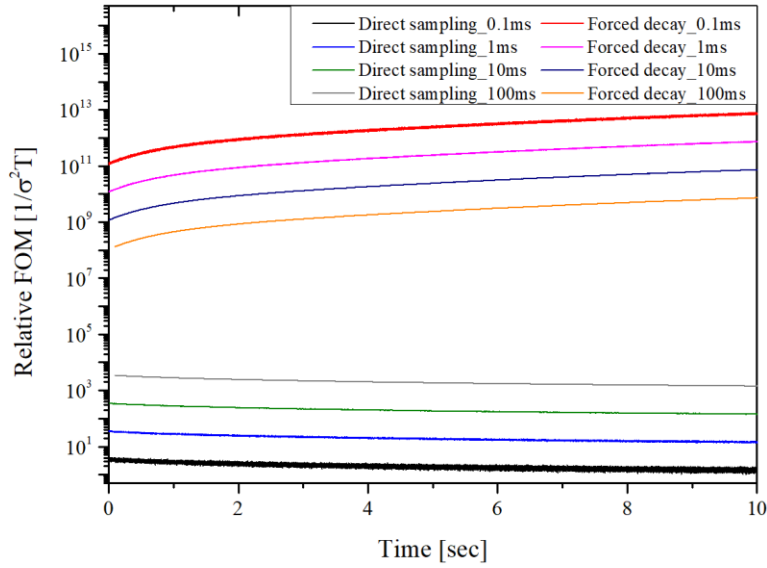


Figure 3.6 FOM of the delayed neutron generation according to the sampling methods using the fixed number of precursors

The forced decay algorithm with the precursor combing is an unbiased method and effectively simulates the relatively important precursors for the next time interval. In combination with the dynamic weight window scheme in McCARD, the effects of delayed neutrons are automatically reflected in the results since the survival weight and lower weight boundary in equation (2.4) are determined by the survival neutron weight at the end of each time step. If the delayed neutron weight is far smaller than the dynamic weight window, most of the delayed neutrons are filtered in the weight window and will not affect the results and vice versa. However, there are some points that users may consider when using the TDMC simulation with forced decay algorithm. They are the number of precursors to simulate and the time interval. Since the relative weight of delayed neutrons to survival neutrons is not known in transient scenarios, the number of precursors is recommended to be the same with the number of neutrons to guarantee a similar level of stochastic error

even in systems where delayed neutrons are highly dominant. As for the time interval, it is recommended to be several times of the generation time. A short time interval leads to inaccurate calculation results with large stochastic uncertainty and requires a large computational burden, while a long time interval leads to the memory shortage in supercritical cases and the lack of survival neutrons in subcritical cases. In terms of the forced decay algorithm, a long time interval may cause relatively large stochastic error from the delayed neutrons due to a large deviation of the delayed neutron weights. Therefore, it is recommended to determine a time interval of TDMC simulations as several times of the generation time.

### 3.2. Initial Steady State Modeling

In most reactor transient analyses, transient start from the steady-state initial condition, which means the initial source distribution of the prompt neutrons and delayed neutron precursors should be obtained. In McCARD, a new MC steady-state simulation method [8] has been developed based on TDMC simulation. Compared to the steady-state modeling method [7] using conventional MC power iteration scheme, it can model the initial source distribution during the consistent TDMC simulation without any calculation mode changes. In the well-known steady-state analysis using  $k$ -eigenvalue calculation, the steady-state properties can be obtained by altering  $\nu_f$  with fictitious one,  $\nu_{fic.}$ , defined by  $\frac{\nu_f}{k}$ . By making the best use of this concept, one can get the steady-state source distribution via TDMC simulation with a slight modification in the number of fission neutron sampled and  $k$  as



$$M_{m,ijk} = \left[ \frac{v_m}{k_{i-1}} + \xi \right], \quad (3.6)$$

$$k_i = \frac{G_{fis}^i}{L_{leak}^i + L_{cap}^i + L_{fis}^i + L_{n\lambda n}^i - G_{n\lambda n}^i}. \quad (3.7)$$

where the subscript  $m$  denotes the prompt neutron or delayed neutron (or precursor).  $k_i$  is the multiplication factor in  $i$ -th time step defined as the ratio of gain terms and loss terms within the time step. After the fission source density are converged to the steady-state distribution, the family distribution and the number density of the sampled precursors should be determined. The precursor family distribution at the steady-state can be easily calculated from the precursor balance equation as

$$\frac{\partial C_l(\mathbf{r}, t)}{\partial t} = \beta_l v \Sigma_f \phi(\mathbf{r}) - \lambda_l C_l(\mathbf{r}, t), \quad (3.8)$$

$$f_{l,0} = \frac{C_{l,0}}{C_0} = \frac{\frac{\beta_l}{\lambda_l} v \Sigma_f \phi(\mathbf{r})}{\sum_{l'} \frac{\beta_{l'}}{\lambda_{l'}} v \Sigma_f \phi(\mathbf{r})}. \quad (3.9)$$

Then when a precursor generated at the steady-state simulation is forced to decay, its precursor family can be sampled from the decay probability starting from the initial steady-state fraction. The number density of precursor can be calculated by balancing the amount of precursor generation and the expected precursor loss due to forced decay in a time step.

$$\bar{w}_0^C = \bar{w}_N^C \frac{\overline{M_C}}{L_{C,N}} \quad (3.10)$$

$$\overline{M_C} = \frac{1}{N} \sum_{i=1}^N \sum_{j,k} M_{C,ijk} \quad (3.11)$$

$$L_{C,i} = \sum_j \frac{1}{\Delta T_i} \int_{T_i}^{T_{i+1}} w_{d,ij}(t) dt = \sum_j \bar{w}_i^C \sum_l f_{lj} (e^{-\lambda_{l,j}(T_i - t_{0,j})} - e^{-\lambda_{l,j}(T_{i+1} - t_{0,j})}) \quad (3.12)$$

In the above equations, the subscript  $C$  indicates precursor and  $N$  is the number of precursor generation steps.  $\bar{w}_0^C$  and  $\bar{w}_N^C$  are the average weight of precursors at the steady-state and the average weight of precursors at the  $N$ -th time step.  $\overline{M_C}$  is the average amount of precursor generation and  $L_{C,i}$  is the expected amount of precursor loss in the  $i$ -th time step. Then the precursor weight at the steady-state can be calculated by the equation (3.10).

### 3.3. Moving Geometry Treatment

To deal with the realistic transient scenarios such as control rod withdrawal or insertion, the geometry in the TDMC simulation should be treated continuously in time. The most of the MC codes deal with geometry as a boundary representation (B-Rep) which a cell is expressed as the intersections of the surrounding surfaces, and each surface is represented by coefficients according to a type of the surface. Then moving geometry can be expressed with the time-dependent coefficients for the surface equation.

$$f(x, y, z, t) = 0 \quad (3.13)$$

The geometry information is used in the flight kernel to calculate the distance to surface and to find the next cell to be linked after the flight. Since the energy and

direction of a neutron during  $k$ -th flight are not changed, the position of the neutron is expressed as a function of time as

$$\mathbf{r}(t) = \mathbf{r}(t_{k-1}^{ij}) + s\mathbf{\Omega} = \mathbf{r}(t_{k-1}^{ij}) + (t - t_{k-1}^{ij})v(E_k^{ij})\mathbf{\Omega} \quad (t > t_{k-1}^{ij}). \quad (3.14)$$

Then  $x$ ,  $y$ , and  $z$  in the surface equation (3.13) are parameterized in time and the time a neutron crosses the surface can be calculated from the equation.

The figure below shows the flow chart of the McCARD transient analysis module. The steady-state TDMC simulation is divided into the fission source convergence step and the precursor generation step. After the fission source distribution is converged in the former step, precursors are sampled and stored for the initial steady-state modeling in the latter step. At the same time, the multiplication factor at the steady-state,  $k_0$ , is calculated which is used as a normalization factor of the fission neutron sampling (equation 3.6) in the transient simulation. At the end of the steady-state simulation, a transient scenario is set according to the user input, and the transient TDMC simulation is conducted with the continuously changing system parameters such as cross section, geometry or density.

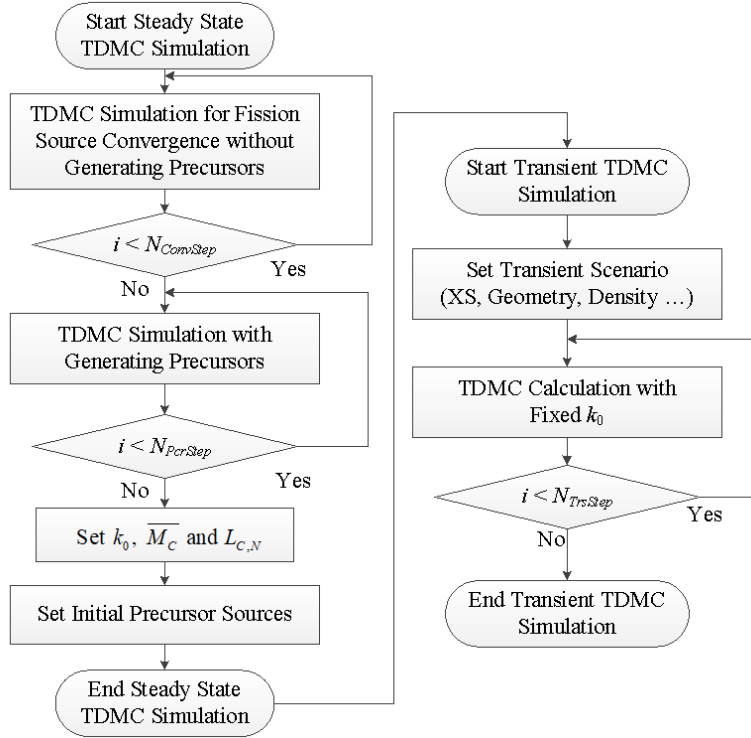


Figure 3.7 Flow chart of the McCARD transient analysis module

### 3.4. Numerical Results

McCARD transient analysis module is applied to the well-known C5G7-TD benchmark problems. The C5G7 core consists of 16  $\text{UO}_2$  and MOX fuel assemblies each of which has 17x17 configuration. Each assembly has 264 fuel pins, 24 guide tubes, and an instrumentation tube in the center. All pins are composed of two zones of the mixture inside a pin and the moderator surrounding it. Figure 3.8 shows the 2-D core configuration of the south-east quadrant. It can be seen the MOX assemblies have three enrichments of 4.3%, 7.0%, and 8.7%, and the core region is surrounded by water moderator.

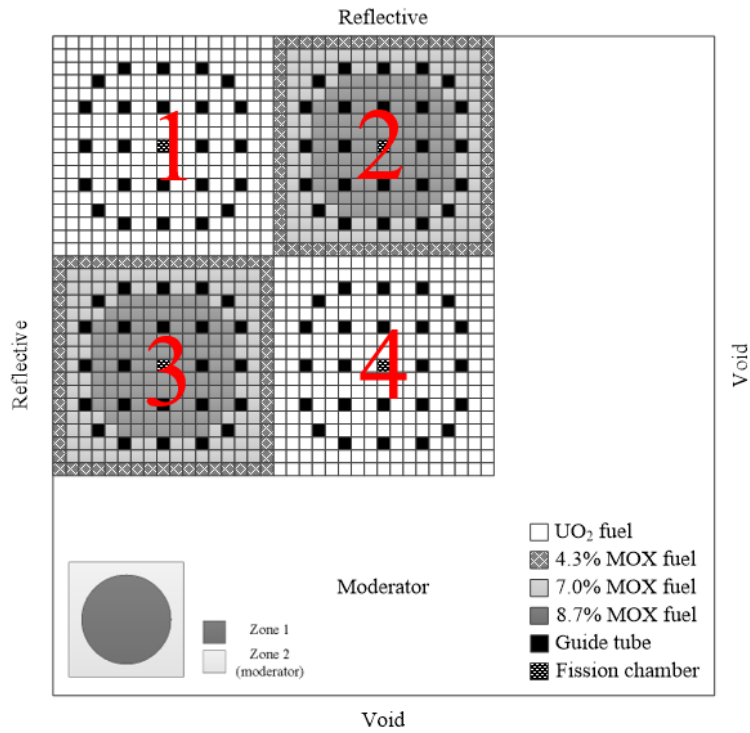


Figure 3.8 Radial core configuration of C5G7-TD benchmark

The axial core configuration is added with the 3-D extension. Additional water reflectors are added in both upper and lower regions of the active core, and the guide tubes and an instrumentation tube are explicitly modeled in the upper reflector region. In the initial steady state condition, a control rod (CR) bank at each assembly is positioned at the boundary between the active core and the upper reflector region. The axial core configuration is depicted in Figure 3.9 and the dimensions of the core are given in Table 3.2.

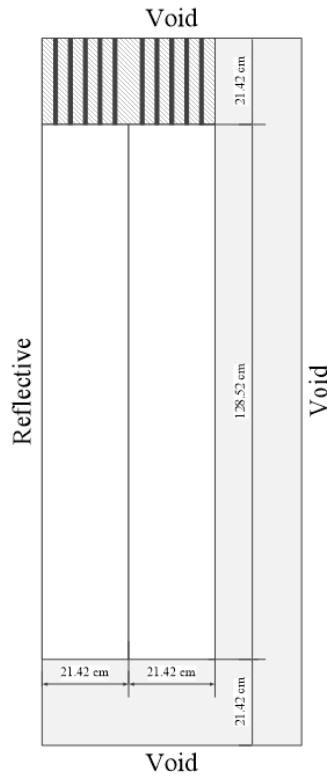


Figure 3.9 Axial core configuration of C5G7-TD benchmark

Table 3.2 Dimensions of C5G7-TD benchmark

Contents	Value [cm]
Pin radius	0.54
Pin pitch	1.26
Assembly pitch	21.42
Radial moderator width	21.42
Active core height	128.52
Axial reflector thickness	21.42

Among the problems, TD0 and TD4 problems are selected for the verification of the McCARD transient analysis module. TD0 is a set of 2-D transient problems with the postulated instantaneous CR insertion and withdrawal of designated CR banks. In 2-

D problems, the insertion and withdrawal of CR banks are modeled by the mixing of control rod and guide materials as

$$\Sigma_{rg}^{GTM}(t) = \begin{cases} \Sigma_{rg}^{GT}, & t = 0, t \geq 2 \text{ s} \\ \Sigma_{rg}^{GT} + 0.1(\Sigma_{rg}^R - \Sigma_{rg}^{GT}), & 0 \text{ s} < t \leq 1 \text{ s} \\ \Sigma_{rg}^{GT} + 0.05(\Sigma_{rg}^R - \Sigma_{rg}^{GT}), & 1 \text{ s} \leq t < 2 \text{ s} \end{cases} \quad (3.15)$$

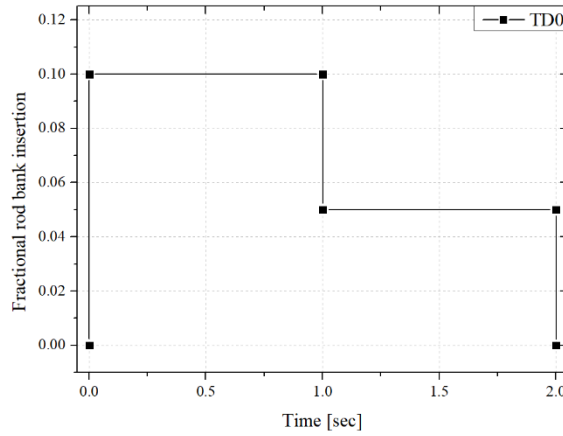


Figure 3.10 Transient scenario of TD0 problems

TD0 problems consist of 5 subsets each of which has different locations where the control rod movements occur.

- TD0-1: insertion/withdrawal of bank 1
- TD0-2: insertion/withdrawal of bank 3
- TD0-3: insertion/withdrawal of bank 4
- TD0-4: insertion/withdrawal of bank 1, 3, and 4 simultaneously
- TD0-5: insertion/withdrawal of bank 1-4 simultaneously

McCARD calculation is done with 50,000 neutrons and 50,000 precursors per time step. 100 fission source convergence steps and 500 precursor generation steps are used with 0.5 ms time interval. The core dynamic reactivity and fractional core

fission rate are calculated and compared with nTRACER results. Figure 3.11 and 3.12 show the comparison results of core dynamic reactivity and fractional core fission rate from 0 to 3 seconds. It should be noted that the uncertainties of the tally values are calculated from the history-based batch method which will be covered in the next chapter. The error bars in the figures indicate  $2\sigma$  values calculated with 50 number of batches. All results show good agreement with nTRACER results presenting the corresponding drops and recoveries according to the extent of reactivity insertion. Figure 3.13 and 3.14 are the assembly-wise fractional fission rates of TD0-3 and TD0-5 problem for 10 seconds. McCARD results also match well with nTRACER's within stochastic errors showing the trends of relative fission rates among the assemblies.

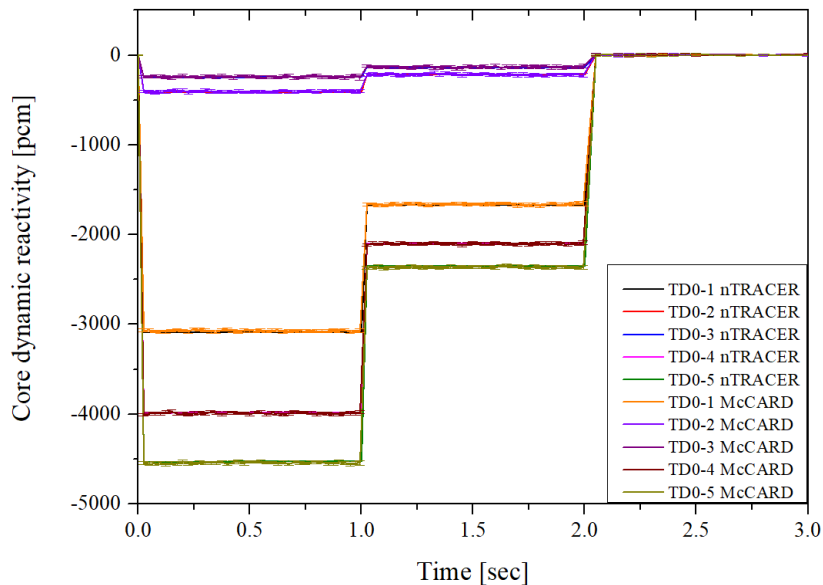


Figure 3.11 Core dynamic reactivity of TD0 problems



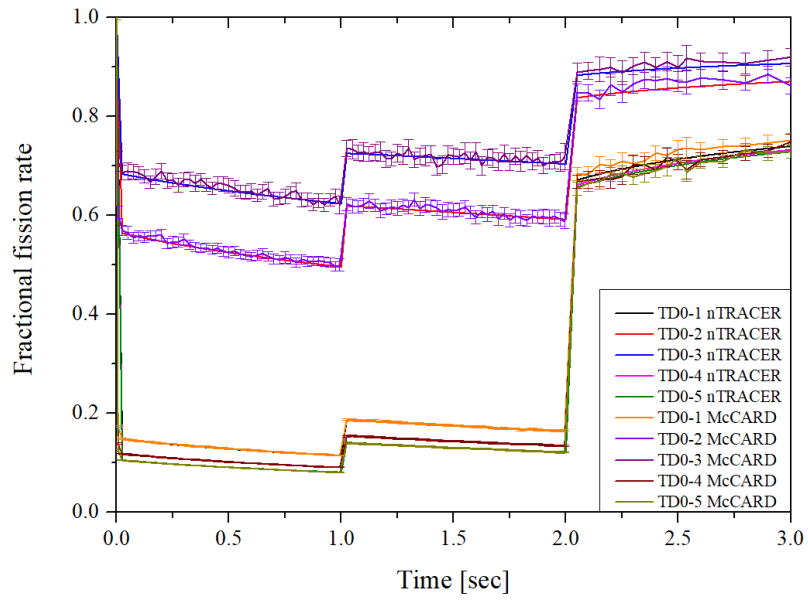


Figure 3.12 Fractional core fission rate of TD0 problems

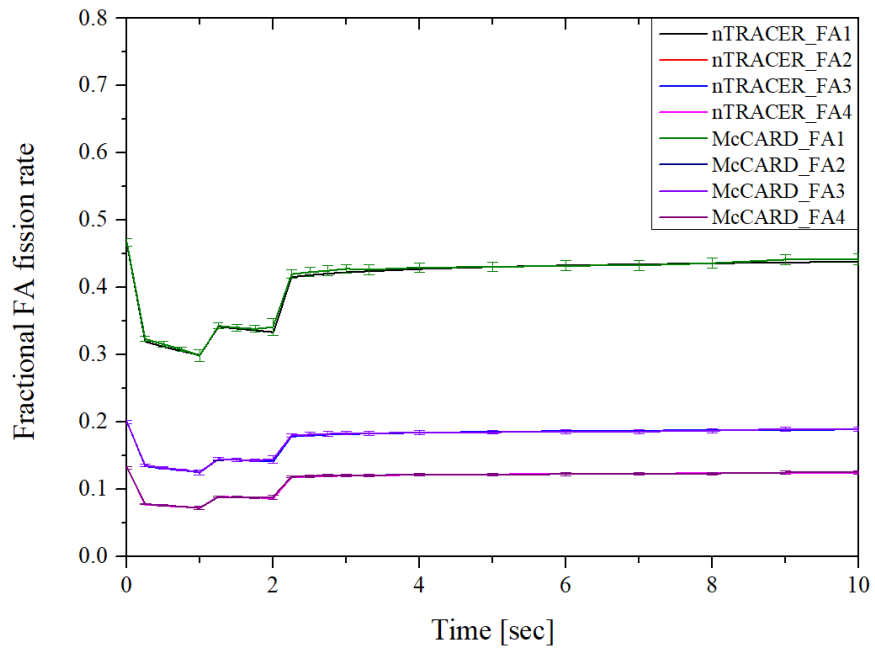


Figure 3.13 Assembly-wise fractional fission rate of TD0-3

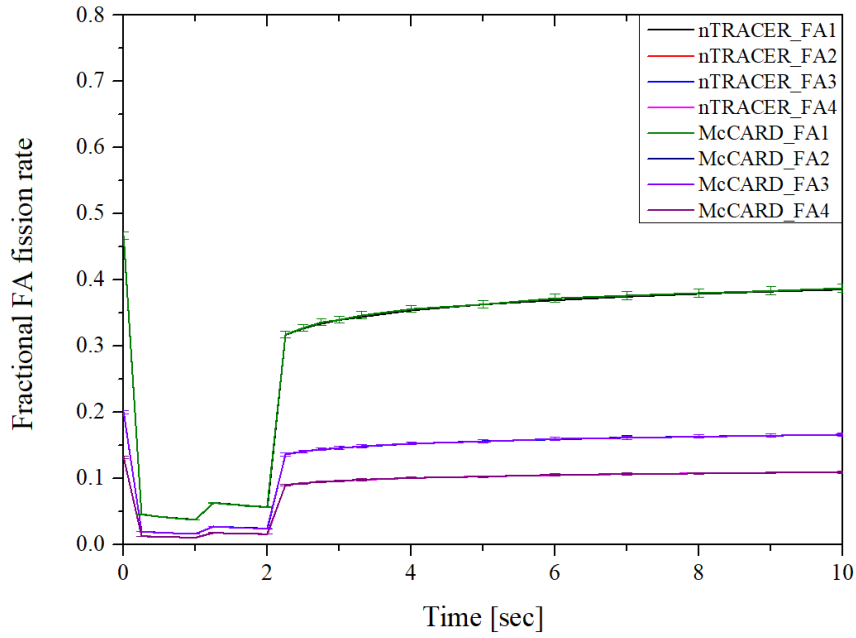


Figure 3.14 Assembly-wise fractional fission rate of TD0-5

TD4 problems postulate 3-D movements of the explicitly modeled control rods from the upper region. Four individual CR banks are inserted and withdrawn according to their transient scenarios. Among the problems, TD4-1, TD4-3, and TD4-4 are selected for the verification, and their transient scenarios are given below.

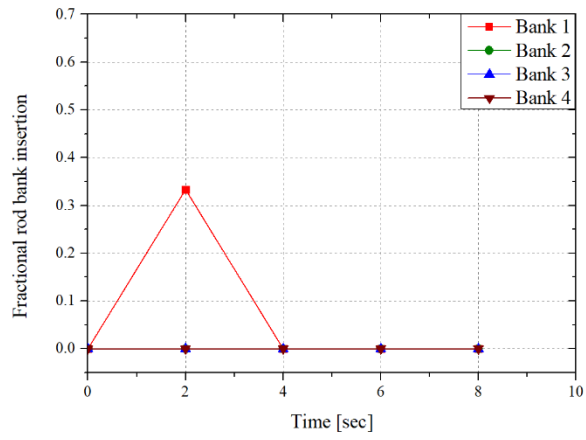


Figure 3.15 Transient scenario of TD4-1

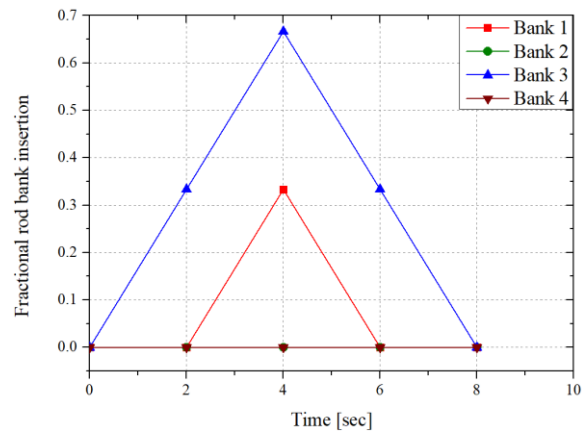


Figure 3.16 Transient scenario of TD4-3

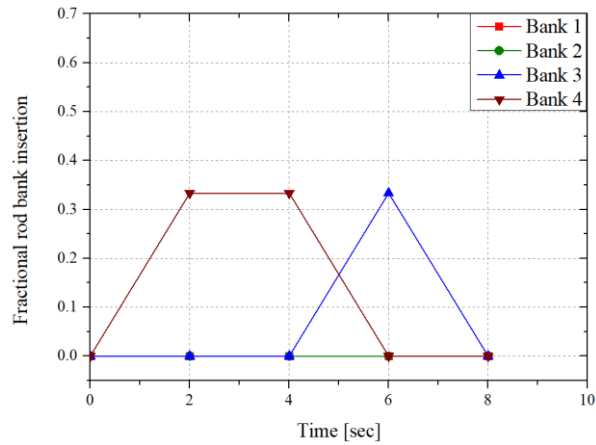


Figure 3.17 Transient scenario of TD4-4

McCARD transient calculation is conducted with 50,000 number of neutrons and precursors. The number of convergence step and precursor generation step are set to 100 and 500 respectively with its time interval of 0.5 ms. In the same manner, the core dynamic reactivity and fractional core fission rate are compared with nTRACER results and given in the figures below. For TD4-1 and TD4-3, the dynamic reactivity is decreased and increased according to the insertion and withdrawal of the CR bank 1 and 3 showing the lowest values at 2.0 and 4.0 seconds respectively. The corresponding fission rate also shows the lowest values at 2 and 4 seconds but slower restoration than the drop rate. As for TD4-4, more complicate reactivity and fission rate changes appear including the offsetting between the CR bank 3 and 4 from 4.0 to 6.0 seconds. In all cases, McCARD results match well with nTRACER results within stochastic errors. The axial distribution and trend of fission rate at the top of each fuel assembly are also given in Figure 3.20 to 3.25, and they also give consistent results.

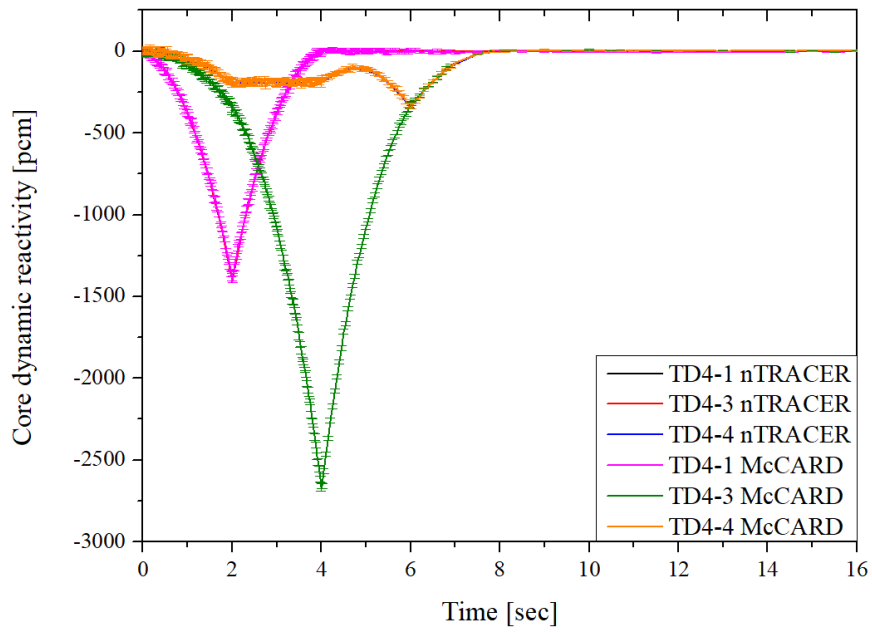


Figure 3.18 Core dynamic reactivity of TD4 problems

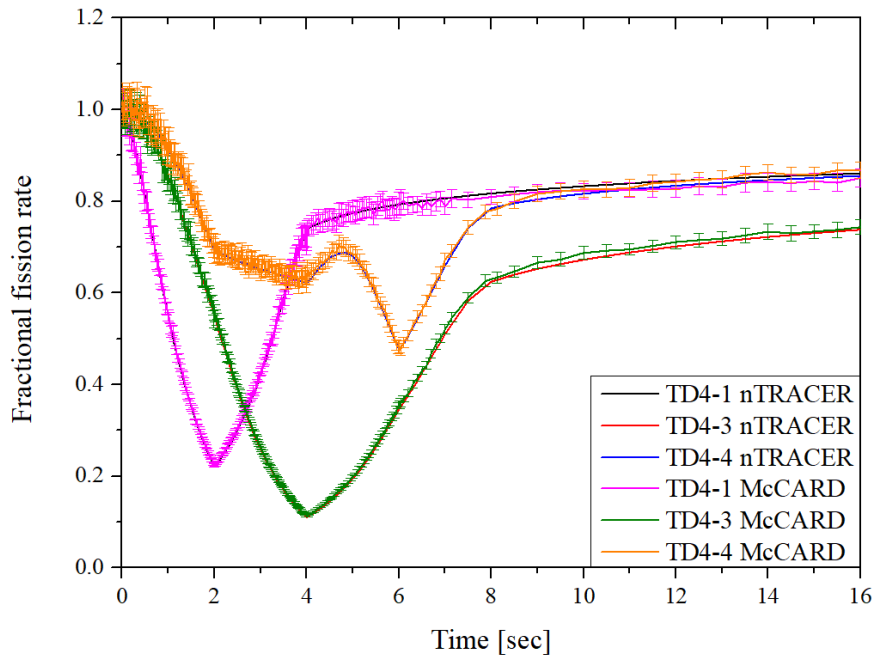


Figure 3.19 Fractional core fission rate of TD4 problems

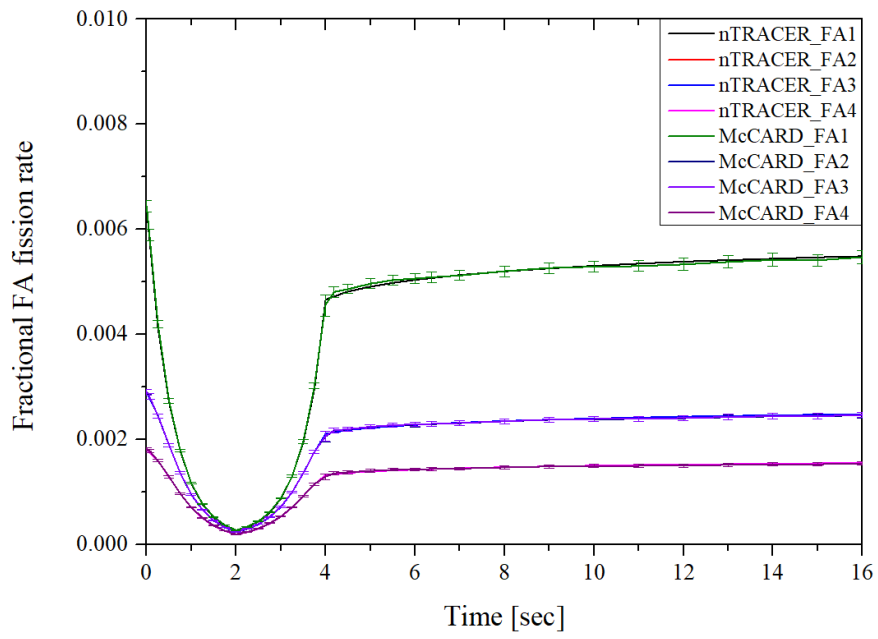


Figure 3.20 Trend of assembly-wise fractional fission rate at the top layer (TD4-1)

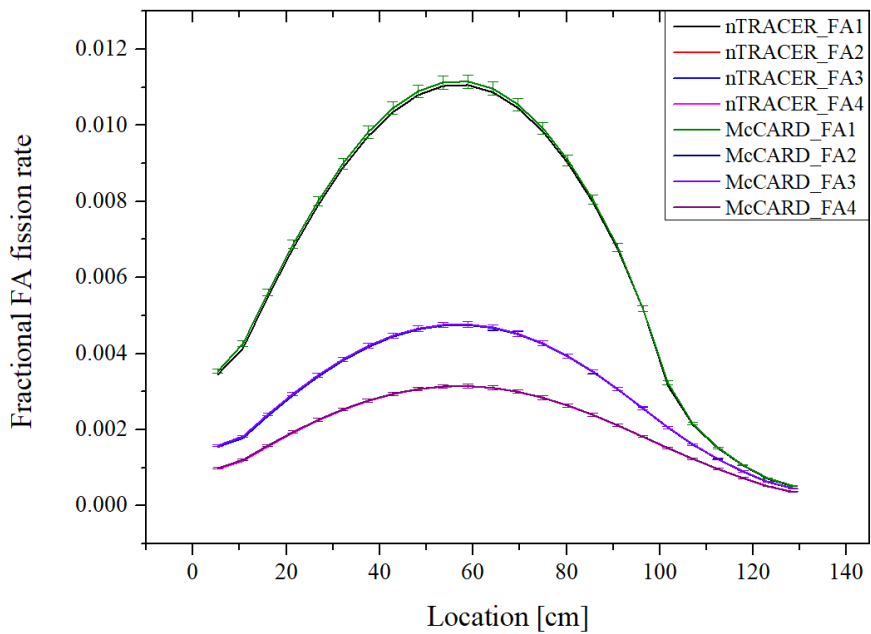


Figure 3.21 Distribution of assembly-wise fractional fission rate  
at 1.5 seconds (TD4-1)

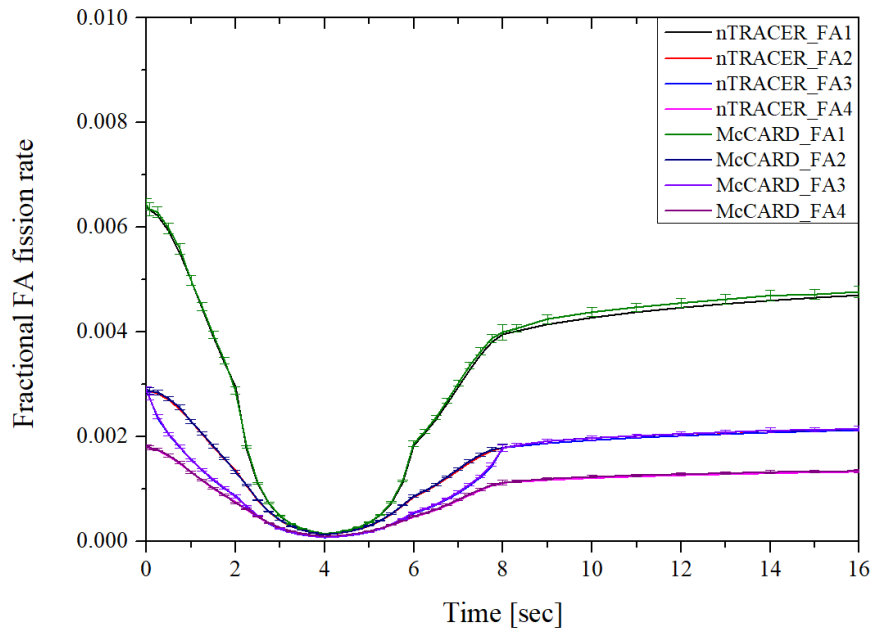


Figure 3.22 Trend of assembly-wise fractional fission rate at the top layer (TD4-3)

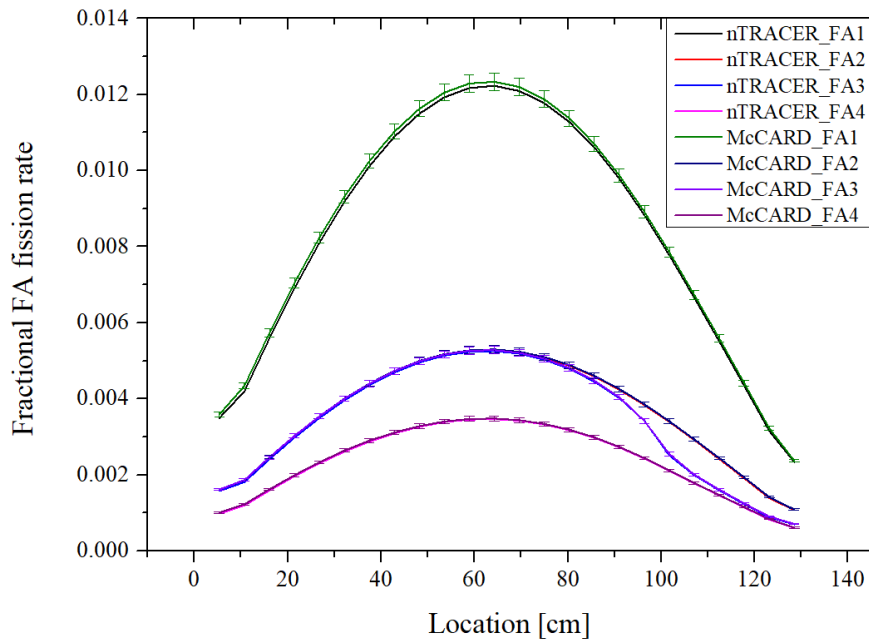


Figure 3.23 Distribution of assembly-wise fractional fission rate  
at 6.5 seconds (TD4-3)

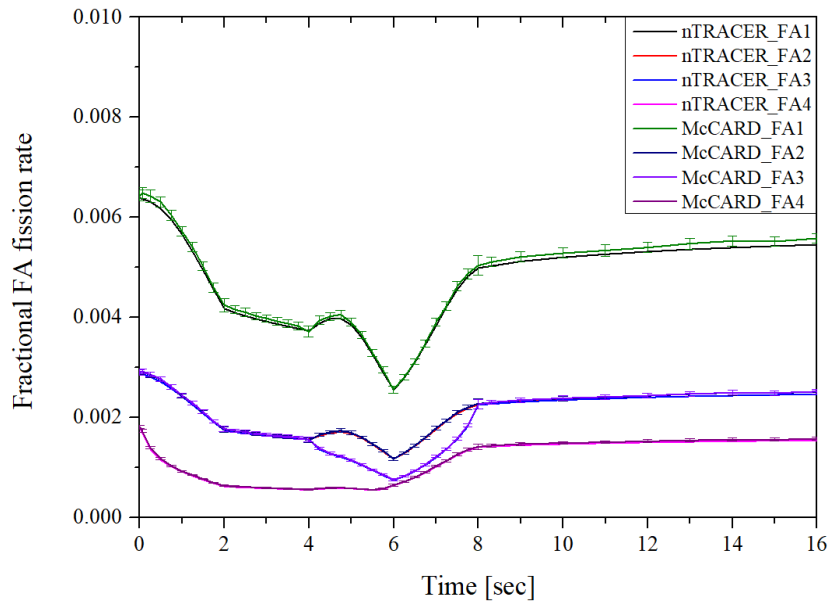


Figure 3.24 Trend of assembly-wise fractional fission rate at the top layer (TD4-4)

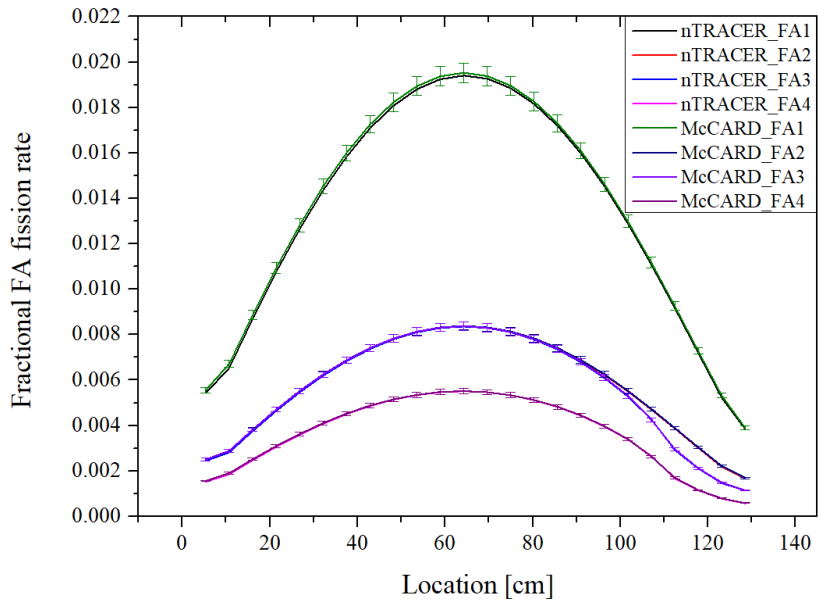


Figure 3.25 Distribution of assembly-wise fractional fission rate  
at 5.0 seconds (TD4-4)



## Chapter 4. Real Variance Estimation in TDMC Simulation

### 4.1. Bias of the Sample Variance in TDMC Simulation

The bias of the sample variance originates from the covariance terms between tally estimates and it can be derived in the same way as in the conventional MC  $k$ -eigenvalue calculation. Let  $Q_{ij}^m$  be the MC estimate of a tally  $Q$  from the  $j$ -th history in the  $i$ -th time step which is included in the  $m$ -th tally bin. The tally bin index  $m$  is introduced because a tally bin can contain multiple time steps depending on the user's needs. Then the tally mean of the  $m$ -th tally bin and its sample variance can be written as

$$\bar{Q}^m = \frac{1}{NM} \sum_i \sum_j Q_{ij}^m, \quad (4.1)$$

$$\sigma_s^2[\bar{Q}^m] = \frac{1}{NM(NM-1)} \sum_i \sum_j (Q_{ij}^m - \bar{Q}^m)^2, \quad (4.2)$$

where the  $M$  and  $N$  are the number of time steps included in the  $m$ -th time step and the number of histories in each time step. The variance bias is defined as the difference between the real variance and the apparent variance which is the expected value of the sample variance. From the definition, the real variance and the apparent variance of a tally mean in TDMC simulation are given by

$$\begin{aligned}
\sigma_R^2[\bar{Q}^m] &= E[(\bar{Q}^m)^2] - E[\bar{Q}^m]^2 = E\left[\left(\frac{1}{NM} \sum_i \sum_j Q_{ij}^m\right)^2\right] - E\left[\frac{1}{NM} \sum_i \sum_j Q_{ij}^m\right]^2 \\
&= \frac{NM}{(NM)^2} E[(Q_{ij}^m)^2] + \frac{1}{(NM)^2} \sum_{i,j} \sum_{i',j' \neq i,j} E[Q_{ij}^m Q_{i'j'}^m] \\
&\quad - \frac{NM}{(NM)^2} E[Q_{ij}^m]^2 - \frac{1}{(NM)^2} \sum_{i,j} \sum_{i',j' \neq i,j} E[Q_{ij}^m] E[Q_{i'j'}^m] \\
&= \frac{1}{NM} \sigma^2[Q_{ij}^m] + \frac{1}{(NM)^2} \sum_{i,j} \sum_{i',j' \neq i,j} \text{cov}[Q_{ij}^m, Q_{i'j'}^m]
\end{aligned} \tag{4.3}$$

$$\begin{aligned}
\sigma_A^2[\bar{Q}^m] &= E[\sigma_S^2[\bar{Q}^m]] \\
&= E\left[\frac{1}{NM(NM-1)} \sum_i \sum_j (Q_{ij}^m - \bar{Q}^m)^2\right] \\
&= \frac{1}{NM(NM-1)} E\left[\sum_i \sum_j (Q_{ij}^m - \bar{Q}^m)^2\right] \\
&= \frac{1}{NM-1} \left(E[(Q_{ij}^m)^2] - E[(\bar{Q}^m)^2]\right) \\
&= \frac{1}{NM-1} \left(E[(Q_{ij}^m)^2] - E[Q_{ij}^m]^2 + E[Q_{ij}^m]^2 - E[(\bar{Q}^m)^2]\right) \\
&= \frac{1}{NM-1} \left(\sigma^2[Q_{ij}^m] + E[Q_{ij}^m]^2 - E[(\bar{Q}^m)^2]\right)
\end{aligned} \tag{4.4}$$

where  $E[\cdot]$  is the expected value of an arbitrary variable in the bracket and

$\text{cov}[Q_{ij}^m, Q_{i'j'}^m]$  is the covariance between tally estimates  $Q_{ij}^m$  and  $Q_{i'j'}^m$ . In equation

(4.4), the last term can be rearranged as

$$\begin{aligned}
E[(\bar{Q}^m)^2] &= E\left[\left(\frac{1}{NM} \sum_i \sum_j Q_{ij}^m\right)^2\right] \\
&= \frac{NM}{(NM)^2} E[(Q_{ij}^m)^2] + \frac{1}{(NM)^2} \sum_{i,j} \sum_{i',j' \neq i,j} E[Q_{ij}^m, Q_{i'j'}^m] \\
&= \frac{1}{NM} E[(Q_{ij}^m)^2] + \frac{NM-1}{NM} E[Q_{ij}^m]^2 \\
&\quad + \frac{1}{(NM)^2} \sum_{i,j} \sum_{i',j' \neq i,j} (E[Q_{ij}^m, Q_{i'j'}^m] - E[Q_{ij}^m] E[Q_{i'j'}^m]) \\
&= \frac{1}{NM} \sigma^2[Q_{ij}^m] + E[Q_{ij}^m]^2 + \frac{1}{(NM)^2} \sum_{i,j} \sum_{i',j' \neq i,j} \text{cov}[Q_{ij}^m, Q_{i'j'}^m]
\end{aligned} \tag{4.5}$$

By substituting equation (4.5) into equation (4.4) and subtracting it from equation (4.3), the variance bias can be expressed in covariance terms between neutrons within the tally bin.

$$\begin{aligned}
& \sigma_R^2[\bar{Q}^m] - \sigma_A^2[\bar{Q}^m] \\
&= \left( \frac{1}{NM} \sigma^2[Q_{ij}^m] + \frac{1}{(NM)^2} \sum_{i,j} \sum_{i',j' \neq i,j} \text{cov}[Q_{ij}^m, Q_{i'j'}^m] \right) \\
&\quad - \left( \frac{1}{NM} \sigma^2[Q_{ij}^m] - \frac{1}{NM-1} \frac{1}{(NM)^2} \sum_{i,j} \sum_{i',j' \neq i,j} \text{cov}[Q_{ij}^m, Q_{i'j'}^m] \right) \quad (4.6) \\
&= \frac{1}{NM(NM-1)} \sum_{i,j} \sum_{i',j' \neq i,j} \text{cov}[Q_{ij}^m, Q_{i'j'}^m]
\end{aligned}$$

The sample variance of a tally mean is usually estimated by statistically processing the contributions per neutron. In the fixed source mode simulation, all the initial neutron sources are guaranteed to be independent of each other and thus the derived tallies are uncorrelated. In the TDMC simulation, however, the neutrons become highly correlated to each other as the simulation proceeds. This correlation stems from the branching process and the population control scheme. The neutrons originated from the branching process such as  $(n, fis)$ ,  $(n, 2n)$ , and  $(n, 3n)$  reactions share the same ancestors, and thereby their progenies are correlated to each other. Such genealogical correlation naturally occurs in all MC simulations and it becomes problematic when neutrons are treated as independent ones after a normalization scheme such as cycle-by-cycle FSD updates in the  $k$ -eigenvalue calculation. In TDMC simulation, the population control algorithm exactly corresponds to this. At the end of each time step, the survival neutrons which may have common ancestors are discarded or split into identical neutrons to maintain the effective number of neutrons. Besides, the weight of neutrons after the population control is normalized to have the same weight, which also makes a correlation between neutrons, as

$$\bar{w}_{i+1} = \frac{\sum_{j=1}^{n_{s,i}} w_{ij}}{N}, \quad (4.7)$$

where  $n_{s,i}$  indicates the number of survival neutrons at the end of the  $i$ -th time step. Therefore, the tallies from these correlated or identical neutrons are not independent and their statistical process causes a variance bias. In addition to the occurrence of the correlation between neutrons, there is another problem in allocating tally contributions from delayed neutrons. In TDMC simulation, the delayed neutrons are treated by the forced decay algorithm, which samples a precursor instead of a delayed neutron at the fission events and forces it to decay and make a contribution at each time interval. Even if the neutrons and precursors are numbered from the beginning of the simulation, it is difficult to properly allocate these contributions because there may be no survival neutrons sharing common ancestors, or the number of delayed neutrons and survival neutrons may not match.

## 4.2. History-based Batch Method in TDMC Simulation

There have been several approaches to estimate real variance in the conventional  $k$ -eigenvalue calculation, such as Gelbard's batch method [29], Ueki's inter-cycle covariance estimation method [30], fission source distribution inter-cycle correlation method [31] and history-based batch method [17]. Among the methods, the history-based batch method simply but effectively gets rid of the correlation between tally estimates by grouping histories in a genealogical way without directly calculating covariance terms.

To estimate an unbiased variance of a tally mean, a history-based batch method

is developed for TDMC simulation. The basic concept of the method is to group neutrons and precursors into different batches which do not interfere with each other throughout the simulation to eliminate the correlation between tallies. Figure 4.1 shows the schematic diagram of the history-based batch method in TDMC simulation.  $n_{i,j}$ ,  $d_{i,j}$  and  $C_{i,j}$  indicate the  $j$ -th survival neutron, delayed neutron and precursor in the  $i$ -th time step.  $N$  and  $N_C$  are the total number of neutrons and precursors.  $N_B$  is the number of batches. At the beginning of the simulation, the neutrons are divided into equal numbers and grouped into batches as indicated by boxes in the figure. The neutrons and precursors are simulated within each batch throughout the simulation. The solid lines present the tracks of each particle while the dot lines present the generation of precursors and delayed neutrons from the forced decay algorithm. At the end of each time step, the number of neutrons and precursors are controlled to maintain the population. One can see that all the simulation schemes including the delayed neutron treatment and population control are applied batch-wisely.

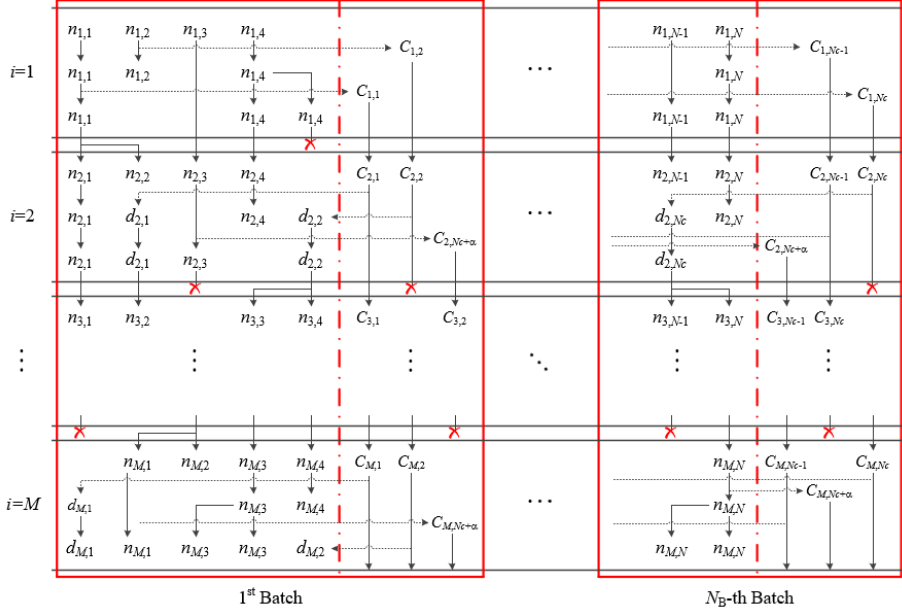


Figure 4.1 Schematic diagram of the history-based batch method in TDMC

Then the mean of a tally and its variance can be estimated from the batch-average tally results as

$$Q_i^\kappa = \frac{1}{N/N_B} \sum_{j \in \kappa} Q_{ij} \quad (\kappa = 1, 2, \dots, N_B), \quad (4.8)$$

$$\sigma^2[\bar{Q}_{i,HB}] = \frac{1}{N_B(N_B - 1)} \sum_{\kappa=1}^{N_B} (Q_i^\kappa - \bar{Q}_{i,HB}), \quad (4.9)$$

$$\bar{Q}_{i,HB} = \frac{1}{N_B} \sum_{\kappa=1}^{N_B} Q_i^\kappa = \frac{1}{N} \sum_{\kappa=1}^{N_B} \sum_{j \in \kappa} Q_{ij}, \quad (4.10)$$

where  $i, j$ , and  $\kappa$  are the time step, history, and batch index.  $Q^{m\kappa}$  is the batch-average tally of the  $\kappa$ -th batch for the  $m$ -th tally bin. Since there is no correlation between the batch-average tallies, it is straightforward that the mean among the batches and its variance are unbiased estimates. In addition, the inconsistent allocation problem

of the delayed neutron contributions is naturally resolved by assigning contributions to the batch to which each delayed neutron belongs. The history-based batch method is exactly the same as the replica calculation, but it has an advantage in that the results can be estimated with a single calculation.

## 4.3. Numerical Results

### 4.3.1. Infinite Homogeneous Two-group Problems

The developed history-based batch method is verified to infinite homogeneous two-group problems. A subcritical problem and a supercritical problem with  $k_{\text{inf}}$  values of 0.99900 and 1.00200, respectively, are chosen for the verification. The two-group cross section data are presented in Table 4.1. McCARD TDMC calculation is conducted with 1,000,000 neutron histories for 100.0 ms with 0.1 ms time interval varying the size of batches. Only prompt neutrons are simulated and the initial sources are set to be 1 group. For the reference calculation, 100 replica calculations are done with 10,000 neutron histories and the same time conditions.

Table 4.1 Two-group cross section data

Cross section	First group ( $g=1$ )	Second group ( $g=2$ )
$\Sigma_{tg}$	0.50000	1.30000
$\Sigma_{fg}$	0.00100	0.09000
$\nu_g$	2.40000	2.40000
$\Sigma_{sgg}$	0.48000	1.09000
$\Sigma_{sg'g}$	$1.69430 \times 10^{-2} / 1.70000 \times 10^{-2}$	0.00190
$\chi_g$	1.00000	0.00000
$1/\nu_g$	$2.28626 \times 10^{-10}$	$1.29329 \times 10^{-6}$

Figure 4.2 shows the comparison results of the fission rate tally with different batch sizes in the subcritical case. The batch size is the number of neutrons allocated to each batch, so the batch size of 100 means the calculation of 10,000 batches with 100 neutrons in this case. From the figure, one can see that it fails to estimate the reference mean  $\bar{Q}^m$  when the batch size is lower than 250 because the number of samples is too small that the batch estimates  $Q^{mk}$  do not follow the normal distribution. On the other hand, when the batch is larger than 2,500, the mean of batch estimates predicts the reference mean well within the stochastic error. Figure 4.3 presents the comparison results at 50 ms. In both figures, the  $1\sigma$  errors are indicated by the grey band for the reference calculation and error bars for other calculations.

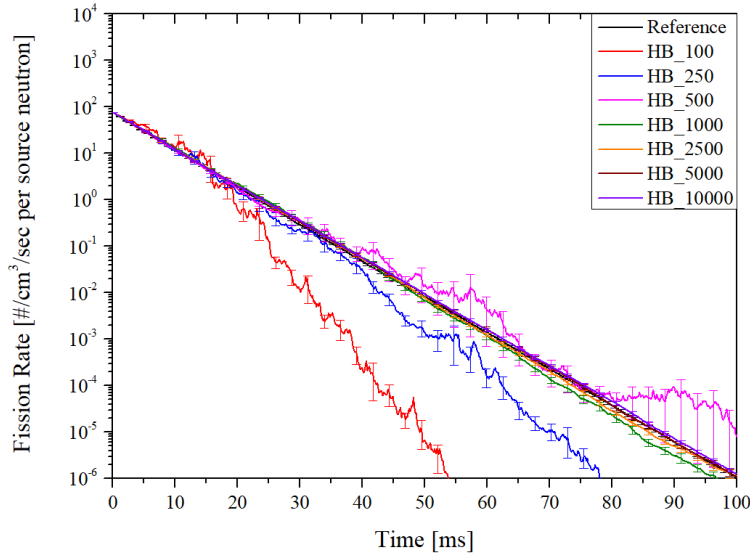


Figure 4.2 Comparison of  $\bar{Q}_{HB}$  trends according to the batch size (subcritical)



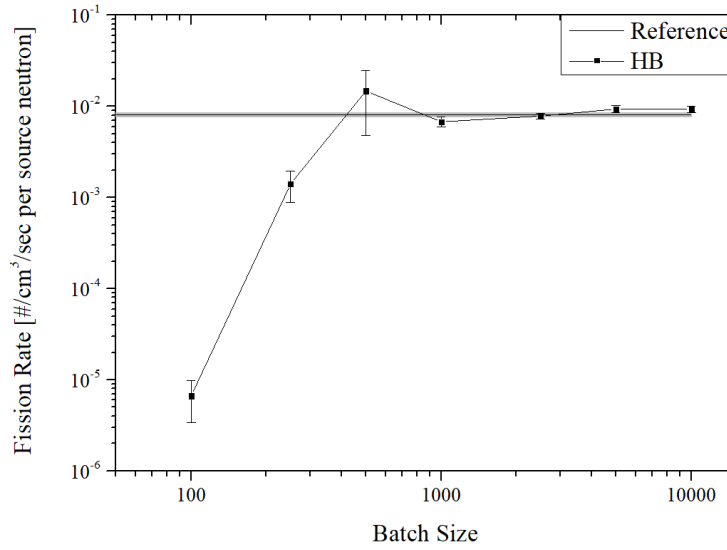


Figure 4.3 Comparison of  $\bar{Q}_{HB}$  at 50 ms according to the batch size (subcritical)

Figure 4.4 is the comparison results of the RSD of a tally mean with different batch sizes. The 90% confidence interval of the RSD is depicted as the grey band for the reference calculation and marked as error bars for other calculations with the history-based batch method. The results with a batch size larger than 2,500 match well with the reference within the stochastic error, which is the consistent results with the previous estimation of the mean value. Figure 4.5 and 4.6 show the comparison of SDs according to the variance estimation method. The black line presents the reference result with  $1\sigma$  SDs depicted by the grey band while the red line and blue line show the results from the conventional method and the history-based batch method using the batch size of 10,000, respectively. In the conventional method, the SDs are estimated to be much smaller than the reference, so the results appear to not match within the stochastic error. However, the history-based batch method estimates the SDs in good agreement with the reference, showing a real to apparent SD ratio of nearly 1.

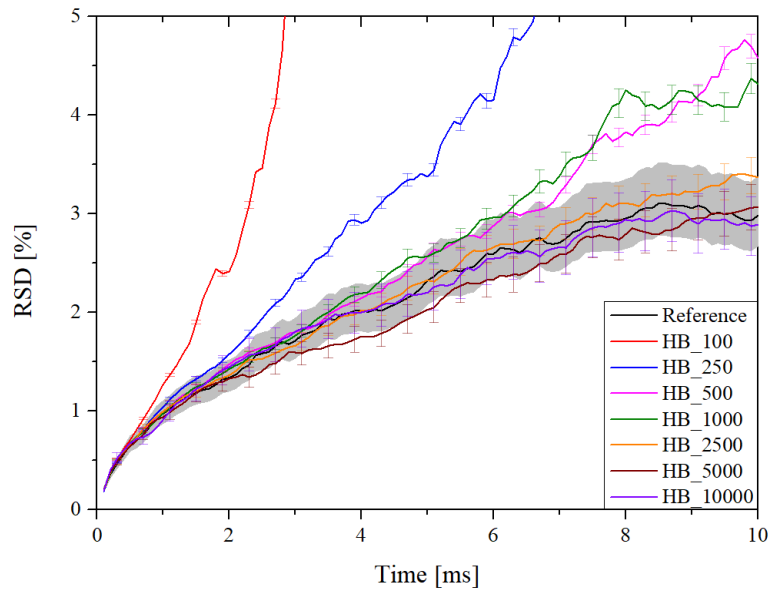


Figure 4.4 Comparison of RSD trends according to the batch size (subcritical)

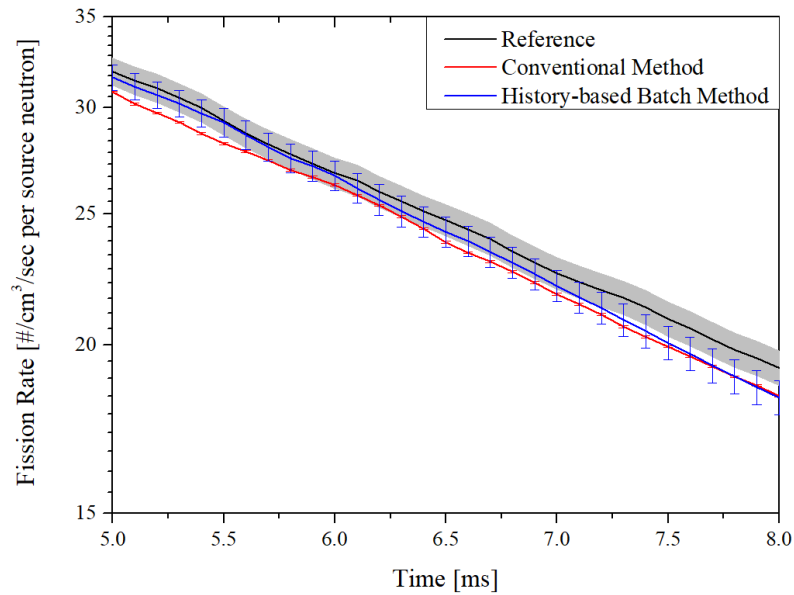


Figure 4.5 Comparison of the SDs according to the history-based batch method  
(subcritical)

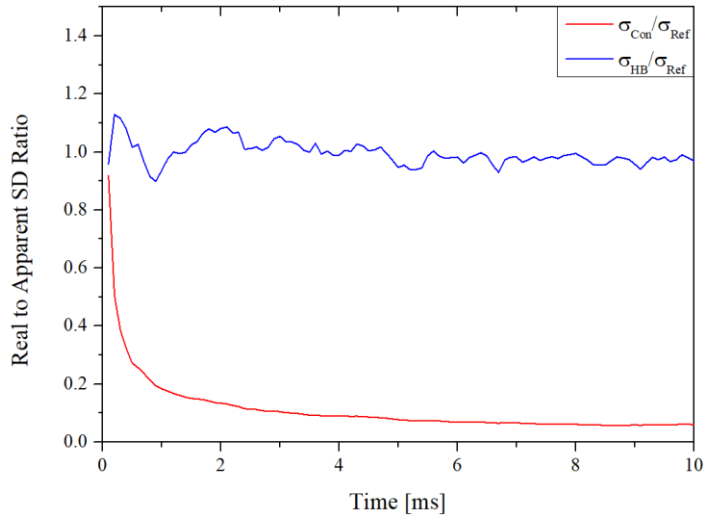


Figure 4.6 Comparison of the real to apparent SD ratio according to the history-based batch method (subcritical)

The verification of the history-based batch method for the supercritical problem is also conducted in the same way. Figure 4.7 to 4.11 are the corresponding results of the supercritical problem. When the size of batch is larger than 2,500, the tally mean and its RSD of the history-based batch method show good agreements with the reference results. The effectiveness of the proposed method is shown in comparison with the conventional method which far underestimates the SDs.

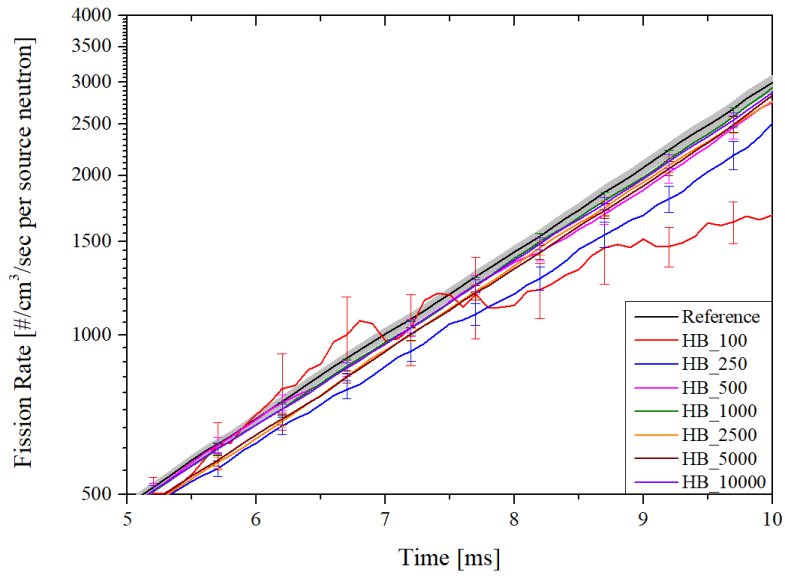


Figure 4.7 Comparison of  $\bar{Q}_{HB}$  trends according to the batch size (supercritical)

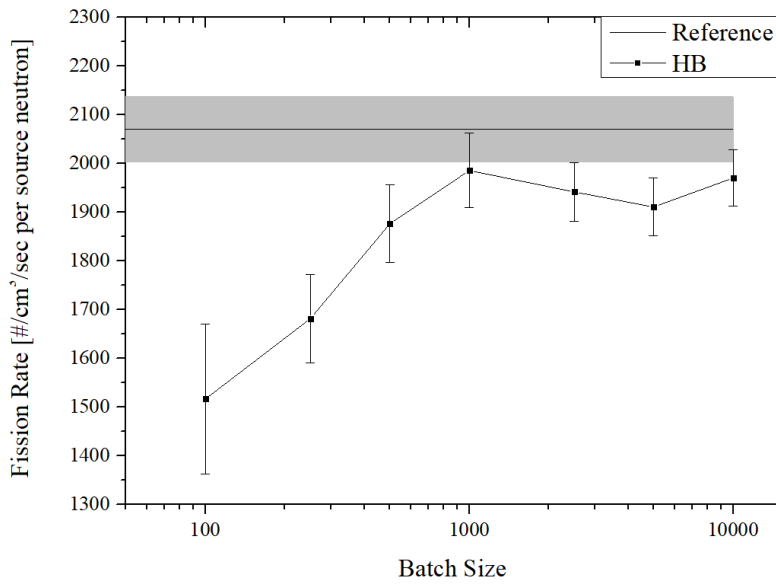


Figure 4.8 Comparison of  $\bar{Q}_{HB}$  at 9 ms according to the batch size (supercritical)

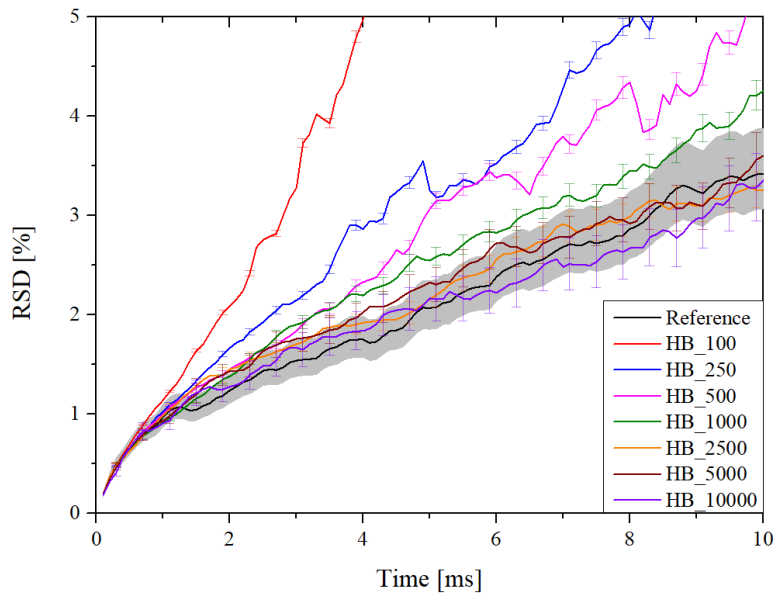


Figure 4.9 Comparison of RSD trends according to the batch size (supercritical)

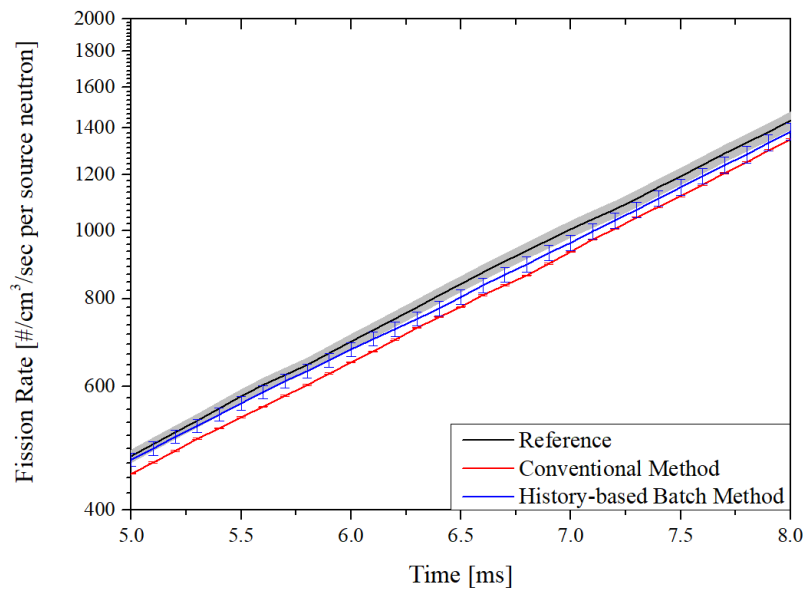


Figure 4.10 Comparison of the SDs according to the history-based batch method  
(supercritical)

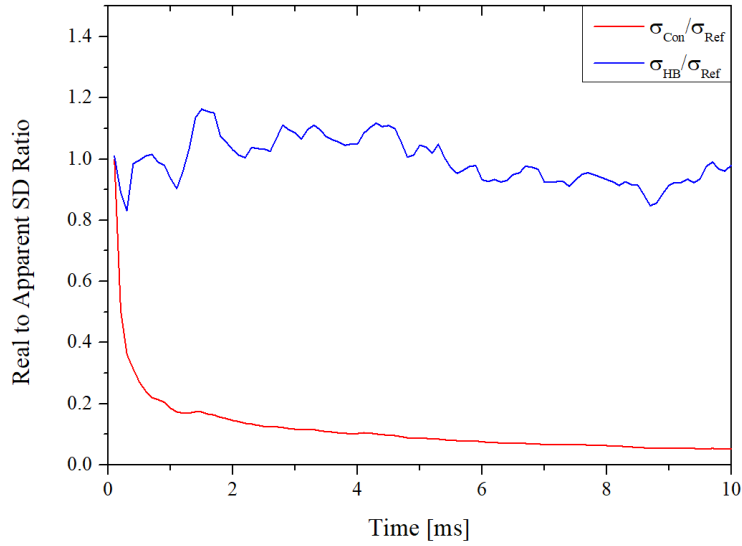


Figure 4.11 Comparison of the real to apparent SD ratio according to the history-based batch method (supercritical)

### 4.3.2. C5G7-TD Benchmark Problems

To consider the effect of the delayed neutrons, C5G7-TD benchmark problems are chosen for the verification and application of the developed method. For the verification, the TD0-5 problem is solved and the real variance of the fission rate is estimated. McCARD calculation is done with 500,000 neutrons and precursors with the time interval of 0.1 ms. The delayed neutrons are simulated using the forced decay algorithm and the simulation starts from the initial steady-state source distribution. For the reference calculation, 100 replica calculations with different random number sequence are conducted using 5,000 neutrons and precursors. The comparison results of the fission rate trend according to the batch size are given in Figure 4.12 and 4.13. Compared to the previous infinite homogeneous two-group problems, the tally mean matches well with the reference even in the case of the

relatively small batch size of 500. This can be inferred from that the previous problems are more extreme cases and the delayed neutrons alleviate the fluctuations among the batch results. Similar results are also found in the comparison of the RSDs in Figure 4.14 that all cases show good agreement with the reference RSD.

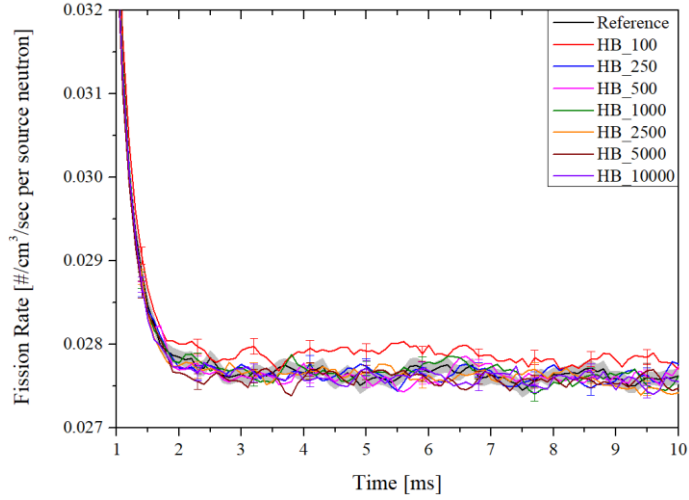


Figure 4.12 Comparison of  $\bar{Q}_{HB}$  trends according to the batch size with delayed neutrons (TD0-5)

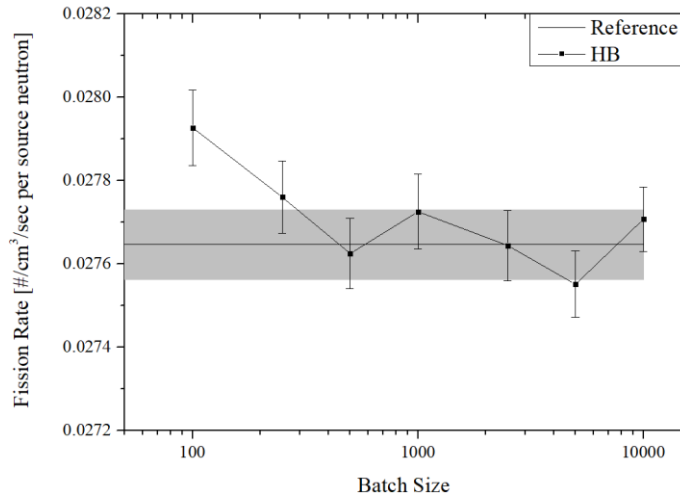


Figure 4.13 Comparison of  $\bar{Q}_{HB}$  at 3 ms according to the batch size with delayed neutrons (TD0-5)

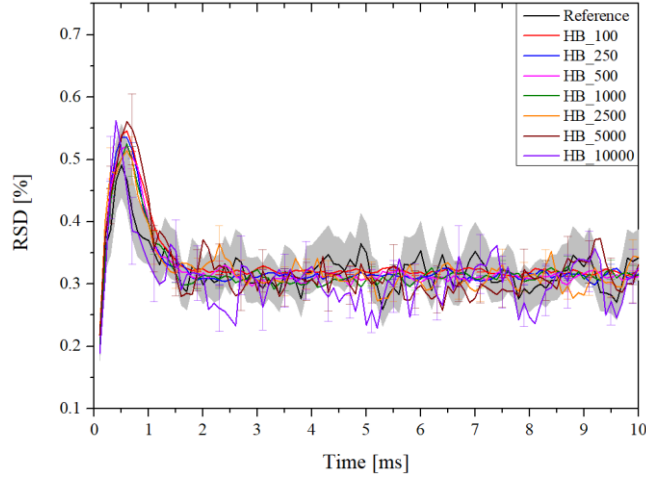


Figure 4.14 Comparison of RSD trends according to the batch size with delayed neutron (TD0-5)

The estimated tally mean and SD from the conventional method are presented in Figure 4.15 with the history-based batch method of 10,000 batch size. It should be noted that the contribution of a delayed neutron is randomly assigned to a neutron in the conventional method. The mean and SDs of the conventional method are quite well matched with the reference which means the correlation between tally estimates is relatively small if the delayed neutrons are simulated. This can be deduced by checking the number of independent branches from the start of the simulation. Figure 4.16 is the plot of the number of independent branches in the conventional method and history-based batch method according to the delayed neutron simulation. Without the delayed neutron, the independent branches keep decreasing from the source convergence step to the transient step. On the other hand, if the delayed neutrons are generated from the stored precursors in each time step, it has much more independent neutrons which reduces the correlation in the tally estimates. It can be also seen that the history-based batch method ensures the minimum number of



independent neutrons so that there will be less correlation. Figure 4.17 is the comparison of the real to apparent SD ratio. The dashed lines are the estimated variance with the 10 times longer tally bin which contains the tally estimates of 10 time steps. The history-based batch method estimates variance well in both cases while the conventional method shows underestimations of variance. When the variance is estimated with tally estimates over several time steps, the variance becomes more biased because the correlation is stronger.

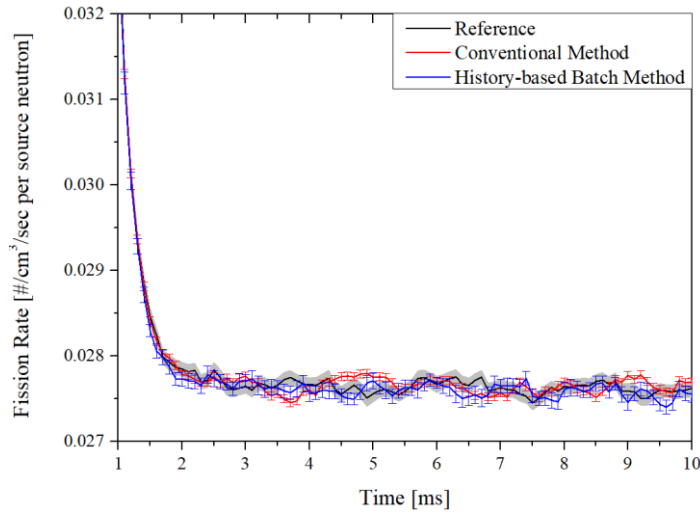


Figure 4.15 Comparison of the SDs according to the history-based batch method with delayed neutron (TD0-5)

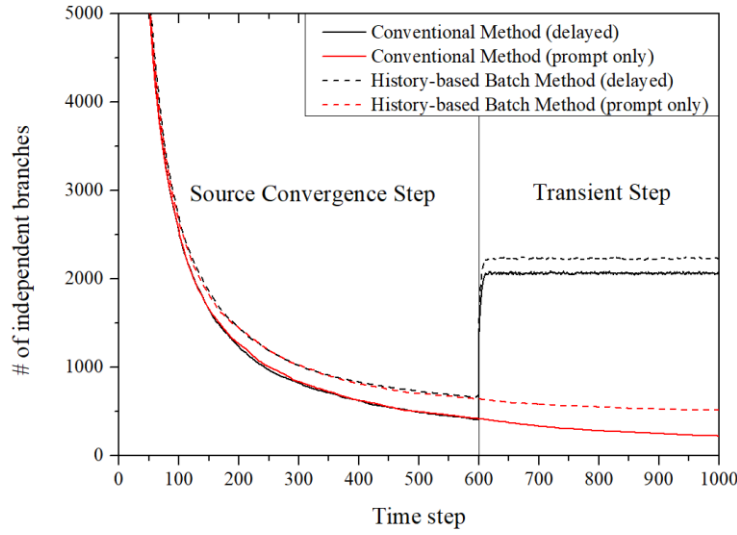


Figure 4.16 Trend of the number of independent branches (TD0-5)

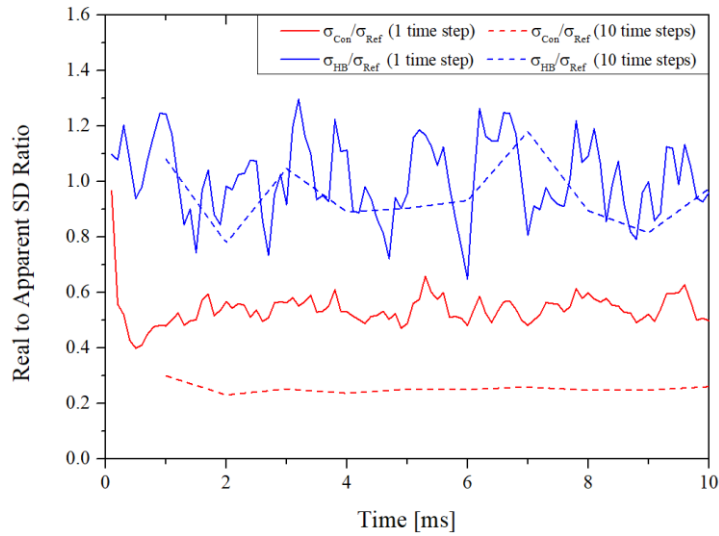


Figure 4.17 Comparison of the real to apparent SD ratio according to the history-based batch method with delayed neutron (TD0-5)

All results of the TDMC simulation in the previous chapters are calculated using the history-based batch method. One may obtain the biased results without using it. The fractional core fission rate of some C5G7-TD benchmark problems are presented in

comparison with the biased results from the conventional method.

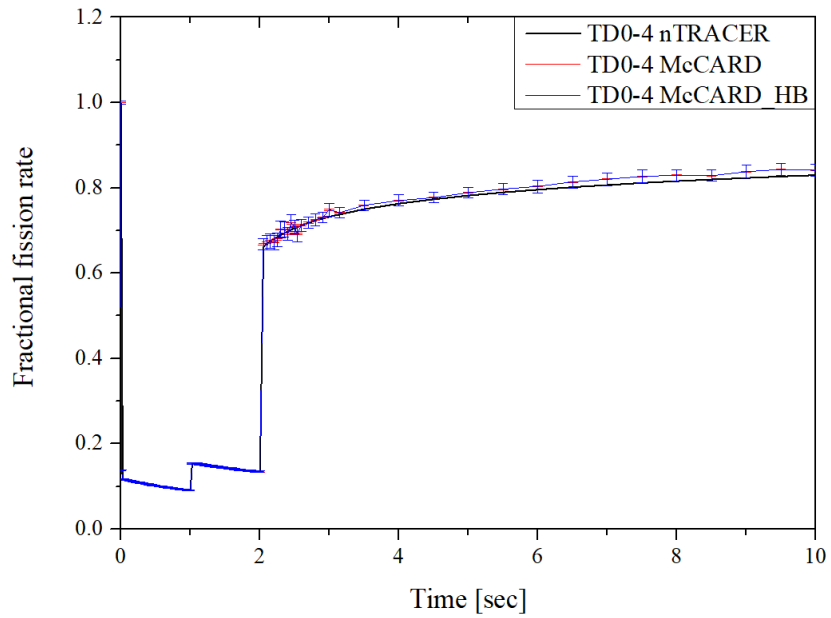


Figure 4.18 Comparison of the estimated variance in TD0-4 problem

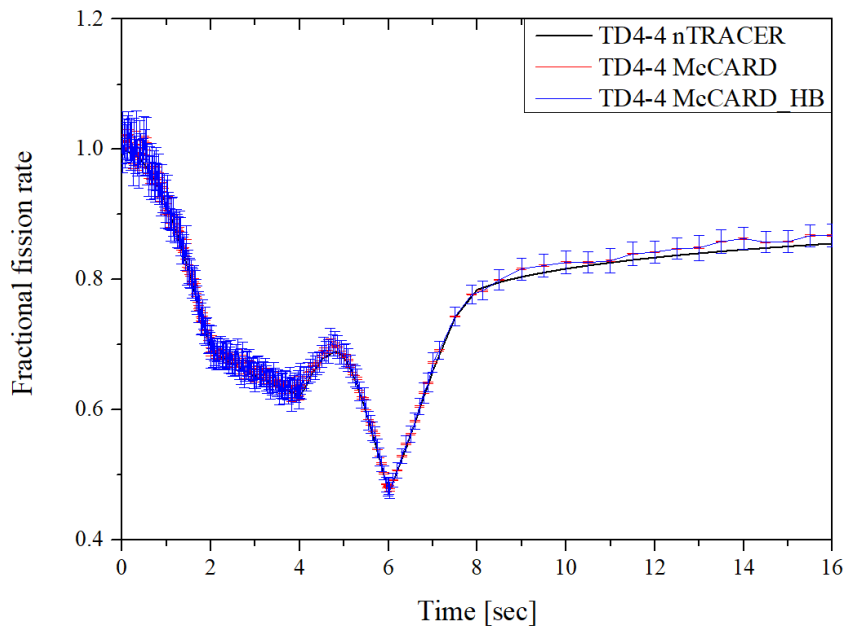


Figure 4.19 Comparison of the estimated variance in TD4-4 problem

From the comparison results, it is demonstrated that the history-based batch

method can effectively eliminate the correlation between neutrons and estimate the real variance. However, as shown in Figures 4.2, 4.7, and 4.12, a sufficient batch size is required to assure unbiased tally results from the history-based batch method. This is because the history-based batch method is based on the assumption that the mean of batch estimates follows the true mean value. So, if the batch size is not sufficient, the batch estimates do not follow the normal distribution and the assumption becomes invalid. The sufficient batch size is highly problem dependent and hard to know before the calculation. In addition, providing the tally mean and variance for various batch sizes is computationally expensive. Therefore, diagnostic methods are suggested to determine the suitability of a prescribed batch size using a posterior normality test.

Among the various normality tests, the Jarque-Bera test [32] and Lilliefors test [33] are selected for the evaluation. The Jarque-Bera test utilizes the skewness and the kurtosis of the  $n$  samples with the test statistic as

$$JB = \frac{n}{6} \left( S^2 + \frac{1}{4}(K-3)^2 \right) \sim \chi^2(2): \text{ under } H_0, \quad (4.11)$$

$$S = \frac{\mu_3}{\sigma^3} = \frac{\frac{1}{n} \sum_{i=1}^n (x_i - \bar{x})^3}{\left( \frac{1}{n} \sum_{i=1}^n (x_i - \bar{x})^2 \right)^{3/2}}, \quad (4.12)$$

$$K = \frac{\mu_4}{\sigma^4} = \frac{\frac{1}{n} \sum_{i=1}^n (x_i - \bar{x})^4}{\left( \frac{1}{n} \sum_{i=1}^n (x_i - \bar{x})^2 \right)^2}. \quad (4.13)$$

In the above equations,  $JB$ ,  $S$ , and  $K$  denotes the test statistic, skewness, and kurtosis

respectively. The null hypothesis is that the random variable  $x$  follows a normal distribution, and under this condition, the test statistic  $JB$  follows a chi-square distribution with 2 degrees of freedom. If the  $p$ -value of the test statistic is smaller than the set level of significance, the null hypothesis is rejected and the samples are regarded not to follow a normal distribution. On contrary, if the  $p$ -value is larger, the samples are regarded to follow a normal distribution because there is no evidence to reject the null hypothesis. The Lilliefors test is a normality test based on the Kolmogorov-Smirnov (K-S) test when the population mean and variance are unknown. It utilizes the maximum difference between the empirical distribution function and the cumulative distribution function which is a normal distribution having the same mean and variance in the normality test as

$$D_n = \sup |F_n(x) - F(x)|. \quad (4.14)$$

In the equation,  $F_n(x)$  and  $F(x)$  are the empirical distribution function with  $n$  samples and the corresponding normal distribution. From the Lilliefors test table, the critical value  $D_{n,\alpha}$  with the set level of significance can be obtained and compared to the  $D_n$ . If the  $D_n$  is smaller than the critical value, the samples are regarded to follow a normal distribution since it cannot reject the null hypothesis. In McCARD, both methods are implemented to give diagnosis results of the time-dependent tally. The significance level is set to 0.05 and its corresponding formulation for the critical value in Lilliefors test with the sample size larger than 50 is given as

$$D_{n,0.05} = 0.895 / \left( \frac{0.83 + n}{\sqrt{n}} - 0.01 \right). \quad (4.15)$$

The table below shows the diagnostic results regarding batch sizes in C5G7-TD0-5 problem. The total number of neutrons are fixed to 1,000,000 in all cases. From both results, the batch estimates are diagnosed to follow a normal distribution in cases when the batch size is larger than 500. Though the proposed methods can provide a suitability for the batch size in the history-based batch method, it is still problem dependent and requires repeated trial and error to get sufficient size of batches. In case of the  $k$ -eigenvalue calculations, it is recommended to be more than 10,000 or even 100,000 number of neutrons to guarantee a normal distribution. In addition, it should be noted that a sufficient number of samples is required to get a reliable probability density of  $p$ -value in the normality test, which is known to be greater than 100. In the history-based batch method, the batch size and the number of batches are interrelated because the number of batches is determined by dividing the total number of neutrons by the batch size. Therefore, when determining the batch size, both batch size and number of batches should be considered in terms of the guarantee of a normal distribution and the applicability of a normality test.

Table 4.2 Results of the normality test in C5G7-TD0-5 problem

Batch size	Number of batches	Jarque-Bera $p$ -value	Lilliefors $D_n$	Lilliefors critical value $D_{n,\alpha}$
100	10000	< 0.00001	0.05956	0.01266
250	4000	< 0.00001	0.04326	0.02001
500	2000	0.00672	0.03682	0.02829
1000	1000	0.10574	0.03607	0.03998
2500	400	0.43334	0.04367	0.06307
5000	200	0.52427	0.05873	0.08885
10000	100	0.56349	0.07878	0.12468

#### 4.4. Error Propagation in TDMC Method

From the results of the infinite homogeneous two-group problems in the previous section, it is observed that the RSD of a tally mean continues to increase with the time step. To investigate the aspect of the error propagation in the TDMC simulation, the error at each time step is quantified based on the uncertainty propagation model and compared with the calculation results.

In TDMC simulation, the population control is forced to continue the simulation especially, when the system is far from the critical state. For an efficiency of the simulation, the number of neutrons to be simulated is maintained constant by adjusting the weight of neutrons while conserving the total weight. The weight of neutrons after the population control is determined by the number of survival neutrons or the weight sum of survival neutrons. The ratio of the neutron weights at the end of a time step is accumulated step by step, and this accumulated neutron weight acts as a multiplier for the tally estimates. Then by separating the multiplier, the mean of tally estimates in the  $i$ -th time step can be written as [34]

$$\bar{Q}_i = F_i \frac{1}{N} \sum_{j=1}^N q_{ij}, \quad (4.16)$$

$$F_i = \prod_{i'=1}^{i-1} f_{i'} = \prod_{i'=1}^{i-1} \left( \frac{\sum_{j=1}^N w_{ij}^s}{N \times \bar{w}_{i'}} \right). \quad (4.17)$$

where  $i$  and  $j$  are the time step and history index.  $q_{ij}$  is a tally estimate from the  $j$ -th neutron with a weight 1.0 in the  $i$ -th time step.  $F_i$  is the multiplier of the  $i$ -th time step which is expressed as the product of the neutron weight ratio,  $f_i$ , of the

preceding time steps.  $f_i$  is defined as the ratio of the sum of neutrons weights at the beginning of  $i$ -th time step and the sum of weights of survival neutrons at the end of the  $i$ -th time step. Then the uncertainties of the neutron weight ratios at each time step are propagated through the multiplier and affect the uncertainty of a tally. Since the multiplier does not affect the simulation, the relative error of a tally mean can be expressed as

$$\frac{\sigma^2[\bar{Q}_i]}{\bar{Q}_i^2} \cong \frac{\sigma^2[F_i]}{F_i^2} + \frac{\sigma^2[\bar{q}_i]}{\bar{q}_i^2}, \quad (4.18)$$

$$\bar{q}_i = \frac{1}{N} \sum_{j=1}^N q_{ij}. \quad (4.19)$$

The second term in the right-hand side of the equation (4.18) is a stochastic uncertainty of the simulation, so it can be expected that the first term will dominate the uncertainty of the tally as time step proceeds. Using the first-order Taylor series expansion, the variance of the multiplier can be written as

$$dF_i = \sum_{i'=1}^{i-1} \left( \frac{\partial F_i}{\partial f_{i'}} \right) df_{i'}, \quad (4.16)$$

$$\begin{aligned} \frac{\sigma^2[F_i]}{F_i^2} &= \frac{E[(dF_i)^2]}{F_i^2} \\ &= \frac{1}{F_i^2} \sum_{m=1}^{i-1} \sum_{m'=1}^{i-1} \left( \frac{\partial F_i}{\partial f_m} \right) \left( \frac{\partial F_i}{\partial f_{m'}} \right) \text{cov}[f_m, f_{m'}] = \sum_{m=1}^{i-1} \sum_{m'=1}^{i-1} \frac{\text{cov}[f_m, f_{m'}]}{f_m \cdot f_{m'}}. \end{aligned} \quad (4.17)$$

This error propagation formula does not exactly represent the error behavior of a tally mean in the history-based batch method or the replica calculations because the



formula represents the variance of the products of the means while the error observed in the simulation is the variance of the mean of the products. However, the comparison of both results can help estimate the cause of the error propagation.

Figure 4.20 is the trend of RSDs along the time step in the previous supercritical case of infinite homogeneous two-group problems. The reference RSDs are estimated from the tally results of the replica calculations and the RSDs of error propagation is calculated with the weight ratios of the replica calculations using formula (4.17). It shows a similar level of uncertainties in the weight ratios over the time steps and its propagation presents similar error trend with the reference. The RSDs are expected to increase continuously as the uncertainties accumulate over the time steps.

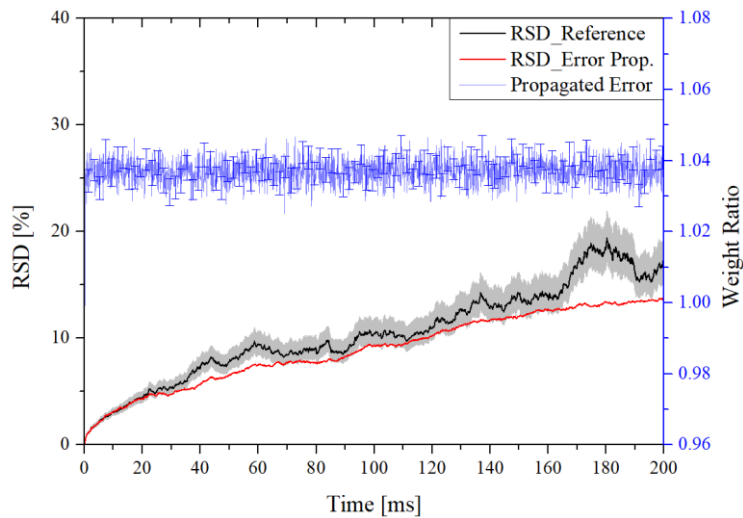


Figure 4.20 Trend of RSDs in 0D 2G supercritical system without delayed neutrons

In case of the C5G7-TD problem where the delayed neutrons are simulated, somewhat different trend of errors is observed. Figure 4.21 is the trend of RSDs in TD0-5 problem. Almost constant RSDs and the slightly increasing RSDs are

appeared in the reference and the error propagation cases respectively. This seems to be attributed to the dominant delayed neutrons in the subcritical system because the multiplier is applied to the survival neutrons only while the delayed neutron is newly added in each time step with its own weight calculated from the decay probability. In other words, the large contributions from the delayed neutrons prevent large fluctuations of the tally estimates and in turn, it keeps errors from propagating largely. On the other hand, in a supercritical system where the delayed neutrons are not dominant, the error is expected to be propagated along the time step as in the previous cases where delayed neutrons are not simulated. This can be found in Figure 4.22 which is the case of a supercritical system with delayed neutrons made by modifying the TD0-4 problem. To demonstrate the effect of the delayed neutrons in TDMC error propagation, the contributions from the survival neutrons and delayed neutrons are quantified respectively. Figures 4.23 and 4.24 are the comparison results of the reaction rate contributions from the survival neutrons and delayed neutrons in the TD0-5 subcritical problem and modified TD0-4 supercritical problem. In both figures, the solid lines and dashed lines indicate the reaction rate contributions and the ratio of the contributions respectively. In the subcritical case where the delayed neutron contribution is relatively high at about 20% of the total reaction rate, the error does not propagate far because the contribution of the survival neutrons in the time step disappeared quickly and the error behavior is dominated by the delayed neutrons. On the other hand, in the supercritical case where the delayed neutron contribution is very low less than 0.1%, the error is propagated through the long lived survival neutrons over large number of time steps as expected in the error propagation model. It is emphasized here that the main factor determining the tendency of error propagation is not the criticality of a system, but the proportion of

survival neutrons propagating the error over time steps. Therefore, even if a transient occurs in a system with the same criticality, it can be expected that the propagation of the error is relatively slow when the delayed neutron fraction is high.

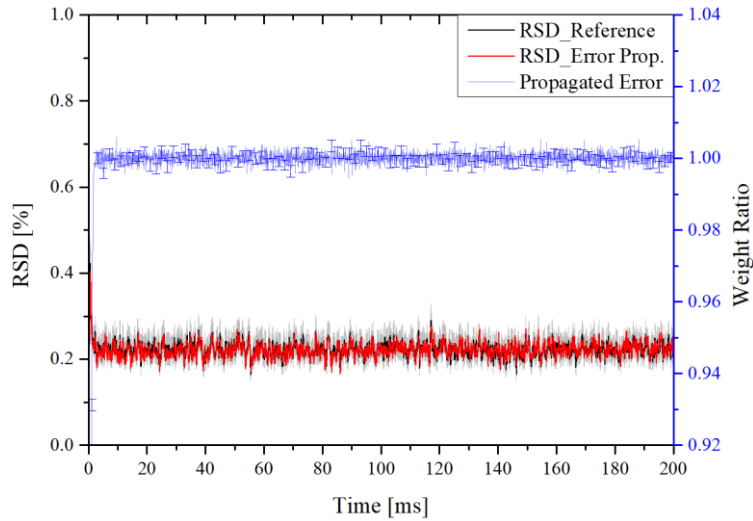


Figure 4.21 Trend of RSDs in TD0-5 subcritical problem

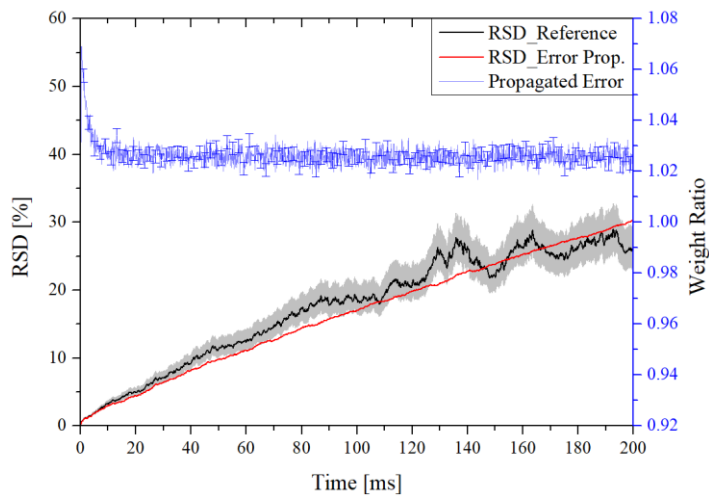


Figure 4.22 Trend of RSDs in modified TD0-4 supercritical problem

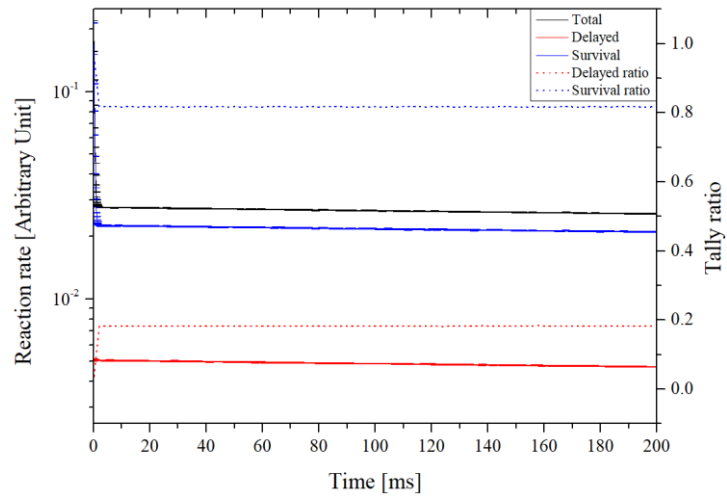


Figure 4.23 Reaction rate contributions in TD0-5 subcritical problem

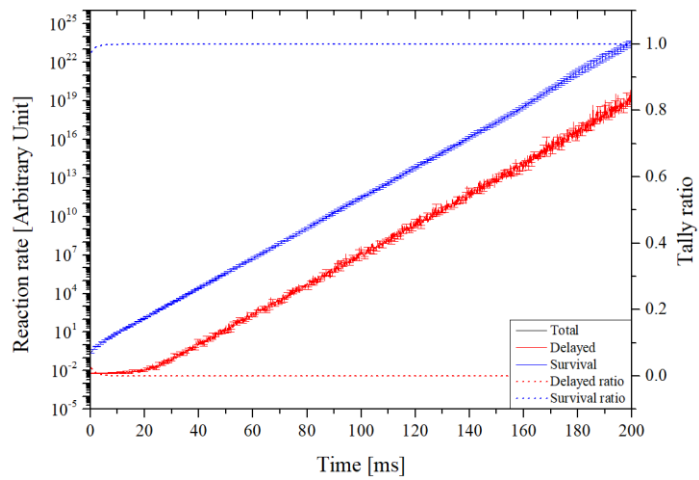


Figure 4.24 Reaction rate contributions in modified TD0-4 supercritical problem

## Chapter 5. Time-dependent Kinetics Parameter

### Estimation in TDMC Simulation

#### 5.1. Kinetics Parameter Estimation

##### 5.1.1. Exact Point Kinetics Equations

The estimation of kinetics parameters is essential for establishing the point kinetics model in reactor transient analysis. In the exact form of the point kinetics equation (PKE) [35], the kinetics parameters which are defined as a ratio of integrals of the time-dependent Boltzmann transport equation and precursor density equations over space, energy, and angle are time-dependent.

$$\frac{1}{v} \frac{\partial \Phi}{\partial t} = -\mathbf{M}\Phi + \mathbf{F}_p \Phi + \sum_i \lambda_i c_i + s_{ext}, \quad (5.1)$$

$$\frac{\partial c_i}{\partial t} = \mathbf{F}_{di} \Phi - \lambda_i c_i, \quad (5.2)$$

$$\begin{aligned} \mathbf{M}\Phi = & [\boldsymbol{\Omega} \cdot \nabla + \Sigma_t(\mathbf{r}, E, t)] \Phi(\mathbf{r}, E, \boldsymbol{\Omega}, t) \\ & - \int dE' \int d\boldsymbol{\Omega}' \Sigma_s(E', \boldsymbol{\Omega}' \rightarrow E, \boldsymbol{\Omega} | \mathbf{r}, t) \Phi(\mathbf{r}, E', \boldsymbol{\Omega}', t), \end{aligned} \quad (5.3)$$

$$\mathbf{F}_p \Phi = \frac{\chi_p(\mathbf{r}, E, t)}{4\pi} \int dE' \int d\boldsymbol{\Omega}' \nu_p(\mathbf{r}, E', t) \Sigma_f(\mathbf{r}, E', t) \Phi(\mathbf{r}, E', \boldsymbol{\Omega}', t), \quad (5.4)$$

$$\mathbf{F}_{di} \Phi = \frac{\chi_{di}(\mathbf{r}, E, t)}{4\pi} \int dE' \int d\boldsymbol{\Omega}' \nu_{di}(\mathbf{r}, E', t) \Sigma_f(\mathbf{r}, E', t) \Phi(\mathbf{r}, E', \boldsymbol{\Omega}', t), \quad (5.5)$$

$$c_i(\mathbf{r}, E, \boldsymbol{\Omega}, t) = \frac{\chi_{di}(r, E, t)}{4\pi} C_i(\mathbf{r}, t). \quad (5.6)$$

In the above equations, notations follow the conventions. By introducing the fission production operator  $\mathbf{F}\Phi \equiv \left( \mathbf{F}_p + \sum_i \mathbf{F}_{di} \right) \Phi$ , multiplying an arbitrary weight function  $w$ , and integrating it over  $(\mathbf{r}, E, \boldsymbol{\Omega})$ , the equation (5.1) becomes

$$\left\langle w, \frac{1}{v} \frac{\partial \Phi}{\partial t} \right\rangle = -\langle w, \mathbf{M}\Phi \rangle + \langle w, \mathbf{F}\Phi \rangle - \left\langle w, \sum_i \mathbf{F}_{di} \Phi \right\rangle + \left\langle w, \sum_i \lambda_i C_i \right\rangle + \langle w, S_{ext} \rangle. \quad (5.7)$$

With the separation of the angular flux into an amplitude function  $P$  and a shape function  $\psi$  and the normalization condition of

$$\Phi(\mathbf{r}, E, \boldsymbol{\Omega}, t) = P(t) \cdot \psi(\mathbf{r}, E, \boldsymbol{\Omega}, t), \quad (5.8)$$

$$\frac{\partial}{\partial t} \left\langle w, \frac{\psi}{v} \right\rangle = 0, \quad (5.9)$$

the exact PKE can be derived as

$$\frac{dP(t)}{dt} = \frac{\rho(t) - \beta(t)}{\Lambda(t)} P(t) + \sum_i \lambda_i C_i(t) + S_{ext}(t), \quad (5.10)$$

$$\frac{dC_i(t)}{dt} = \frac{\beta_i(t)}{\Lambda(t)} P(t) - \lambda_i C_i(t). \quad (5.11)$$

In the above equations, the kinetics parameters are defined as

$$\beta(t) \equiv \sum_i \beta_i(t) = \sum_i \frac{\langle w, \mathbf{F}_{di} \psi \rangle}{\langle w, \mathbf{F} \psi \rangle}, \quad (5.12)$$

$$\Lambda(t) \equiv \frac{\left\langle w, \frac{\psi}{v} \right\rangle}{\left\langle w, \mathbf{F} \psi \right\rangle}. \quad (5.13)$$

The kinetics parameters in the exact PKE contain the time-dependent operators and shape function. In practice, however, due to the difficulties of getting the exact shape function, equations are approximated by the fundamental mode solution of the steady-state transport equation for the shape function, and its corresponding adjoint function for the weight function. Generally, the  $k$ -eigenvalue equation is used for the initially critical state and  $k$ -eigenvalue equation,  $\alpha$ -eigenvalue equation or inhomogeneous equation with external source is used for the initially subcritical state.

With the development of advanced methods for the TDMC simulation, the exact shape function or the time-dependent behavior of neutrons can be obtained. In addition, efficient MC algorithms [36] for estimating the adjoint response of an arbitrary detector cross section during the MC fixed source calculation are developed, which are applicable to the TDMC simulation as well. Thus, based on these, the time-dependent kinetics parameters estimation method reflecting the exact time-dependent shape function and the adjoint response is developed and presented in this chapter.

### 5.1.2. Physical Meaning of Adjoint Response

The physical meaning the adjoint response and its MC algorithm can be derived starting from the adjoint equation of the outcoming collision density equation written as

$$\Phi_{\text{det}}^{\dagger} = \hat{\Sigma}_{\text{det}} + \mathbf{K}^{\dagger} \Phi_{\text{det}}^{\dagger}, \quad (5.14)$$

$$\Sigma_{\text{det}} \equiv \int d\mathbf{r}' \tilde{T}(\mathbf{r} \rightarrow \mathbf{r}' | E, \mathbf{\Omega}, t) \frac{\Sigma_{\text{det}}(\mathbf{r}', E, t)}{\Sigma_t(\mathbf{r}', E, t)}, \quad (5.15)$$

$$\mathbf{K}^\dagger \Phi_{\text{det}}^\dagger = \int d\mathbf{r}' \int dE' \int d\mathbf{\Omega}' \tilde{T}(\mathbf{r} \rightarrow \mathbf{r}' | E, \mathbf{\Omega}, t) C(E, \mathbf{\Omega} \rightarrow E', \mathbf{\Omega}' | \mathbf{r}', t) \Phi_{\text{det}}^\dagger(\mathbf{r}', E', \mathbf{\Omega}', t) \quad (5.16)$$

where the  $\mathbf{K}^\dagger$  and  $\Sigma_{\text{det}}$  are the adjoint transport kernel and the detector response with an arbitrary detector cross section  $\Sigma_{\text{det}}$  defined with the kernels below.

$$C(E, \mathbf{\Omega} \rightarrow E', \mathbf{\Omega}' | \mathbf{r}', t') = \frac{\Sigma_s(E, \mathbf{\Omega} \rightarrow E', \mathbf{\Omega}' | \mathbf{r}', t')}{\Sigma_t(\mathbf{r}', E, t')} + \frac{\nu(\mathbf{r}', E, t') \Sigma_f(\mathbf{r}', E, t')}{\Sigma_t(\mathbf{r}', E, t')} \cdot \frac{\chi(\mathbf{r}', E', t')}{4\pi} \quad (5.17)$$

$$T(\mathbf{r} \rightarrow \mathbf{r}' | E, \mathbf{\Omega}, t') = \frac{\Sigma_t(\mathbf{r}', E, t')}{|\mathbf{r}' - \mathbf{r}|^2} \exp \left[ - \int_0^{|\mathbf{r}' - \mathbf{r}|} \Sigma_t \left( \mathbf{r}' - s \frac{\mathbf{r}' - \mathbf{r}}{|\mathbf{r}' - \mathbf{r}|}, E, t' - \frac{s}{v} \right) ds \right] \delta \left( \mathbf{\Omega} \cdot \frac{\mathbf{r}' - \mathbf{r}}{|\mathbf{r}' - \mathbf{r}|} - 1 \right) \quad (5.18)$$

$$\tilde{T}(\mathbf{r} \rightarrow \mathbf{r}' | E, \mathbf{\Omega}, t) \equiv \frac{\Sigma_t(\mathbf{r}', E, t)}{|\mathbf{r}' - \mathbf{r}|^2} \exp \left[ - \int_0^{|\mathbf{r}' - \mathbf{r}|} \Sigma_t \left( \mathbf{r}' - s \frac{\mathbf{r}' - \mathbf{r}}{|\mathbf{r}' - \mathbf{r}|}, E, t \right) ds \right] \delta \left( \mathbf{\Omega} \cdot \frac{\mathbf{r}' - \mathbf{r}}{|\mathbf{r}' - \mathbf{r}|} - 1 \right) \quad (5.19)$$

In the above equations,  $T$  and  $C$  represent the free flight kernel and the collision kernel. In the conventional kernels, the time variable is omitted because the change of the location  $\mathbf{r}$  implies the change in time. In here, the time variable is added to express the change of cross sections in TDMC simulation. The kernel  $\tilde{T}$  is redefined and used in the adjoint transport kernel instead of  $T$  since the expected importance or the adjoint response of a neutron is defined in the fixed phase space  $(\mathbf{r}, E, \mathbf{\Omega}, t)$  when the neutron is introduced. So one can find that the time is fixed in



the flight kernel  $\tilde{T}$ . The time variables in macroscopic cross sections are included in the number density terms expressed as

$$\Sigma_r(\mathbf{r}, E, t) = \sum_l N^l(\mathbf{r}, t) \sigma_r^l(\mathbf{r}, E), \quad (5.20)$$

$$\Sigma_s(E', \boldsymbol{\Omega}' \rightarrow E, \boldsymbol{\Omega} | \mathbf{r}, t) = \sum_l N^l(\mathbf{r}, t) \sigma_s^l(E', \boldsymbol{\Omega}' \rightarrow E, \boldsymbol{\Omega} | \mathbf{r}), \quad (5.21)$$

$$\nu(\mathbf{r}, E, t) = \frac{\sum_l \nu^l(\mathbf{r}, E) N^l(\mathbf{r}, t) \sigma_f^l(\mathbf{r}, E)}{\sum_l N^l(\mathbf{r}, t) \sigma_f^l(\mathbf{r}, E)}, \quad (5.22)$$

$$\begin{aligned} \chi(\mathbf{r}, E, t) \\ = \frac{\sum_l \chi^l(\mathbf{r}, E) \int dE' \int d\boldsymbol{\Omega}' \nu^l(\mathbf{r}, E') N^l(\mathbf{r}, t) \sigma_f^l(\mathbf{r}, E') \Phi(\mathbf{r}, E', \boldsymbol{\Omega}', t)}{\sum_l \int dE' \int d\boldsymbol{\Omega}' \nu^l(\mathbf{r}, E') N^l(\mathbf{r}, t) \sigma_f^l(\mathbf{r}, E') \Phi(\mathbf{r}, E', \boldsymbol{\Omega}', t)}, \end{aligned} \quad (5.23)$$

where subscript  $r$  and  $l$  denote the reaction type and the isotope index. From equation (5.14), the adjoint response can be expressed as below with the Taylor's series expansion.

$$\Phi_{\text{det}}^\dagger = (1 - \mathbf{K}^\dagger)^{-1} \hat{\Sigma}_{\text{det}} = \left[ 1 + \mathbf{K}^\dagger + (\mathbf{K}^\dagger)^2 + \dots \right] \hat{\Sigma}_{\text{det}} = \sum_{j=0}^{\infty} \Phi_{\text{det}, j}^\dagger \quad (5.24)$$

$$\begin{aligned} \Phi_{\text{det}, j}^\dagger &= (\mathbf{K}^\dagger)^j \hat{\Sigma}_{\text{det}} \\ &= \int d\mathbf{r}' \int d\mathbf{r}_j \int dE_j \int d\boldsymbol{\Omega}_j \frac{\Sigma_{\text{det}}(\mathbf{r}', E_j, t)}{\Sigma_i(\mathbf{r}', E_j, t)} \tilde{T}(\mathbf{r}_j \rightarrow \mathbf{r}' | E_j, \boldsymbol{\Omega}_j, t) \\ &\quad \cdot \int d\mathbf{r}_{j-1} \int dE_{j-1} \int d\boldsymbol{\Omega}_{j-1} C(E_{j-1}, \boldsymbol{\Omega}_{j-1} \rightarrow E_j, \boldsymbol{\Omega}_j | \mathbf{r}_j, t) \tilde{T}(\mathbf{r}_{j-1} \rightarrow \mathbf{r}_j | E_{j-1}, \boldsymbol{\Omega}_{j-1}, t) \\ &\quad \dots \int d\mathbf{r}_1 \int dE_1 \int d\boldsymbol{\Omega}_1 C(E_1, \boldsymbol{\Omega}_1 \rightarrow E_2, \boldsymbol{\Omega}_2 | \mathbf{r}_2, t) \tilde{T}(\mathbf{r}_1 \rightarrow \mathbf{r}_2 | E_1, \boldsymbol{\Omega}_1, t) \\ &\quad \cdot C(E, \boldsymbol{\Omega} \rightarrow E_1, \boldsymbol{\Omega}_1 | \mathbf{r}_1, t) \tilde{T}(\mathbf{r} \rightarrow \mathbf{r}_1 | E, \boldsymbol{\Omega}, t) \end{aligned} \quad (5.25)$$

$\Phi_{\text{det}, j}^\dagger$  is the adjoint response from the  $j$ -th collision. From the equations (5.24) and

(5.25), the adjoint response,  $\Phi_{\text{det}}^\dagger(\mathbf{r}, E, \mathbf{\Omega}, t)$ , can be interpreted as the sum of expected detector signals induced by a neutron at phase space  $(\mathbf{r}, E, \mathbf{\Omega}, t)$ .

### 5.1.3. MC Algorithm for Kinetics Parameter Estimation

From the exact forms of PKE, the adjoint weighted kinetics parameters,  $\beta(t)$  and  $\Lambda(t)$ , are expressed as

$$\beta(t) \equiv \sum_i \beta_i(t) = \sum_i \frac{\langle \Phi_{\text{det}}^\dagger, \mathbf{F}_{di} \psi \rangle}{\langle \Phi_{\text{det}}^\dagger, \mathbf{F} \psi \rangle}, \quad (5.26)$$

$$\Lambda(t) \equiv \frac{\langle \Phi_{\text{det}}^\dagger, \frac{\psi}{v} \rangle}{\langle \Phi_{\text{det}}^\dagger, \mathbf{F} \psi \rangle}, \quad (5.27)$$

where  $\psi$  is the time-dependent shape function and the bracket  $\langle \rangle$  means the inner product of the components over  $(\mathbf{r}, E, \mathbf{\Omega})$ . The Neumann series solution of the collision density equation gives the fission operator term in the bracket as

$$\begin{aligned} \langle \mathbf{F} \psi \rangle = & \sum_{j=0}^{\infty} \int d\mathbf{r} \int dE \int d\mathbf{\Omega} \int d\mathbf{r}_j \frac{\nu(\mathbf{r}, E, t) \Sigma_f(\mathbf{r}, E, t)}{\Sigma_t(\mathbf{r}, E, t)} T(\mathbf{r}_j \rightarrow \mathbf{r} | E, \mathbf{\Omega}, t) \\ & \cdot \int d\mathbf{r}_{j-1} \int dE_{j-1} \int d\mathbf{\Omega}_{j-1} C(E_{j-1}, \mathbf{\Omega}_{j-1} \rightarrow E_j, \mathbf{\Omega}_j | \mathbf{r}_j, t_j) T(\mathbf{r}_{j-1} \rightarrow \mathbf{r}_j | E_{j-1}, \mathbf{\Omega}_{j-1}, t_j), \quad (5.28) \\ & \cdots \int d\mathbf{r}_1 \int dE_1 \int d\mathbf{\Omega}_1 C(E_1, \mathbf{\Omega}_1 \rightarrow E_2, \mathbf{\Omega}_2 | \mathbf{r}_2, t_2) T(\mathbf{r}_1 \rightarrow \mathbf{r}_2 | E_1, \mathbf{\Omega}_1, t_2) \\ & \cdot C(E', \mathbf{\Omega}' \rightarrow E_1, \mathbf{\Omega}_1 | \mathbf{r}_1, t_1) T(\mathbf{r}' \rightarrow \mathbf{r}_1 | E', \mathbf{\Omega}', t_1) s_t(\mathbf{r}', E', \mathbf{\Omega}', t') \end{aligned}$$

where  $s_t$  denotes the time source density in the TDMC simulation which consists of the survival neutron source from the previous time step and the delayed neutron source. Equation (5.28) means all fission neutrons generated during the flight and

collision of a neutron starting from the time source. By combining the Neumann series solutions of the collision density equation with that of the adjoint response, equation (5.24), the time-dependent kinetics parameters can be calculated. Then the denominator of the kinetics parameters indicates the sum of all expected detector responses induced by the generated fission neutrons starting from the time source.

Without any approximations, this can be exactly done by producing artificial branches at each fission event and simulating them to obtain the adjoint response tally. However, this so-called Contribution method [18] is quite burdensome which may take hundreds of times depending on the system, especially if applied to a near critical or a supercritical problem. So more efficient MC algorithms are developed utilizing Shim's MC algorithm [36] with some assumptions to apply it for the TDMC simulation.

The idea of the efficient MC algorithm is to utilize the subsequent branches of the neutron instead of making artificial branches for the adjoint calculation. Figure 5.1 shows the schematic of the algorithm for calculating the fission operator term  $\langle \Phi_{\text{det}}^{\dagger}, \mathbf{F} \psi \rangle$ . The figure is a branch process of a neutron where the yellow circles denote fission reactions and the thick lines after the fissions indicates the generation of a delayed neutron. In the Contribution method, artificial branches are generated when a fission occurs and their contributions are calculated along the individual tracks. However, the same contributions can be obtained by following the original track as if it is an artificial branch. The number in each collision point is the number of overlapping contributions when each fission neutron makes contributions along the original tracks. This number is equal to the number of fissions a neutron experienced before the collision point. Therefore, one can estimate all of the

contributions in a forward calculation by counting the fission events and tallying the detector responses multiplied by this number. Other two terms of  $\langle \Phi_{\text{det}}^{\dagger}, \mathbf{F}_{di} \psi \rangle$  and  $\langle \Phi_{\text{det}}^{\dagger}, \frac{\psi}{v} \rangle$  in kinetics parameters can be calculated in the same way.  $\langle \Phi_{\text{det}}^{\dagger}, \mathbf{F}_{di} \psi \rangle$  means the integration of detector responses after a delayed fission occurs, so it can be calculated by counting the delayed fission events instead of the fission events.  $\langle \Phi_{\text{det}}^{\dagger}, \frac{\psi}{v} \rangle$  means the integration of detector responses after each collision weighted by the flight time. This is because  $\psi / v$  term indicates the track length divided by the velocity between each collision, so one can estimate the integral term by accumulating the flight time instead of the fission events.

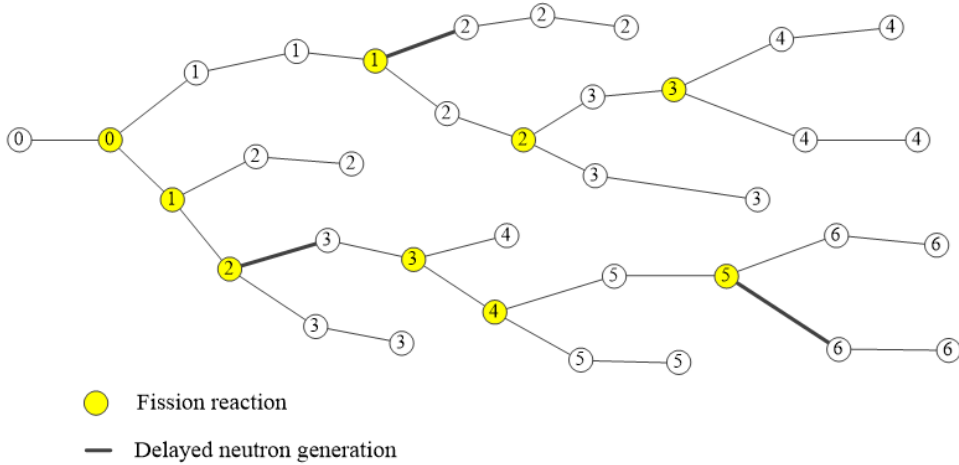


Figure 5.1 Tally algorithm for the estimation of kinetics parameters  
in fixed source mode calculation

However, this algorithm cannot be applied to the TDMC simulation as it is for several reasons. First, the shape function within a time step is represented by the simulation of neutrons starting from the time source until the upper time boundary.

Thus, the adjoint responses should be weighted to the collisions within a time step. Second, the calculation of the adjoint responses may not be finished in the case when the system is near critical or supercritical. To prevent such an endless simulation, the adjoint convergence interval ( $L$ ) is introduced and the adjoint response is calculated within the  $L$  considering the starting time of adjoint calculation. Finally, since the system within a time step keeps changing, for the exact calculation, it is necessary to estimate the adjoint responses by fixing the system time at each starting time of the adjoint calculation. But there is no way to do this without making artificial branches. Therefore, it is assumed that the system change and its effect on the adjoint response are small enough within a time step that the kinetics parameters calculation can be conducted at the fixed beginning of a time step. This assumption is thought to be valid because the time interval of the TDMC simulation is very small with an order of the neutron generation time. Considering the characteristics of the TDMC simulation listed above, the MC algorithm for the kinetics parameter estimation is modified.

Figure 5.2 is the schematic of the modified algorithm to fit it in the TDMC simulation. The time interval of the TDMC simulation,  $\Delta t$ , and the adjoint convergence interval,  $L$ , are introduced, and the number of repeated contributions in the collision points are changed accordingly. Then one can estimate the integral term with fission operator by counting the number of fission events occurred within  $L$  before the collision and within  $\Delta t$ .

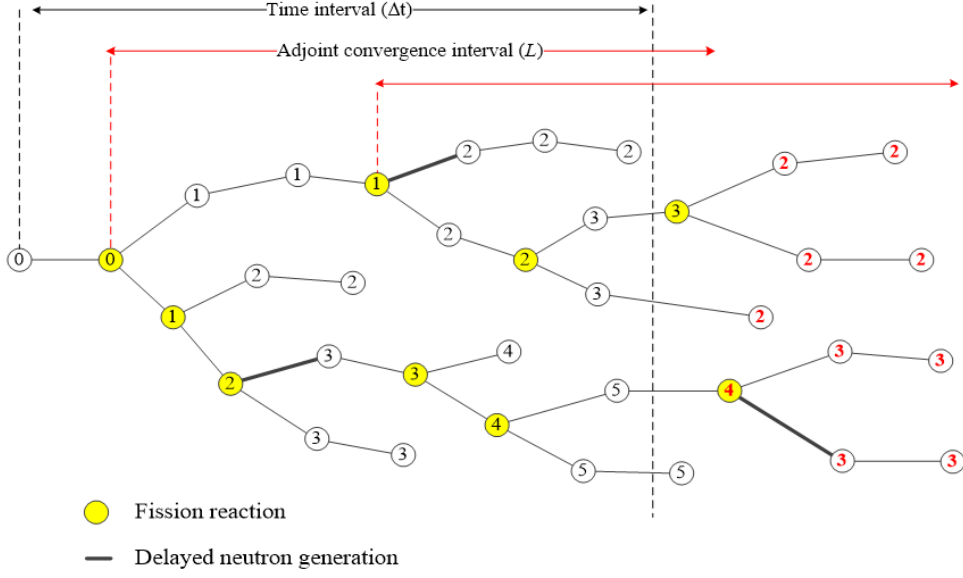


Figure 5.2 Modified tally algorithm for the estimation of kinetics parameters  
in TDMC simulation

The MC algorithms for the estimation of the terms in the equations (5.26) and (5.27) can be expressed as

$$\begin{aligned}
 \langle \Phi_{\text{det}}^\dagger, \mathbf{F} \psi \rangle &\cong \frac{1}{N} \sum_{n=1}^N \sum_{n'} \sum_{j \in D_j^{(n,n')}} J^{(n,n')} w_{j+1}^{(n,n')} \left( \frac{1}{w_{j+1}^{(n,n')}} \sum_{\substack{j'=j+1 \\ j' \notin \{D_c^{(n,n'')} | n'' < n'\}}}^{J_L^{(n,n')} j} \left( w_{j'}^{(n,n')} \frac{\Sigma_{\text{det}}^{(n,n')} j'}{\Sigma_t^{(n,n')} j'} \right) \right), \quad (5.29) \\
 &= \frac{1}{N} \sum_{n=1}^N \sum_{n'} \sum_{\substack{j=1 \\ j \notin \{D_c^{(n,n'')} | n'' < n'\}}}^{J^{(n,n')} j} \left( m_{f,L}^{(n,n')} w_j^{(n,n')} \frac{\Sigma_{\text{det}}^{(n,n')} j}{\Sigma_t^{(n,n')} j} \right)
 \end{aligned}$$

$$\begin{aligned}
 \langle \Phi_{\text{det}}^\dagger, \sum_i \mathbf{F}_{di} \psi \rangle &\cong \frac{1}{N} \sum_{n=1}^N \sum_{n'} \sum_{j \in D_{di}^{(n,n')}} J^{(n,n')} w_{j+1}^{(n,n')} \left( \frac{1}{w_{j+1}^{(n,n')}} \sum_{\substack{j'=j+1 \\ j' \notin \{D_c^{(n,n'')} | n'' < n'\}}}^{J_L^{(n,n')} j} \left( w_{j'}^{(n,n')} \frac{\Sigma_{\text{det}}^{(n,n')} j'}{\Sigma_t^{(n,n')} j'} \right) \right), \quad (5.30) \\
 &= \frac{1}{N} \sum_{n=1}^N \sum_{n'} \sum_{\substack{j=1 \\ j \notin \{D_c^{(n,n'')} | n'' < n'\}}}^{J^{(n,n')} j} \left( m_{d,L}^{(n,n')} w_j^{(n,n')} \frac{\Sigma_{\text{det}}^{(n,n')} j}{\Sigma_t^{(n,n')} j} \right)
 \end{aligned}$$

$$\begin{aligned}
\left\langle \Phi_{\text{det}}^\dagger, \frac{\psi}{v} \right\rangle &\cong \frac{1}{N} \sum_{n=1}^N \sum_{n'} J(n, n') \sum_{j=1}^{J(n, n')} w_{j+1}^{(n, n')} \frac{\Delta I_j^{(n, n')}}{v_j^{(n, n')}} \left( \frac{1}{w_{j+1}^{(n, n')}} \sum_{\substack{j'=j \\ j' \notin \{D_c^{(n, n'')} \mid n'' < n'\}}}^{J_L(n, n') j} \left( w_{j'}^{(n, n')} \frac{\Sigma_{\text{det}}^{(n, n') j'}}{\Sigma_t^{(n, n') j'}} \right) \right) \\
&= \frac{1}{N} \sum_{n=1}^N \sum_{n'} \sum_{\substack{j=1 \\ j \notin \{D_c^{(n, n'')} \mid n'' < n'\}}}^{J_L(n, n') j} \left( m_{t, L}^{(n, n') j} w_j^{(n, n')} \frac{\Sigma_{\text{det}}^{(n, n') j}}{\Sigma_t^{(n, n') j}} \right)
\end{aligned} \quad (5.31)$$

In the equations,  $n$  and  $n'$  are a neutron source and its branch index of multiplicative reactions such as  $(n, f)$ ,  $(n, 2n)$ , and  $(n, 3n)$  within a time step. So,  $(n, n')$  means the  $n'$ -th branch of the  $n$ -th neutron source, and  $N$  is the total number of neutron sources.  $D_f^{(n, n')}$ ,  $D_{fd}^{(n, n')}$ , and  $D_c^{(n, n')}$  are the collection of fission, delayed fission, and collision indices respectively.  $J(n, n')$  indicates the last collision index within a time step. The adjoint convergence interval,  $L$ , is introduced to set a limit on the adjoint tracking.  $J_L(n, n') j$  indicates the last collision index within the forward interval  $L$  from the  $j$ -th collision. It should be noted that the neutron weight after the  $j$ -th collision in the first equality is offset with the neutron weight in the parentheses because the adjoint response is the sum of detector responses induced by a neutron. In addition, the collision index inside the parentheses of the first equality starts with  $j+1$  in the equations (5.29) and (5.30), while it starts with  $j$  in the equation (5.31) since the flight time outside the parentheses is the time between the  $(j-1)$ -th and the  $j$ -th collision.

The convergence of the adjoint response needs to be demonstrated to assure the use of the adjoint convergence interval  $L$ . From the physical meaning of the adjoint response, the adjoint response can be defined as the sum of fission neutrons generated by a neutron introduced at phase space  $(\mathbf{r}, E, \mathbf{\Omega}, t)$  using  $v\Sigma_f$  as an arbitrary detector cross section. Then the adjoint response can be presented with the

$k$ -eigenvalues at each time step defined as equation (3.7).

$$\Phi_{\text{det}}^{\dagger} = \sum_{i=1}^{\infty} \left( \prod_{i'=1}^i k_{i'} \right) = k_1 + k_1 k_2 + \cdots + k_1 k_2 \cdots k_i + \cdots, \quad (5.32)$$

If  $T$  and  $n$  are the time and time step index taken to reach the asymptotic flux shape from the introduction of a neutron, the  $k$ -eigenvalue after time  $T$  can be approximated to  $k_{\text{asy}}$  and the adjoint response can be written as

$$\Phi_{\text{det}}^{\dagger} = \lim_{t \rightarrow \infty} N(t) = \lim_{t \rightarrow \infty} \left[ (k_1 + k_1 k_2 + \cdots + k_1 k_2 \cdots k_n) + N_n \sum_{i=1}^{(t-T)/l} (k_{\text{asy}})^i \right], \quad (5.33)$$

$$N_n = k_1 k_2 \cdots k_n, \quad (5.34)$$

where  $l$  is the neutron life time and  $N_n$  is the expected number of fission neutrons generated until the  $n$ -th time step by a neutron introduced at phase space  $(\mathbf{r}, E, \mathbf{\Omega}, t)$ .

When the system is subcritical where  $k_{\text{asy}}$  is less than 1.0, it can be easily seen that the adjoint response converges to

$$\Phi_{\text{det}}^{\dagger} = \lim_{t \rightarrow \infty} N(t) = \sum_{i=1}^n N_i + N_n \frac{k_{\text{asy}}}{1 - k_{\text{asy}}}. \quad (5.35)$$

In cases when the system is critical or supercritical where  $k_{\text{asy}}$  is greater than or equal to 1.0, the adjoint response asymptotically diverges with the rate of  $k_{\text{asy}}$ . Since the significance of the adjoint weighing is to reflect the relative importance of a neutron and the kinetics parameters are defined as the ratio of the adjoint weighted operator terms, the validity of introducing  $L$  can be justified by the convergence of the relative adjoint distribution. Using the equation (5.33), the ratio between adjoint responses at different phase space 1 and 2 is written as



$$\frac{\Phi_{\text{det},1}^{\dagger}}{\Phi_{\text{det},2}^{\dagger}} = \frac{\Phi_{\text{det}}^{\dagger}(\mathbf{r}_1, E_1, \mathbf{\Omega}_1, t_1)}{\Phi_{\text{det}}^{\dagger}(\mathbf{r}_2, E_2, \mathbf{\Omega}_2, t_2)} = \frac{\lim_{t \rightarrow \infty} N_1(t)}{\lim_{t \rightarrow \infty} N_2(t)} = \frac{N_{n,1}}{N_{n,2}}. \quad (5.36)$$

From the equation, one can see that the ratio of the adjoint responses converges even in the critical or supercritical cases. These approaches to prove the convergence of the adjoint are proposed by Fegghi [37] in the conventional  $k$ -eigenvalue calculation and the analogy of the method is applied to the adjoint response in TDMC simulation here. From the demonstrations above, it can be considered that the introduction of the adjoint convergence interval for the adjoint calculation during TDMC simulation is sufficiently reasonable.

## 5.2. Numerical Results

### 5.2.1. Infinite Homogeneous Two-group Steady-state Problems

For the verification, kinetics parameters are estimated in infinite homogeneous two-group problems. The two-group cross sections are given in Table 5.1 varying the differential scattering cross section.  $\Sigma_{s21}$  are set to make the infinite multiplication factor from 0.6 to 1.002 and  $\nu\Sigma_{fg}$  is used as the detector cross sections. McCARD calculation is done with the different number of histories and time considering its infinite multiplication factor. The simulations are conducted using 100,000,000 histories for 1 second in the cases where the  $k_{\text{inf}}$  is 0.8 or less, 10,000,000 histories for 1 second in the cases where the  $k_{\text{inf}}$  is 1.0 or less, and 50,000 histories for 0.01 second in the supercritical case. The initial neutron source is set to the fast energy group for all problems. To investigate the convergence of

kinetics parameters according to the adjoint convergence interval, simulations are conducted varying the value  $L$ . The estimated kinetics parameters are compared with the analytic solutions. In addition, to compare the efficiency of the developed method, the FOM is compared with the Contribution method.

Table 5.1 Two-group cross section data with delayed neutron

Cross section	First group ( $g=1$ )	Second group ( $g=2$ )
$\Sigma_{tg}$	0.50000	1.30000
$\Sigma_{fg}$	0.00100	0.09000
$\nu_g$	2.40000	2.40000
$\Sigma_{sgg}$	0.48000	1.09000
$\Sigma_{sg'g}$	Variable	0.00190
$\chi_g$	1.00000	0.00000
$1/\nu_g$	$2.28626 \times 10^{-10}$	$1.29329 \times 10^{-6}$
$\beta_{ig}$	$i=1$	0.00300
	$i=2$	0.00300
$\lambda_i$	$i=1$	0.16504
	$i=2$	1.44726

Figure 5.3 to 5.5 are the comparison results of the estimated  $\Lambda$  and  $\beta_{eff}$  with its reference value in  $k_{inf}$  of 0.6, 1.0, and 1.002 cases. The  $x$ -axis presents the relative adjoint convergence interval with respect to its generation time and error bars show  $2\sigma$  values. The estimates converge to the reference value as  $L$  increases, and it requires a larger  $L$  to get converged value in 1.0 and 1.002 cases where the neutron chain is relatively longer. In the subcritical case, it converges to the reference when  $L$  is longer than 10 times of the generation time, whereas it converges when  $L$  is longer than 90 times in the critical or supercritical case. Table 5.2 is the comparison

results of kinetics parameters in various cases, and it shows a good agreement within 95% confidence intervals. Table 5.3 shows the FOM of the Contribution method and the developed method according to  $k_{\text{inf}}$ . FOM is calculated as  $\frac{1}{(RSD)^2 \times T}$ . In deep subcritical systems with  $k_{\text{inf}}$  of 0.8 or less, the developed method is 2-10 times efficient than the Contribution method, however, as the system approaches the critical state, it shows more than 1,000 times better efficiency.

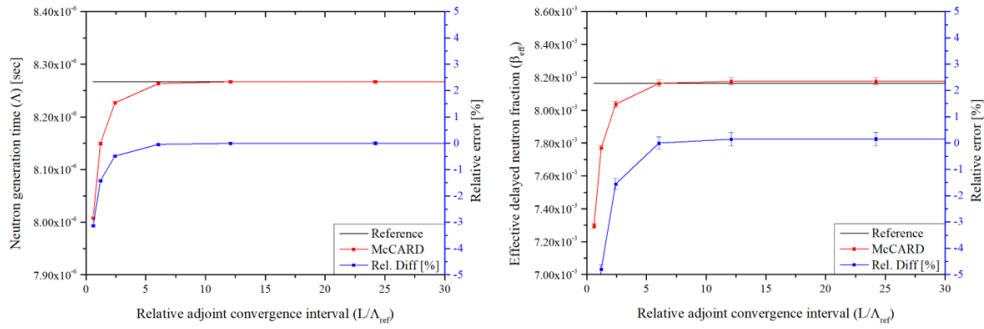


Figure 5.3 Comparison results of the estimated kinetics parameters  
in steady-state ( $k_{\text{inf}} = 0.6$ )

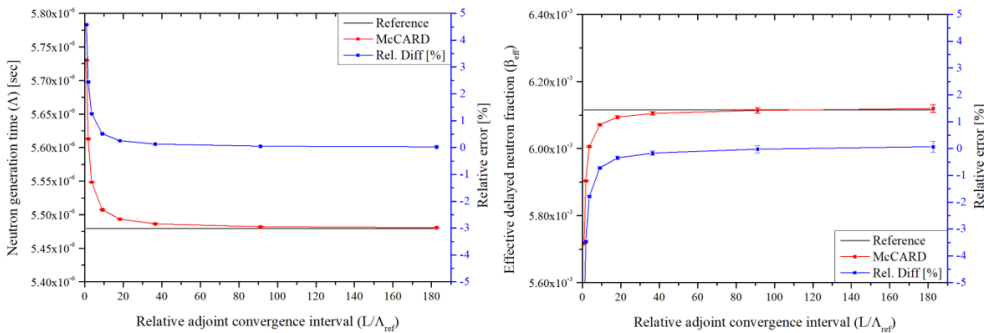


Figure 5.4 Comparison results of the estimated kinetics parameters  
in steady-state ( $k_{\text{inf}} = 1.0$ )

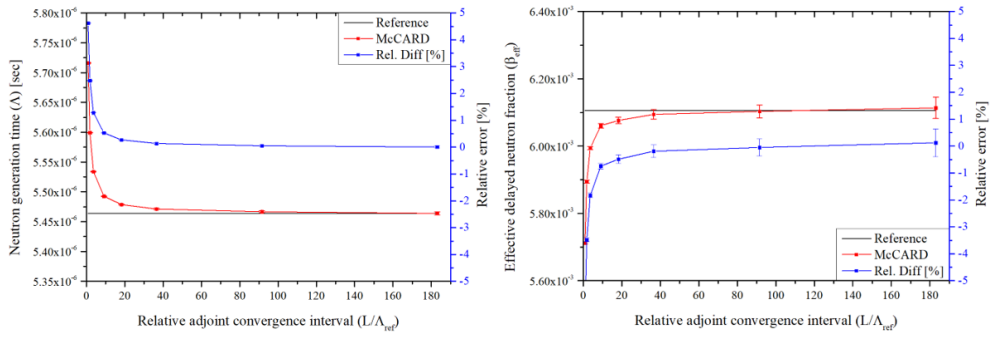


Figure 5.5 Comparison results of the estimated kinetics parameters

in steady-state ( $k_{\text{inf}} = 1.002$ )

Table 5.2 Comparison results of the estimated kinetics parameters in steady-state

$k_{\text{inf}}$	Kinetics parameter	Analytic solution	McCARD (RSD[%])	Relative error[%]
0.6	$\Lambda$	$8.26688 \times 10^{-6}$	$8.26695 \times 10^{-6}$ (0.02)	<0.01
	$\beta_{\text{eff}}$	$8.16340 \times 10^{-3}$	$8.17590 \times 10^{-3}$ (0.13)	0.15
0.7	$\Lambda$	$7.34565 \times 10^{-6}$	$7.34675 \times 10^{-6}$ (0.01)	0.01
	$\beta_{\text{eff}}$	$7.43094 \times 10^{-3}$	$7.43753 \times 10^{-3}$ (0.12)	0.09
0.8	$\Lambda$	$6.59940 \times 10^{-6}$	$6.59891 \times 10^{-6}$ (0.01)	0.01
	$\beta_{\text{eff}}$	$6.88160 \times 10^{-3}$	$6.87660 \times 10^{-3}$ (0.11)	0.07
0.9	$\Lambda$	$5.98623 \times 10^{-6}$	$5.98322 \times 10^{-6}$ (0.03)	0.05
	$\beta_{\text{eff}}$	$6.45432 \times 10^{-3}$	$6.45157 \times 10^{-3}$ (0.32)	0.04
0.98	$\Lambda$	$5.57037 \times 10^{-6}$	$5.56979 \times 10^{-6}$ (0.03)	0.01
	$\beta_{\text{eff}}$	$6.17530 \times 10^{-3}$	$6.16959 \times 10^{-3}$ (0.28)	0.09
1.0	$\Lambda$	$5.47921 \times 10^{-6}$	$5.48067 \times 10^{-6}$ (0.01)	0.03
	$\beta_{\text{eff}}$	$6.11520 \times 10^{-3}$	$6.11939 \times 10^{-3}$ (0.10)	0.07
1.002	$\Lambda$	$5.46378 \times 10^{-6}$	$5.46402 \times 10^{-6}$ (0.02)	<0.01
	$\beta_{\text{eff}}$	$6.10607 \times 10^{-3}$	$6.11369 \times 10^{-3}$ (0.26)	0.12

Table 5.3 Comparison of FOM in kinetics parameter estimation in steady-state

FOM <sub>1</sub> Contributon method			FOM <sub>2</sub> Developed method		Efficiency (FOM <sub>2</sub> /FOM <sub>1</sub> )	
$k_{\text{inf}}$	$\beta_{\text{eff}}$	$\Lambda$	$\beta_{\text{eff}}$	$\Lambda$	$\beta_{\text{eff}}$	$\Lambda$
0.6	$1.14 \times 10^2$	$1.47 \times 10^4$	$2.99 \times 10^2$	$2.47 \times 10^4$	3	2
0.7	$7.43 \times 10^1$	$8.21 \times 10^3$	$4.31 \times 10^2$	$4.02 \times 10^4$	6	5
0.8	$3.75 \times 10^1$	$7.51 \times 10^3$	$3.64 \times 10^2$	$3.98 \times 10^4$	10	5
0.9	$1.11 \times 10^1$	$1.15 \times 10^3$	$6.34 \times 10^2$	$5.74 \times 10^4$	57	50
0.98	$6.43 \times 10^{-1}$	$6.59 \times 10^1$	$7.22 \times 10^2$	$7.34 \times 10^4$	1124	1114
0.99	$1.24 \times 10^{-1}$	$5.14 \times 10^0$	$2.58 \times 10^2$	$3.06 \times 10^4$	2080	5956

### 5.2.2. Infinite Homogeneous Two-group Transient Problems

For the transient problem, a simple transient scenario is postulated by mixing the two material used in the steady-state problems. The two materials with  $k_{\text{inf}}$  of 1.0 (A) and 0.6 (B) are selected and mixed linearly from pure A material to pure B material until 5 ms. For the next 5 ms, the mixture is changed vice versa. Figure 5.6 shows the transient scenario of material mixing. McCARD TDMC calculation is done with 1,000,000 histories and the initial neutron source is set to fast energy group given at  $t=0$ . The kinetics parameters are estimated at each time step varying the time interval,  $\Delta t$ , and  $L$  and compared with the reference solution. The reference solution is calculated by the MATLAB/Simulink simulation.

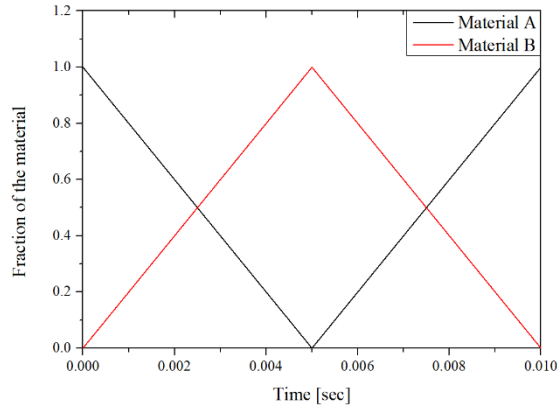


Figure 5.6 Transient scenario of material mixing in 0D 2G problem

Figures 5.7 to 5.10 are comparison results of the estimated kinetics parameters along the transient scenario. In Figures 5.7 and 5.8,  $\Delta t$  is fixed to 0.1ms, and in Figures 5.9 and 5.10,  $L$  is fixed to 1 ms. The results show a significant difference when it does not reflect sufficiently large  $L$ , which is more than 20 times of  $\Lambda$ , on the adjoint calculation. But, as for the time interval, it shows good agreement with the reference regardless of the size of  $\Delta t$ . The FOM is also evaluated to compare the efficiency of the kinetics parameters estimation methods. Comparing the RSDs at each time step, the developed method is 800 times and 1,120 times more efficient than the Contributon method in calculating  $\beta_{\text{eff}}$  and  $\Lambda$ , respectively. From the results above, the developed MC algorithm is verified to give a true solution regardless of the criticality of a system, if the adjoint convergence interval is sufficient. In addition, it works well in both steady-state problems and transient problems and shows much better computational efficiency than the Contributon method.

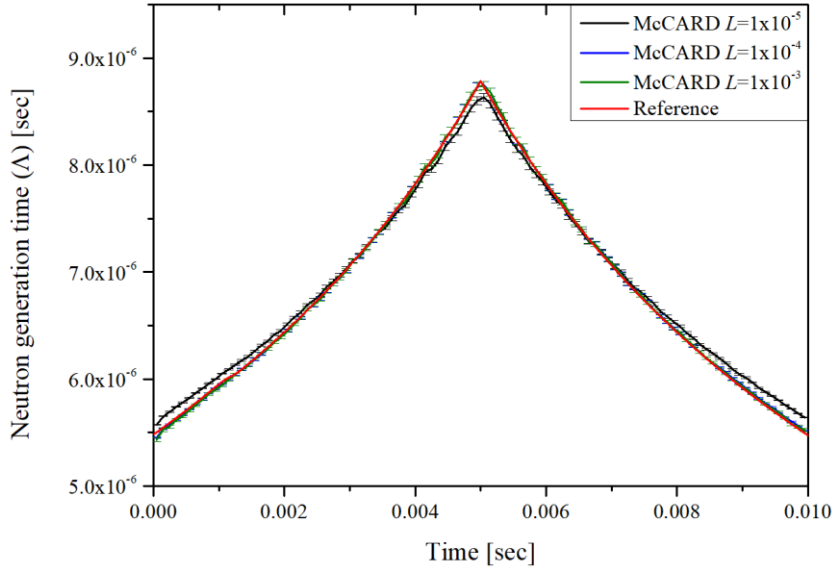


Figure 5.7 Comparison results of  $\Lambda$  regarding  $L$  ( $\Delta t=1 \times 10^{-4}$  sec)

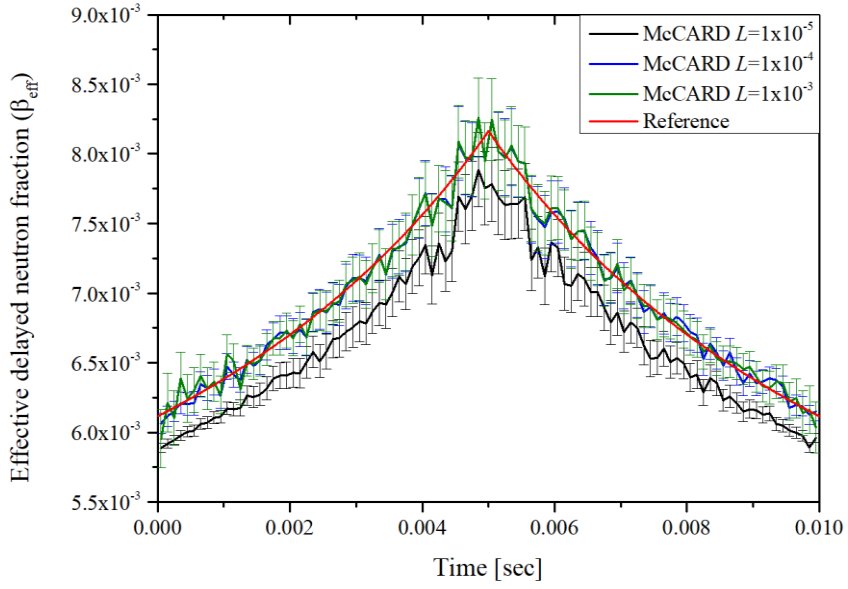


Figure 5.8 Comparison results of  $\beta_{\text{eff}}$  regarding  $L$  ( $\Delta t=1 \times 10^{-4}$  sec)

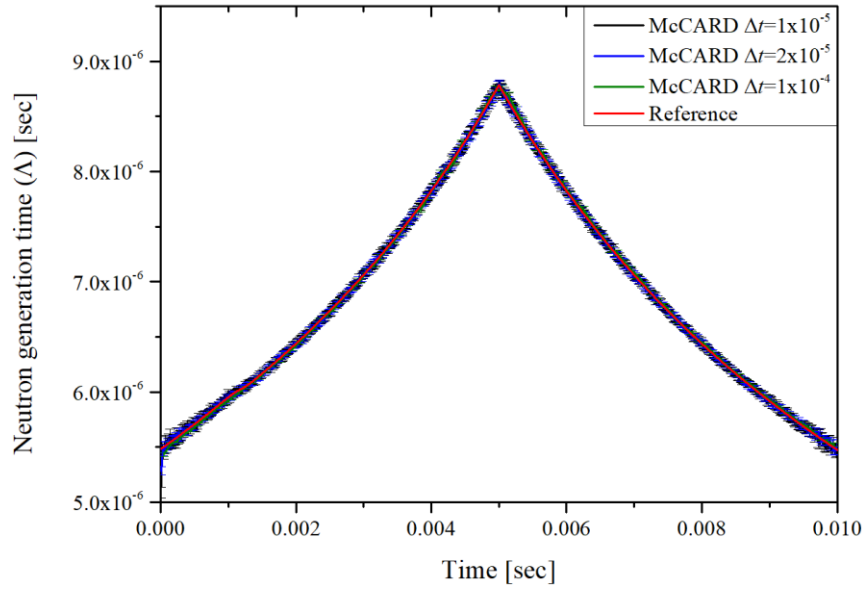


Figure 5.9 Comparison results of  $\Lambda$  regarding  $\Delta t$  ( $L = 1 \times 10^{-3}$  sec)

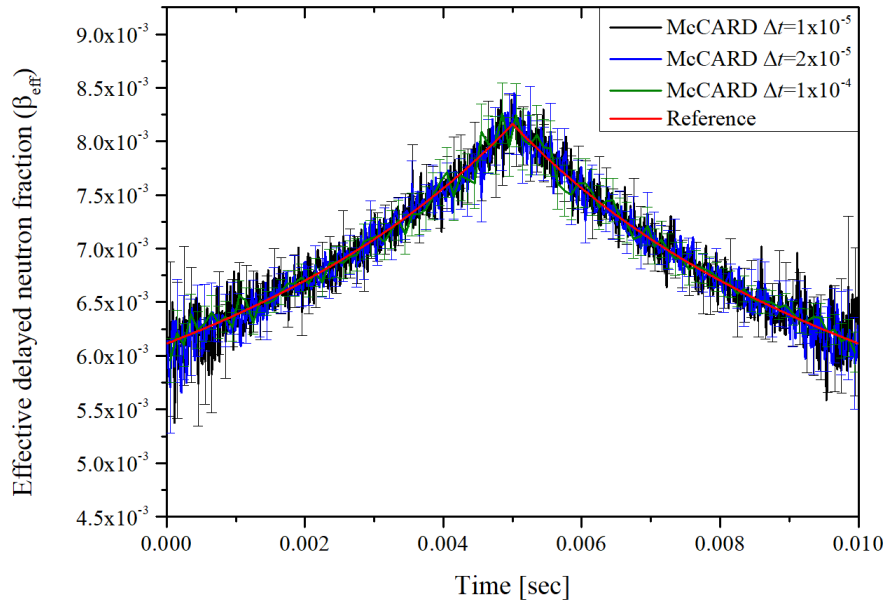


Figure 5.10 Comparison results of  $\beta_{\text{eff}}$  regarding  $\Delta t$  ( $L = 1 \times 10^{-3}$  sec)



## 5.3. Point Kinetics Analysis

### 5.3.1. C5G7-TD Benchmark Problem

As for the application of the estimated time-dependent kinetics parameters, the point kinetics analysis is conducted to predict the behavior of the system in a transient state. The C5G7-TD benchmark is selected as an application problem in which the transient starts from the initially critical state. Among the problems, the TD2-1 2D problem which postulates the insertion and withdrawal of control rod bank 1 is chosen and the kinetics parameters are estimated along the time.

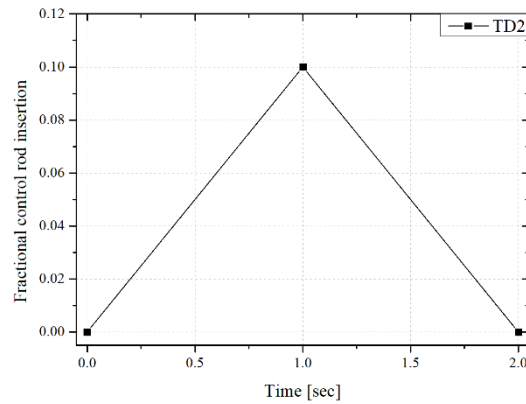


Figure 5.11 Transient scenario of TD2 problems

McCARD TDMC simulation is conducted using 100,000 neutron histories and 10,000 precursors with 0.2 ms time interval. The kinetics parameters  $\Lambda$  and  $\beta_{\text{eff}}$  are calculated at each time step with the adjoint convergence interval of 1 ms and the estimated values are averaged every 5 ms interval. Figure 5.12 and 5.13 shows the time-dependent  $\Lambda$  and  $\beta_{\text{eff}}$  estimates. The black lines are the kinetics parameters estimated from the TDMC simulation and the red lines are the kinetics parameters

calculated from the conventional  $k$ -eigenvalue calculation weighted by the  $k$ -adjoint.  $k$ -adjoint weighted kinetics parameters are calculated by McCARD  $k$ -eigenvalue calculation using 400,000 neutron histories for 200 active cycles after 100 inactive cycles. One can see that the kinetics parameters decrease from the critical state value as the control rods are inserted and get back to the critical state value as the control rods are withdrawn. At the critical state, the estimated kinetics parameters are matched with the  $k$ -adjoint weighted kinetics parameters within stochastic errors.

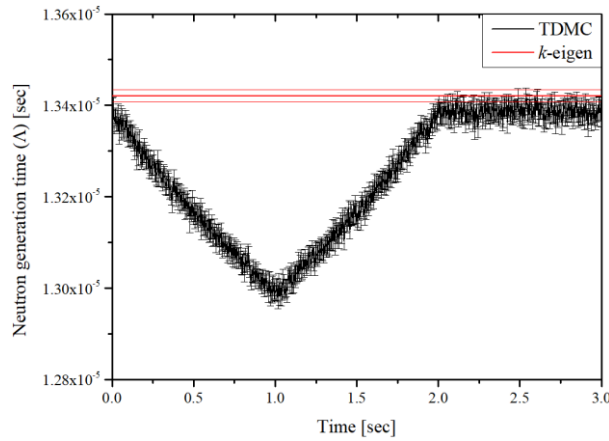


Figure 5.12 Estimated  $\Lambda$  from the TDMC simulation for TD2-1

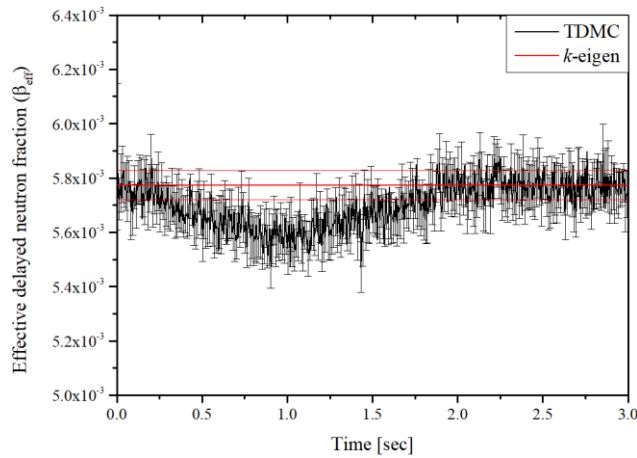


Figure 5.13 Estimated  $\beta_{\text{eff}}$  from the TDMC simulation for TD2-1

Using the estimated kinetics parameters, the point kinetics analysis is conducted and compared with the reference TDMC simulation result of the fractional core fission rate. Figure 5.14 shows the trend of relative amplitudes calculated by PKE with different kinetics parameters and their errors. The reactivity is calculated from the TDMC simulation as a core dynamic reactivity and is used for all point kinetics analyses. The PKE analyses are conducted with the kinetics parameters which are estimated from the  $k$ -eigenvalue calculation weighted by the  $k$ -adjoint, the TDMC calculation weighted by the detector response at 0.5 seconds and 1.0 seconds. It shows similar differences near the initial critical state, however, as the system becomes subcritical with the insertion of CRs, the PKEs from the TDMC simulation match with the reference better than that from the  $k$ -eigenvalue calculation. The PKE from the  $k$ -eigenvalue calculation shows about 6% differences in the subcritical state, whereas the PKEs from the TDMC simulation at 0.5 and 1.0 seconds give 4% and 3% differences respectively. This is because the shape function and adjoint function at the selected states during the CR insertion reflect the behavior of neutrons in the transient system better than that of the critical state. Figure 5.15 is the enlarged picture between 0 and 1 second in Figure 5.14, and the difference between the results can be seen more clearly.

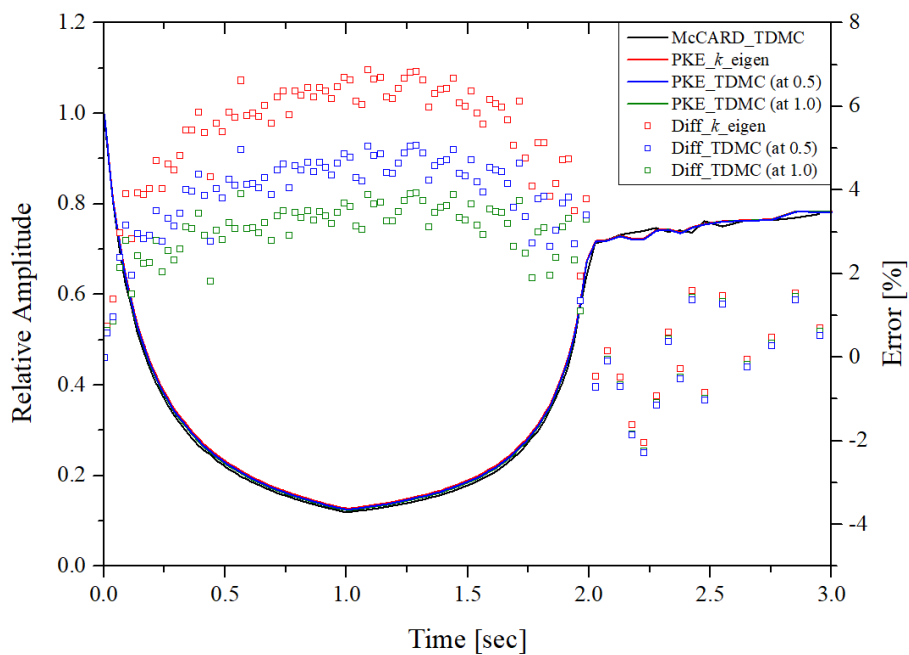


Figure 5.14 Comparison of PKEs with different kinetics parameters for TD2-1

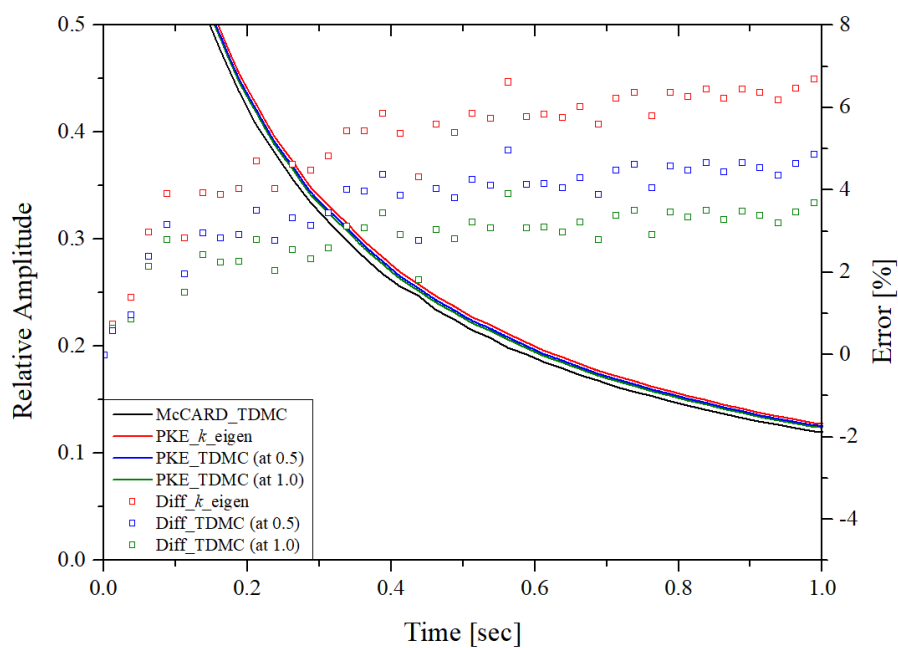


Figure 5.15 Comparison of PKEs with different kinetics parameters  
for TD2-1 (enlarged)

### 5.3.2. Numerical Beam Trip Experiment in KUCA

For the application of point kinetics analysis in an initially subcritical case, the thorium-loaded ADS benchmark [38] at KUCA is selected as the target problem. The benchmark is composed of various subcritical core configurations with different thorium-loaded fuel assemblies. Each assembly consists of  $5.08 \times 5.08$  cm coupon-shaped plates stacked inside the  $5.53 \times 5.53$  cm aluminum sheath of 1mm thickness. Among the various core configurations, Th-HEU-Gr-PE core with the deepest subcriticality with  $k_{\text{eff}}$  of 0.35473 is chosen. The fuel assembly and the core configuration is given in Figure 5.16 and 5.17. The fuel assembly consists of thorium and 93% highly enriched uranium fuel, graphite and polyethylene moderator and reflector. The overall height of the fuel assembly is 152.4 cm with 60 cm long layers of the upper and lower polyethylene reflector and the fuel layers of approximately 25 cm long. The core consists of 25 fuel assemblies surrounded by polyethylene reflectors. The 14 MeV neutron source is generated near the one side of the fuel regions in an isotropic direction from the D-T reaction by injecting a deuterium beam into the tritium target. The numerical experiment of a beam trip is conducted with the TDMC simulation and the time-dependent kinetics parameters are estimated after the beam trip.

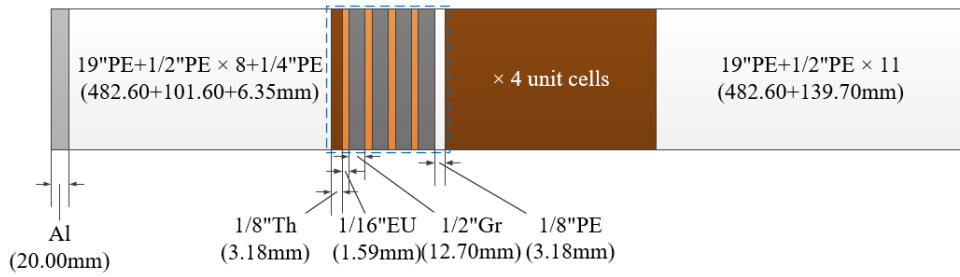


Figure 5.16 Fall sideways view of Th-HEU-Gr-PE fuel assembly

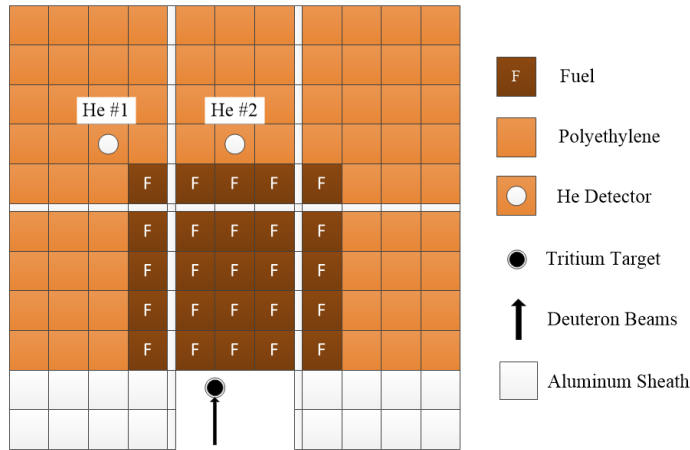


Figure 5.17 Configuration of the Th-HEU-Gr-PE core

McCARD TDMC calculation is conducted using 1,000,000 neutron histories and 1,000,000 precursors with 0.1 ms time interval. To simulate the beam trip experiment from the steady-state, the external source is uniformly simulated within each time step thorough the steady-state simulation. The number of fission source convergence steps and precursor generation steps are set to be 100 and 500 steps respectively. The transient simulation after the beam trip is conducted for 0.01 second and the adjoint convergence interval is set to 1.0 second. For the comparison, the  $k$ -adjoint weighted kinetics parameters are estimated from the  $k$ -eigenvalue calculation. In addition, the kinetics parameters weighted by the solution of the

inhomogeneous adjoint equation for the reference subcritical state with external sources are estimated from the fixed source calculation.  $k$ -eigenvalue calculation is done using 400,000 neutron histories for 200 active cycles after 100 inactive cycles. The fixed source calculation is done using 80,000,000 neutron histories for 50 replica calculations. In all calculations, JENDL-4.0 cross section library is used.

Figure 5.18 and 5.19 are the comparison results of the estimated kinetics parameters from each calculation. In Figure 5.18,  $\Lambda$  estimates increase rapidly after the beam trip at 0.01 second and converge to a lower value than the values at the steady-state as the delayed neutrons become dominant. The  $\Lambda$  estimate of the fixed source calculation matches well with the estimates of the TDMC simulation at the steady-state, but the  $\Lambda$  estimate of the  $k$ -eigenvalue calculation shows some difference. As for the  $\beta_{\text{eff}}$ , there is no significant difference before and after the beam trip in the TDMC estimates and similar values are calculated in other two estimates.

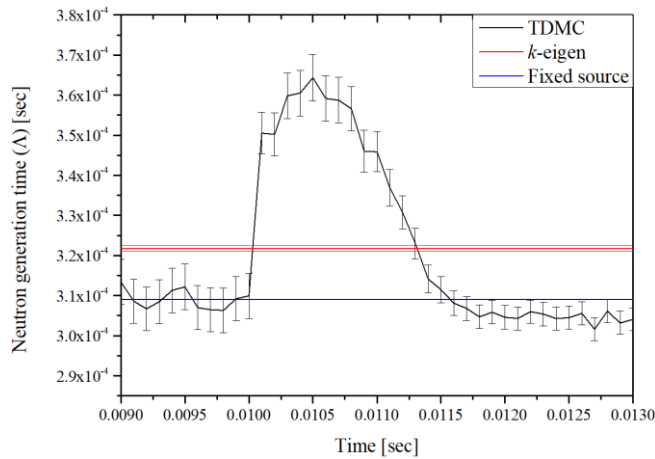


Figure 5.18 Estimated  $\Lambda$  for the beam trip experiment in Th-HEU-Gr-PE core

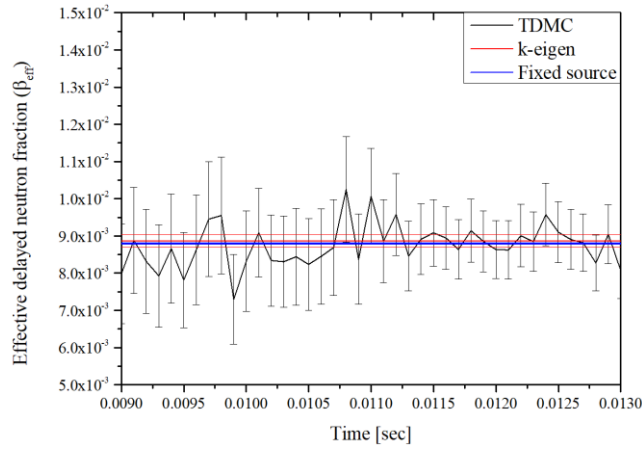


Figure 5.19 Estimated  $\beta_{\text{eff}}$  for the beam trip experiment in Th-HEU-Gr-PE core

The point kinetics analyses are performed using the estimated kinetics parameters after the beam trip. The time-dependent core fission rate from the TDMC simulation is used as the reference and all results are normalized as a relative value with respect to the initial steady-state. The reactivity is calculated as the conventions in the PKE with the  $k$ -eigenvalue calculation, while it is set to 0 in the PKE with the fixed source calculation and the TDMC calculation since the system is not change over time in the ADS PKE [36]. The red line and blue line are PKE results using the kinetics parameters estimated from  $k$ -eigenvalue calculation and fixed source calculation. The squared boxes present the difference with the reference. The fixed source case predicts the system behavior the best at the very beginning of the beam trip since it reflects the effect of the initial source distribution. However, as the source distribution is moved to the fundamental mode solution without an external source, the  $k$ -eigenvalue case fits the reference trend better than the fixed source case between 10.5 ms and 11.5 ms where the estimated  $\Lambda$  of  $k$ -eigenvalue fits to the TDMC results better than the fixed source case. At the end where the delayed



neutrons are dominant, both results show a similar trend. The green line is the PKE result obtained by adjusting the exact kinetics parameters at each time step. Overall, it best matches the reference among the results by reflecting the adequate neutron distribution and importance over time.

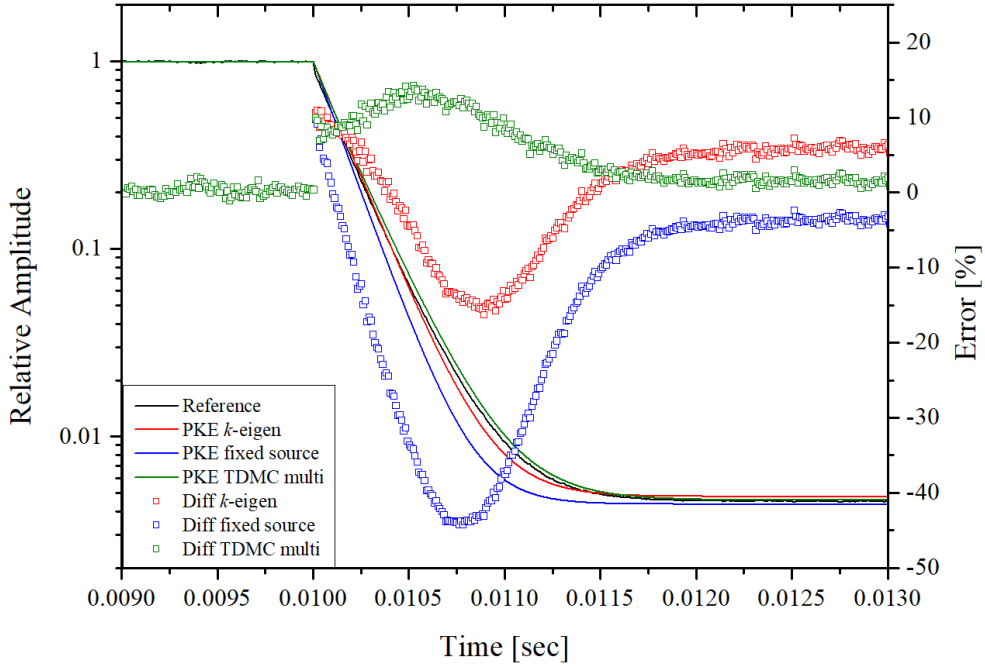


Figure 5.20 Comparison of PKEs with different kinetics parameters for the beam trip experiment in Th-HEU-Gr-PE core

The significance of the developed method is that it can provide the method to calculate kinetics parameters applying the exact shape function and adjoint response of that time independent of the system. In the conventional approaches of the PKE, it deals with the problem of accurately predicting the system behavior in transient based on the steady-state flux and its adjoint function. However, in the developed method, the PKE model is established based on any transient state by estimating

kinetics parameters using the time-dependent shape function and its time-dependent adjoint response. It can be said that the PKE domain is generalized from the steady-state to arbitrary states including transient states and the framework for the point kinetics analysis in the generalized time domain is suggested. The developed method is expected to be used in the quasi-static MC method to estimate kinetics parameters at each time step by weighting the time-dependent adjoint response and the accuracy is expected to be significantly improved compared to the conventional steady-state adjoint weighting case.

## **Chapter 6. Neutronics and Thermal-hydraulic Coupled Transient Analysis System**

### **6.1. McCARD/CUPID Coupled Analysis System**

The reactor transient analysis requires the capability for considering thermal hydraulic feedback effects caused by the power deviation in transient scenarios. McCARD equips with a simple one-dimensional T/H feedback module [12] but it cannot take into account the coolant mixing effects in sub-channels, which can lead to major errors in the accuracy of the results. Therefore, McCARD is coupled with the 3D sub-channel code CUPID, which is developed in KAERI, to establish multi-physics module for the transient analysis. The coupling is performed using the TCP/IP socket communication. The TCP/IP socket communication enables the real time bi-directional communication between the server and the client through the designated port. It has also the advantage of high scalability since it can easily implement the data transmission and reception modules once establish the interface. To minimize the modification of the codes, McCARD and CUPID is coupled externally through the server module but internally exchange data through memory using server module.

Figure 6.1 is a flow chart of the McCARD/CUPID module. McCARD and CUPID are connected to the server module using a designated address and a port number. After checking the connection and the dimension of coupling variables, it starts the simulation. When the simulation starts, McCARD calculates the relative 3D pin power distribution with the given temperature and density. CUPID calculates the temperature and density of the coolant and the temperature of the fuel and

cladding based on the pin power distribution. The calculated coupling data are exchanged through the server module. Table 6.1 is the list of the coupling variables. The coupling calculation is performed iteratively until it satisfies the temperature convergence criteria or the maximum number of iterations in the steady-state simulation or until the specified time boundary in the transient simulation.

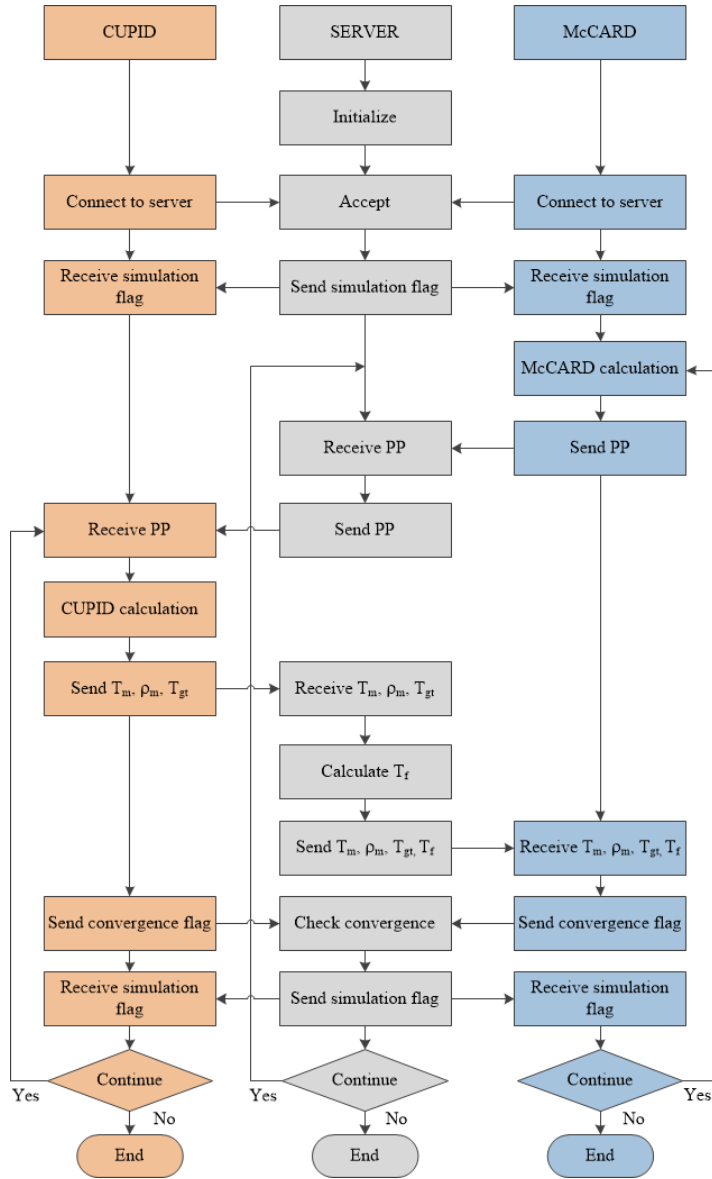


Figure 6.1 McCARD/CUPID coupled analysis system

Table 6.1 Coupling variables of McCARD/CUPID coupled analysis system

Transmit	Receive	Coupling variable [Unit]
McCARD	CUPID	3D relative pin power distribution
		Coolant average temperature [K] Coolant density [g/cc]
CUPID	McCARD	Fuel centerline temperature [K] Fuel surface temperature [K] Cladding average temperature [K]
		Guide tube average temperature [K] Guide tube coolant density [g/cc] Guide tube cladding average temperature [K]

Since the structure of the radial and axial nodes are different according to the code and problem, the data should be adjusted for the control volume before it is transferred to one another. In general, since neutron transport codes deal with unit cells of a control rod and sub-channel codes deal with unit cells of a channel, the coolant data need to be adjusted in the radial direction. The radial adjustment is conducted using the area ratio of the lattice geometry as

$$T_M^j = \frac{\sum_{i=1}^N T_C^i \times A_{ij}}{\sum_{i=1}^N A_{ij}} = \sum_{i=1}^N T_C^i \times R_{ij} , \quad (6.1)$$

where  $i$  and  $j$  are the radial lattice index of CUPID and McCARD and subscript  $C$  and  $M$  indicate CUPID and McCARD respectively.  $A_{ij}$  is the area of the  $i$ -th CUPID lattice superimposed on the  $j$ -th McCARD lattice. With the radial mapping data

depicted in Figure 6.2, McCARD unit cell data is calculated by weighting 0.25 to the surrounding four sub-channel data.

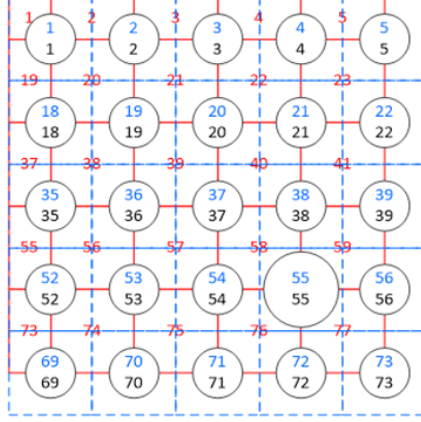


Figure 6.2 Radial lattice and data mapping

As for the axial direction, data adjustment is conducted using the ratio of the axial lattice length as

$$P_C^i = \frac{\sum_{j=1}^N P_M^j \times L_{ji}}{L_C^i} = \sum_{i=1}^N P_M^i \times R_{ji}, \quad (6.2)$$

where  $L_{ji}$  is the length of  $j$ -th McCARD lattice superimposed on the  $i$ -th CUPID lattice. Figure 6.3 shows the example of the axial lattice and data mapping.

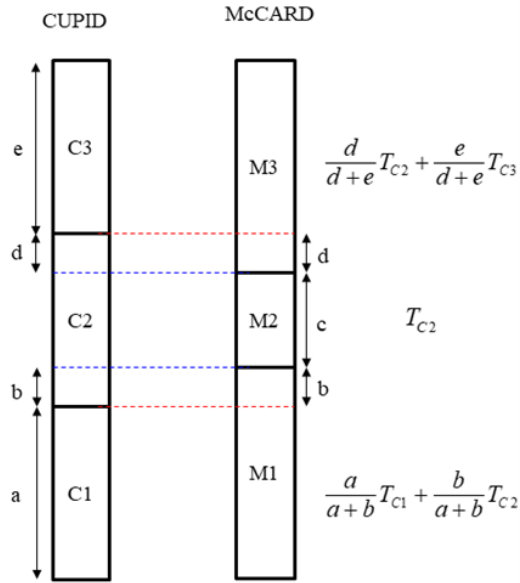


Figure 6.3 Axial lattice and data mapping

It is noted that the McCARD/CUPID coupling is parallelized to exchange data and calculate the coupling variables in both codes simultaneously for the efficiency in the steady-state calculation. On the other hand, when the transient analysis starts, the coupling is serialized to exchange data and calculate the variables in order. In addition, due to the difference in data time, that is the power distribution calculated from McCARD is the average value of the time step, while CUPID requires the data at the time boundary, so the power density is linearly extrapolated before being transmitted to CUPID.

## 6.2. Numerical Results

### 6.2.1. VERA Benchmark Steady-state Problem

To verify the developed McCARD/CUPID coupled analysis system, the VERA #6 hot full power problem is analyzed among the VERA 3D assembly problems.

VERA assembly is a 17 by 17 Westinghouse type PWR assembly which consists of 264 3.1% enriched uranium fuel rods, 24 guide tubes, and an instrumentation tube. The fuel rod is axially divided into 23 layers with 6 internal spacer grids and 2 spacer grids at both ends. The total height of the fuel rod is 418.937 cm with the active core of 365.760 cm. Figures 6.4 and 6.5 are radial and axial cross-sectional view of the assembly respectively.

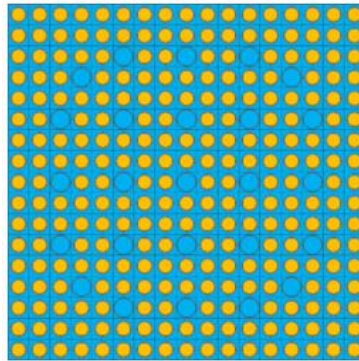


Figure 6.4 Radial cross-sectional view of the VERA #6 assembly

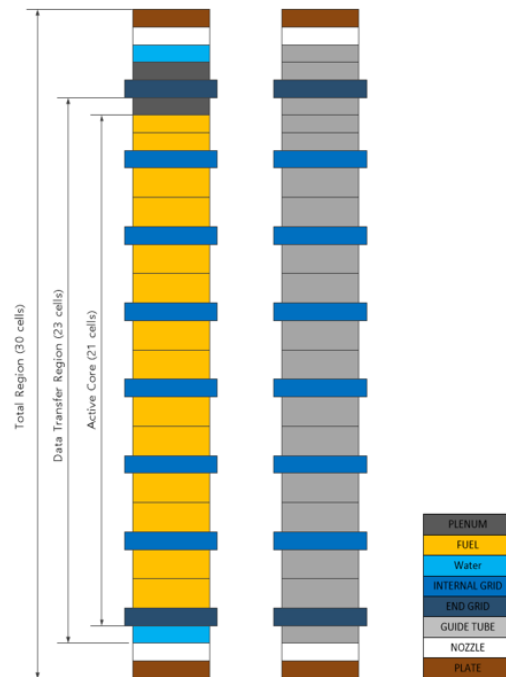


Figure 6.5 Axial cross-sectional view of the VERA #6 assembly



Total 23 cells in the axial direction including the active core and the adjacent cells are coupled for the McCARD/CUPID coupled calculation. In the McCARD model, the upper and lower cells which are not coupled use the temperature and density data from the adjacent cells. The dimension of the assembly and material composition follow the benchmark. The operation condition at HFP are given in Table 6.2.

Table 6.2 Operation condition of VERA #6 HFP assembly problem

Contents [Unit]	Value
Average power [MW]	17.670
Exit pressure [MPa]	15.513
Inlet temperature [K]	565.000
Average mass flux [kg/sec-m <sup>2</sup> ]	3457.620
Boron concentration [ppm]	1300.000

The developed McCARD/CUPID coupled analysis system is verified by comparing with the previous analysis results of the McCARD/MATRA coupled analysis system. McCARD calculation is done with 500,000 neutron histories for 200 active cycles after 100 inactive cycles. The number of coupled iteration is set to 13. Among the iterations, 3 iterations are conducted with the gradually increasing scheme as 66, 132, and 200 cycles to get the roughly converged temperature distribution. The remaining 10 iterations are conducted with the maximum cycle number of 200 for the accurate temperature convergence. The ENDF/B-VII.0 is used for the cross section library. The cross section libraries are processed by the Gauss-Hermite quadrature on the fly Doppler broadening module based on the libraries

produced at 300K intervals and the stochastic mixing method is used for the thermal scattering libraries.

Both McCARD/CUPID and McCARD/MATRA calculation are conducted for 13 iterations. After the calculation, the effective multiplication factor is calculated as  $1.16717 \pm 0.00006$  and  $1.16708 \pm 0.00007$  for McCARD/CUPID and McCARD/MATRA respectively, which match well within the stochastic errors. Figures 6.6 and 6.7 are the maximum fuel and coolant temperature deviation along the iteration. The fuel temperatures are converged within 10 K after the 5-th and 6-th iterations in the McCARD/CUPID and McCARD/MATRA calculation, while the coolant temperatures are converged within 0.1 K after the 7th iteration in both cases. The initial deviation is large in McCARD/CUPID calculation because CUPID uses zero power initial distribution for the first calculation whereas cosine shape power distribution is assumed in MATRA. The convergence criterion for the coupled calculation is set to maximum 10 K and it shows sufficient convergence through the 13 iterations.

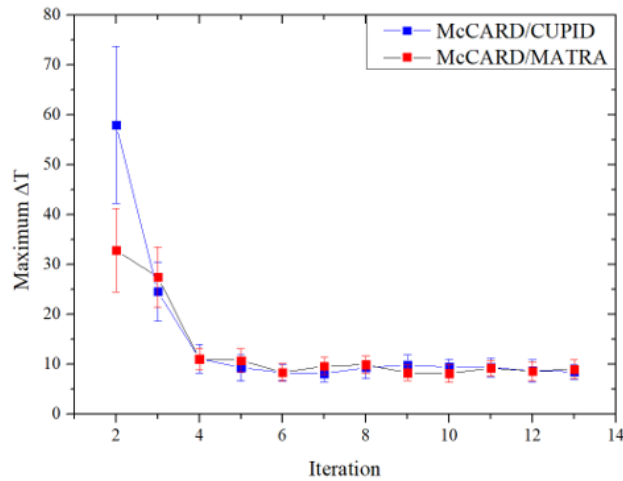


Figure 6.6 Trend of the fuel temperature convergence in VERA #6 problem

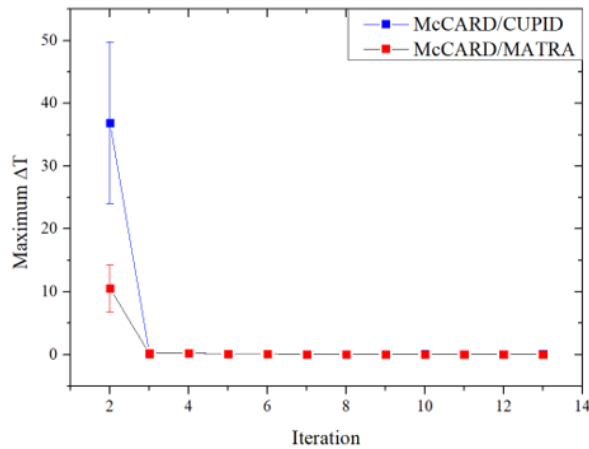


Figure 6.7 Trend of the coolant temperature convergence in VERA #6 problem

Figure 6.8 is the comparison result of the axial power distribution. Overall power distribution match within 3% and 1% from the 5-th layer. The dents of the power distribution is the location where the spacer grids exist. One can see the lower power distribution as the flow rate decreases and the pressure drops at these locations. In Figure 6.9, the radial power distribution is compared. It shows a good agreement within the stochastic errors and the maximum difference is 0.17%. The fuel and coolant temperatures are also compared between two coupled system. Figures 6.10 and 6.11 are the comparison results of the coolant exit temperature and fuel temperature. The coolant exit temperature math well showing the maximum difference of 0.21 K or 0.06% as the relative difference and the fuel temperature shows maximum 12.12 K or 1.55% difference.



McCARD/CUPID
McCARD/MATRA
Difference

Figure 6.10 Comparison of the coolant exit temperature in VERA #6 problem

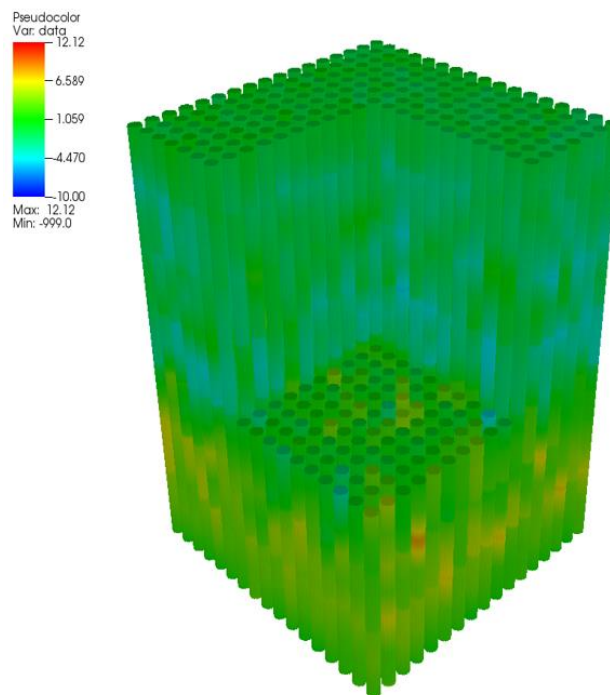


Figure 6.11 Comparison of the fuel temperature in VERA #6 problem

### 6.2.2. VERA Benchmark Transient Problem

In this section, the capability of the McCARD/CUPID coupled transient analysis system is not thoroughly verified. Instead, the integrity of the coupled system is checked by analyzing the postulated transient scenario for the VERA #6 problem and observing the Doppler effect. To simulate rod ejections of the fuel assembly, the guide tubes in the VERA #6 problem is changed to control rods with AIC absorber in them. The initial condition is assumed to be the hot zero power with  $10^{-4}$  % of the nominal power. All control rods are positioned at the 16.22 % height of the active core in the initial state and it is assumed to be at critical state. The quarter part of the control is ejected immediately at 0.01 second so that the 1.12\$ reactivity will be inserted by fully ejecting the control rods. The control rods that are ejected as the transient scenarios are depicted in the figure below with red color.

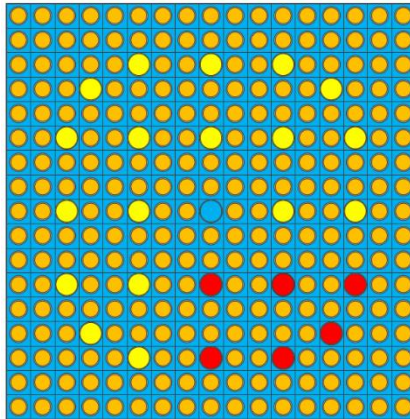


Figure 6.12 Location of the postulated control rods ejection (red colored)

McCARD/CUPID calculation is conducted using 100,000 neutron histories and precursors with 100 and 200 time steps for fission source convergence and precursor generation. The time interval is set to be 0.1 ms and the coupling frequency for the temperature update is set to be 2 ms, which exchanges data for every 20 time step calculations. Figure 6.13 is the McCARD/CUPID coupled calculation result of the core power after the control rod ejection. It can be seen that the Doppler effect gives the negative feedback to the power increase as the fuel temperature is increased, and it converges to the new equilibrium state. Figure 6.14 is the trends of the average fuel temperature and the coolant exit temperature. One can see that the fuel temperature increases rapidly with the initial power increase but it decelerates due to the Doppler effect and increases constantly as the power converges. The fuel temperature is expected to converge to a value corresponding to the converged power level. The coolant temperature also changes with the power increase but shows a relatively slow increase due to the large heat capacity. Figures 6.15 and 6.16 are the power distribution and fuel temperature profile at 0.23 second. Both results show the corresponding power and temperature increase in the quarter parts of the core where the control rods are ejected.

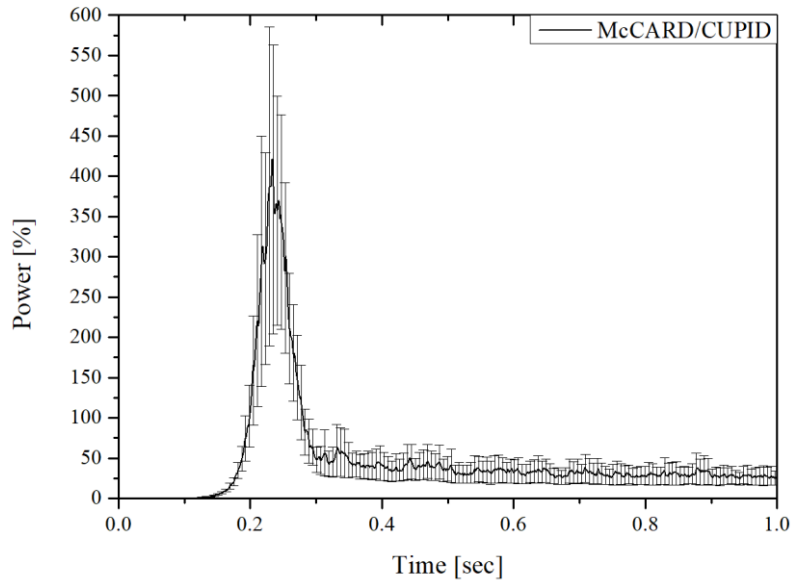


Figure 6.13 Trend of the power after the rod ejection

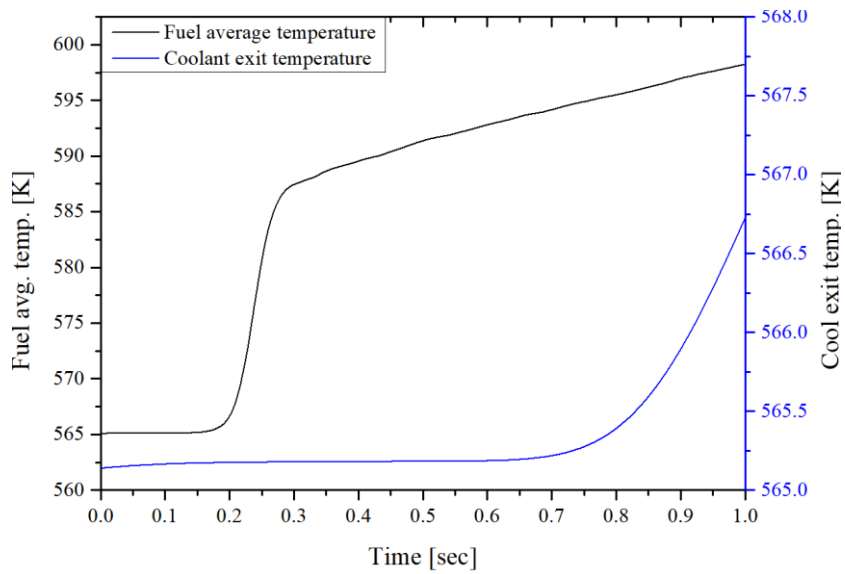


Figure 6.14 Trends of the fuel and coolant temperature after the rod ejection



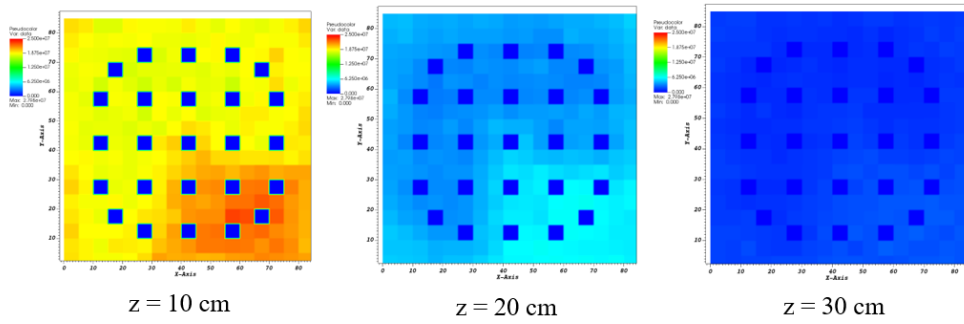


Figure 6.15 Power distribution at 0.23 second

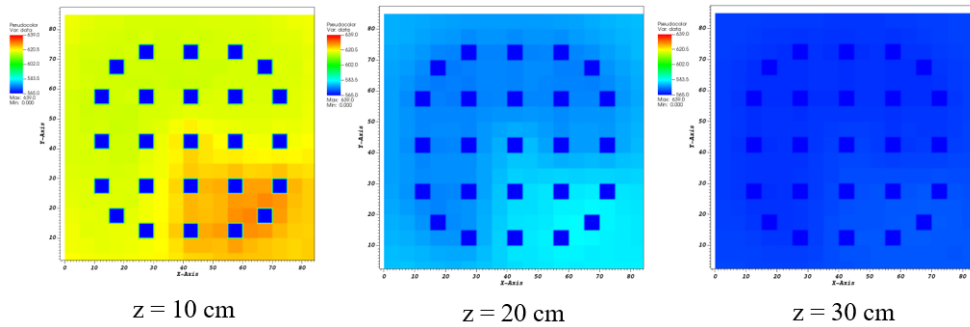


Figure 6.16 Fuel temperature profile at 0.23 second

From the power and temperature trends, one can see that the temperatures are changing smoothly while the power is fluctuating. This is due to the heat capacity of a material acting as thermal inertia to prevent rapid changes in temperature. In reality, such fluctuation in power may not be observed because there are much more neutrons than the simulation and the thermal feedback occurs continuously. Considering the stochastic errors shown in the figure, smooth power shape could be obtained if a much larger number of neutrons were simulated. From the same point of view, such fluctuation can exist in a transient state of a very low power although the change will be very small and difficult to measure.

## Chapter 7. Conclusion

In this thesis, advanced time-dependent Monte Carlo methods are developed to perform a more accurate and reliable analysis for the realistic reactor transient problems. The capability of the TDMC simulation in McCARD has enhanced and the applicability of the developed TDMC methods has extended.

The conventional TDMC algorithm using the analog MC branching method with the combing method for population control is implemented with some improvements by eliminating the scale factor and introducing the dynamic weight window for an efficient neutron simulation. The TDMC simulation with the population control is applied to the PNS alpha measurement. With the time-dependent tally of neutrons from the TDMC simulation, an optimum detector position search algorithm is developed to resolve the dependency issue of the PNS alpha measurement. The developed method is applied to the Pb-Bi-zoned experimental benchmark at KUCA and numerical experiments at AGN-201K. It is shown that the developed method predicts the relative alpha convergence at different detector positions well. An optimum detector position is searched at both cores by comparing the amplitude of signals from detectors after the convergence. The sensitivity of an optimum detector position to initial source positions is also examined.

For the transient analysis starting from the initial steady-state, the delayed neutron treatment with the forced decay algorithm and the TDMC steady-state simulation method with the precursor density normalization scheme are implemented. In addition, new features of moving geometry treatment is developed to extend its capability to the three-dimensional transient analysis. The developed

method is verified to the C5G7-TD 2D and 3D problems and it shows good agreements with the results of nTRACER within the stochastic errors.

The history-based batch method in the TDMC simulation is developed for the unbiased variance estimation. The conventional variance estimation method which stochastically processes the tally estimates per neutron gives highly biased results due to the correlations among the neutrons. The history-based batch method disconnects this correlation by simulating neutrons and processing the tally estimates batch-wisely. The developed method is verified in infinite homogeneous two-group problems and C5G7-TD benchmark problems and it gives unbiased variance for the tally means. From the variance estimation of the time-dependent tally, it is found that the error is propagated in the TDMC simulation through the weight normalization scheme in the population control. However, when the delayed neutrons are dominant than the survival neutrons, it keeps errors from propagating largely.

As an application of the TDMC simulation, a time-dependent kinetics parameter estimation method is developed reflecting the exact flux shape and adjoint response. Based on the physical meaning of the adjoint response, the MC algorithm called Contribution method can be used to estimate the kinetics parameters by making additional particles for the adjoint calculation. But, it has serious limitations in calculation speed and application ranges for practical use. Therefore, with some reasonable assumptions, efficient MC algorithms are proposed for the kinetics parameter estimation. The algorithms are verified in infinite homogeneous two-group problems and show good agreement with the reference solutions. It also shows more than 1,000 times the efficiency than the conventional method near the critical cases. The developed methods are applied to the C5G7-TD problem and numerical beam trip experiment at KUCA for the estimation of the kinetics parameters. The

estimated kinetics parameters are used for the point kinetics analysis of the system and compared with the one using the conventional kinetics parameters. It is expected to be utilized for exploring the best estimates of the kinetics parameters that can predict the transient situation better.

Finally, in order to consider the thermal-hydraulic feedback in the realistic reactor transient analysis, McCARD is coupled with the 3D sub-channel code CUPID using the TCP/IP socket communication. The McCARD/CUPID coupled system is verified in the steady-state problem of VERA #6 HFP assembly compared to the previously built McCARD/MATRA system. The results match well with the McCARD/MATRA system showing the maximum difference of 0.17% in power distribution, 0.06% in coolant exit temperature, and 1.55% in fuel temperature. To conduct a coupled transient analysis, the VERA #6 problem is modified to a simple rod ejection problem and it is analyzed using the coupled system. The integrity of the coupled system is checked by observing the Doppler effect from the temperature feedback of the fuel, but more verification is needed for the problems with comparison results.

## Bibliography

- [1] S. Goluoglu et al., “Development of a Time-Dependent Three-Dimensional Deterministic Neutron Transport Method,” *Trans. Am. Nucl. Soc.*, **76**, 219 (1997).
- [2] M. Shayesteh and M. Shahriari, “Calculation of Time-Dependent Neutronic Parameters Using Monte Carlo Method,” *Ann. Nucl. Energy*, **36** (7), pp. 901-909 (2009).
- [3] Y. G. Jo, B. H. Cho, and N. Z. Cho, “Nuclear Reactor Transient Analysis by Continuous-Energy Monte Carlo Calculation Based on Predictor-Corrector Quasi-Static Method,” *Nucl. Sci. Eng.*, **183**, pp. 229-246 (2016).
- [4] E. L. Kaplan, “Monte Carlo Methods for Equilibrium Solutions in Neutron Multiplication,” UCRL-5275-T, Lawrence Livermore National Laboratory (1958).
- [5] T. E. Booth, “A Weight (Charge) Conserving Importance-Weighted Comb for Monte Carlo,” LA-UR-96-0051, Los Alamos National Laboratory, NM, USA, (1996).
- [6] D. Legrady and J. E. Hoogenboom, “Scouting the Feasibility of Monte Carlo Reactor Dynamics Simulations,” *Proc. PHYSOR 2008*, Interlaken, Switzerland, Sep 14–19 (2008).
- [7] B. L. Sjenitzer and J. E. Hoogenboom, “Dynamic Monte Carlo Method for Nuclear Reactor Kinetics Calculations,” *Nucl. Sci. Eng.*, **175**, pp. 94-107 (2013).
- [8] N. Shaukat, M. Ryu, and H. J. Shim, “Dynamic Monte Carlo Transient Analysis for the Organization for Economic Co-operation and Development Nuclear Energy Agency(OECD/NEA) C5G7-TD Benchmark,” *Nucl. Eng. Technol.*, **49**, pp. 920-927 (2017).
- [9] T. E. Valentine and J. T. Mihalcz, “MCNP-DSP: A Neutron and Gamma Ray Monte Carlo Calculation of Source-Driven Noise-Measured Parameters,” *Ann. Nucl. Energy*, **23** (16), 1271 (1996).
- [10] U. Wiącek and E. Krynicka, “Decay of the pulsed thermal neutron flux in two-zone hydrogenous systems – Monte Carlo simulations using MCNP standard data libraries,” *Nuclear Instruments and Methods in Physics Research Section B: Beam Interactions with Materials and Atoms*, **243** (1), 92 (2006).
- [11] N. Shaukat, “Effective Realization of Time Dependent Monte Carlo Simulation Method for Nuclear Reactor Transient Analysis,” PhD Thesis, Seoul National University (2017).
- [12] H. J. Shim, B. S. Han, J. S. Jung, H. J. Park, and C. H. Kim, “McCARD: Monte Carlo code for advanced reactor design and analysis,” *Nuclear Engineering and Technology*, **44** (2), pp. 161–176, (2012).
- [13] C. H. Pyeon, “Experimental Benchmarks of Neutronics on Solid Pb-Bi in

- Accelerator-Driven System with 100 MeV Protons at Kyoto University Critical Assembly,” KURRI-TR-447, Research Reactor Institute, Kyoto University (2017).
- [14] M. H. Kim, “Research & Educational Reactor AGN-201K”, Reactor Research & Education Center, Kyung Hee University (2018).
- [15] V. F. Boyarinov et al., “Deterministic Time-Dependent Neutron Transport Benchmark without Spatial Homogenization (C5G7-TD),” Version 1.9, NEA/NSC/DOC(2016), OECD Nuclear Energy Agency (2018).
- [16] Y. S. JUNG et al., “Practical Numerical Reactor Employing Direct Whole Core Neutron Transport and Subchannel Thermal/Hydraulic Solvers,” *Ann. Nucl. Energy*, **62**, pp. 357-374 (2013).
- [17] H. J. Shim, S. H. Choi, and C. H. Kim. “Real variance estimation by grouping histories in Monte Carlo eigenvalue calculations,” *Nucl. Sci. Eng.*, **176**(1), pp. 58-68, (2014).
- [18] M. L. Williams, “The Relations Between Various Contribution Variables Used in Spatial Channel Theory Applied to Reactor Shielding Analysis,” *Nucl. Sci. Eng.*, **63**, 220 (1977)
- [19] “CUPID Code Manuals Vol. 1: Mathematical Models and Solution Methods (version 2.2)”, Thermal Hydraulics and Safety Research Division Korea Atomic Energy Research Institute, KAERI, August, (2018).
- [20] H. Kwon, et al. "Validation of a Subchannel Analysis Code MATRA Version 1.1." KAERI/TR-5581/2014 (2014).
- [21] A. T. Godfrey, “VERA Core Physics Benchmark Progression Problem Specifications,” Oak Ridge National Laboratory, CASL-U-2012-0131-004, Rev. 4 (2014).
- [22] F. R. N. McDonnell and M. J. Harris, “Pulsed-source Experiments in a Reflected Coupled-core Reactor-I. Reactivity Measurements,” *Journal of Nuclear Energy*, **26** (3), pp. 113-128 (1972).
- [23] C. H. Pyeon et al., “Experimental Benchmarks on Kinetic Parameters in Accelerator-driven System with 100 MeV Protons at Kyoto University Critical Assembly,” *Annals of Nuclear Energy*, **105**, pp. 346-354 (2017).
- [24] Taninaka et al., “Determination of Lambda-mode Eigenvalue Separation of a Thermal Accelerator-driven System from Pulsed Neutron Experiment,” *Journal of nuclear science and technology*, **47** (4), pp. 376-383 (2010).
- [25] R. Katano. “Estimation Method of Prompt Neutron Decay Constant Reducing Higher Order Mode Effect by Linear Combination,” *Nuclear Science and Engineering*, **193** (4), pp. 431-439 (2019).
- [26] T. Suzaki, “Subcriticality Determination of Low-Enriched UO<sub>2</sub> Lattices in Water by Exponential Experiment,” *Journal of Nuclear Science and Technology*, **28** (12), pp. 1067-1077 (1991).

- [27] H. J. Shim, S. H. Jang, and S. M. Kang, "Monte Carlo Alpha Iteration Algorithm for a Subcritical System Analysis," *Science and Technology of Nuclear Installations*, **2015**, pp. 1-7 (2015).
- [28] G. R. Keepin, "Physics of Nuclear Kinetics," Addison-Wesley, (1965).
- [29] E. M. Gelbard and R. Prael, "Computation of Standard Deviations in Eigenvalue Calculations," *Prog. Nucl. Energy*, **24**, 237 (1990).
- [30] T. Ueki, T. Mori, and M. Nakagawa, "Error Estimations and Their Biases in Monte Carlo Eigenvalue Calculations," *Nucl. Sci. Eng.*, **125**, 1 (1997).
- [31] H. J. Shim and C. H. Kim, "Real Variance Estimation Using an Inter-Cycle Fission Source Correlation for Monte Carlo Eigenvalue Calculations," *Nucl. Sci. Eng.*, **162**, pp. 98-108 (2009).
- [32] A. Bera and C. Jarque, "Efficient Tests for Normality, Homoscedasticity and Serial Independence of Regression Residuals: Monte Carlo Evidence," *Econ. Lett.*, **7**, 313 (1981).
- [33] H. W. Lilliefors, "On the Kolmogorov-Smirnov Test for Normality with Mean and Variance Unknown," *J. Am. Stat. Assoc.*, **64**, 387 (1967).
- [34] S. J. Jeong and H. J. Shim, "Uncertainty Propagation Analysis in Time-Dependent Monte Carlo Calculations with Combing Technique," *Transactions of Korean Nuclear Society Virtual Autumn Meeting*, Dec. 17-18, (2020).
- [35] K. O. Ott and R. J. Neuhold, "Introductory Nuclear Reactor Dynamics," La Grange Park (IL), American Nuclear Society, (1985).
- [36] H. J. Shim et al., "Estimation of Kinetics Parameters by Monte Carlo Fixed-source Calculations for Point Kinetics Analysis of Accelerator-driven System," *J Nucl. Sci. Technol.*, **57**(2), pp. 177-186 (2020).
- [37] S. A. H. Feghhi, M. Shahriari, H. Afarideh, "Calculation of Neutron Importance Function in Fissionable Assemblies using Monte Carlo Method," *Ann. Nucl. Energy*, **34** (6), pp. 514–520 (2007).
- [38] C. H. Pyeon, "Experimental Benchmarks on Thorium Loaded Accelerator-Driven System at Kyoto University Critical Assembly," KURR-TR(CD)-48, Research Reactor Institute, Kyoto University, Kyoto, Japan, (2015).

## 초 록

시간에 따른 중성자의 거동을 해석하는 것은 노심 기동 해석, 임계도 추정, 사고 해석, 연구용 원자로 실험 등 다양한 적용분야에서 노심의 동역학적 특성을 이해하는데 필수적이다. 원자로 과도해석은 정상상태 해석에 비해 많은 전산 시간이 필요하기 때문에 주로 결정론적 방법론이나 준정상상태 방법론에 의존해 왔으나 이 방법론들은 공간과 에너지 또는 시간에 대한 차별화 근사를 포함하기 때문에 부정확한 결과를 초래할 수 있다. 최근 지속적인 전산 성능의 향상과 고신뢰도 방법론들의 개발에 힘입어 근사가 없는 시간중속 몬테칼로(TDMC) 중성자 수송해석방법론에 대한 연구가 활발히 이루어지고 있으며 실제 시간 범위의 원자로 과도해석에 적용 가능한 대안이 되었다. 몬테칼로 방법론은 상용 원자로뿐만 아니라 차세대 원자로나 연구로 등 다양한 노심의 과도해석에 기준해를 제공할 수 있기 때문에 몬테칼로 과도해석 방법론의 개발은 매우 중요하다. 국내에서는 서울대학교에서 개발한 몬테칼로 코드인 McCARD가 TDMC 모의 기능을 갖추어 알파 고유치 계산과 과도해석을 수행한 적이 있으나 2차원 해석에 제한되고 편향된 분산을 예측하는 등 정밀하고 신뢰할만한 원자로 과도해석능을 갖추지 못하였다. 본 논문은 고신뢰도 과도해석 코드 개발의 필요성을 바탕으로 원자로 과도해석을 위한 TDMC 알고리즘을 고도화 개발하고 TDMC 모의의 적용성을 실질적인 문제에 확장하는 것을 목표로 한다.

TDMC 방법론은 기존의 몬테칼로 모의계산에 시간 구간을 도입하고 시간 구간별로 중성자 수송을 모의한 다음 각 시간 구간의 끝에서 중성자수를 제어함으로써 중성자의 지속적인 모의를 가능하게 한다. McCARD에서는 입자의 분기를 그대로 모의하는 아날로그 몬테칼로 분기법과 편향 없이 정확한 수의 중성자를 추출하는 빗질 방법을 중성자수 제어 방법으로 사용하였으며, 기존에 가중치 정규화 용도로 사용하던 축적 인자를 제거하고 동적 가중치창을 도입하여 알고리즘의 효율성을 개선하였다. 시간에 따른 중성자의 지속적인 모의가 가능한 TDMC 방법은 즉발중성자붕괴상수 알파를 예측하는 펄스중성자선원(PNS) 실험에 적용하였다. PNS 실험은 초기 선원과 노심의 기하학적 영향으로 검출기의 위치와 시간에 따라 서로 다른 결과가 측정되는 문제가 보고되어 왔는데 위치와 시간에 따른 중성자의 거동을 정확히 모의할 수 있는 TDMC 방법을 활용하여 PNS 알파 측정을 위한 최적의 검출기 위치를 찾는 탐색 알고리즘을 개발



하였다. 개발된 방법은 교토대 임계집합체(KUCA)의 납-비스무스 장전 실험 검증 문제와 AGN-201K의 모의 실험에 적용하였다. KUCA 실험 검증문제에서는 파쇄 중성자 선원의 영향이 잘 반영되어 서로 다른 검출기 위치에서의 알파 수렴성을 잘 예측하였으며 AGN-201K 모의 실험에서는 초기 선원 위치에 따른 계측의 민감도 평가가 수행되었다. 위치에 따른 수렴 시간에서 검출기 신호를 비교하여 신호가 가장 높은 곳을 최적의 검출기 위치로 선정하였고 이러한 적용 해석 결과는 실제 PNS 알파 계측 실험을 설계하고 수행하는데 있어 좋은 참고가 될 것으로 기대된다.

중성자수 제어 방법과 더불어 원자로 과도상태 모의에 있어 방법론적으로 중요한 부분이 지발중성자 모의법과 정상상태 모델링 방법이다. 즉발중성자와 지발중성자는 세대 시간에 큰 차이가 있기 때문에 핵분열로부터 지발중성자를 직접 추출하는 통상적인 방법은 큰 통계 오차를 일으킨다. 또한 대부분의 과도해석은 정상상태로부터 시작하기 때문에 초기 정상상태의 즉발중성자와 지발중성자 선원 분포를 모의할 수 있는 방법이 필요하다. 따라서 효율적인 지발중성자 모의를 위해 지발중성자 선행핵 모의를 통한 강제 붕괴 알고리즘을 도입하였고, 초기상태 모델링 방법으로는 계산 모드의 전환 없이 초기부터 과도상태까지 TDMC 모의법을 통해 일관적으로 초기 정상상태를 모델링할 수 있는 몬테칼로 정상상태 모의법을 사용하였다. 이 과정에서 초기 지발중성자 선행핵수를 정규화하는 알고리즘을 개선하였고 보다 실질적인 3차원 과도상태 시나리오를 모의할 수 있는 동적 구조물 처리 기능을 개발하였다. 개발된 McCARD 과도해석능은 원자로 과도상태 검증 계산 문제집인 C5G7-TD의 2차원 문제와 3차원 문제에 대해 nTRACER와 비교 검증하였다. 3차원 문제에서 제어봉의 축방향 삽입과 인출이 잘 모의되었으며 시간에 따른 노심 동적반응도 및 상대 핵분열 반응률은 통계 오차 이내에서 잘 일치하였다.

몬테칼로 계산은 일반적으로 표본 평균과 표본 평균의 분산을 통해 계산 결과의 정확도와 신뢰도를 제공하는데 McCARD 과도해석 모듈의 해석능을 검증하는 과정에서 일반적인 통계처리를 통해 얻은 TDMC 집계 평균의 표본 분산이 크게 편향되어 있는 것을 발견하였다. 이는 TDMC 계산의 분기 과정 및 중성자수 제어에서 중성자간에 상관관계가 생기기 때문인데 이러한 편향된 분산은 몬테칼로 계산 결과의 정확도 및 신뢰도를 판단하는데 왜곡된 정보를 주게 된다. 또한 집계 평균의 분산을 추정할 때 지발중성자의 기여도를 어떻게 할당하여 통계 처리해야 하는지에 대한 문제도 존재한다. 본 논문에서는 이러한 문

제를 해결하고 정확한 분산을 계산하기 위해 TDMC 모의에서의 히스토리 기반 배치법을 개발하였다. 히스토리 기반 배치법은 중성자와 선행핵을 묶어 배치별로 따로 모의하고 결과를 배치별로 통계처리하여 추정치 간 상관관계를 끊는 방법으로 동시에 지발중성자의 기여도 할당 문제도 기여도를 포함한 배치의 집계에 할당함으로써 자연스럽게 해결할 수 있다. 개발된 방법은 2군 무한균질문제와 C5G7-TD 검증 계산문제를 통해 검증하였고 배치의 크기가 충분할 경우 집계 평균에 대해 편향되지 않은 정확한 분산을 계산하였다. 또한, 검증과정에서 TDMC 모의 도중 오차가 전파되는 현상을 확인하였고 이것이 중성자수 제어의 가중치 정규화로부터 파생되어 살아남은 중성자들을 통해 전파된다는 것을 입증하였다. 한편 살아남은 중성자보다 지발중성자의 영향이 지배적인 시스템에서는 중성자가 오래 살아남지 못하고 지발중성자의 기여가 크기 때문에 오차가 크게 전파되지 않았다.

원자로 과도 해석을 위해 일점운동방정식 모델을 수립하거나 반응도 계측 실험을 수행할 때는 해당 노심의 동특성 인자 계산이 필요하다. 일반적으로는 과도상태에서 정확한 중성자속 분포를 얻기 어렵기 때문에 정상상태 수송방정식과 수반방정식의 해를 형상 함수와 가중 함수로 가정하고 동특성 인자를 계산한다. 그러나 TDMC 방법을 통해 시간에 따른 정확한 중성자속 분포를 모의할 수 있게 되면서 TDMC 모의를 이용하여 정확한 일점운동방정식에 기반한 시간중속 동특성 인자 계산법을 개발하였다. 특히 수반 응답 계산에 대해서는 계산 부담이 큰 기존의 기여자 모의법(Contributon method)을 대신하여 TDMC 순방향 모의 중에 이를 효율적으로 계산할 수 있는 몬테칼로 알고리즘을 개발하였다. 개발된 방법은 검증을 위해 2군 무한균질 문제에서 시간에 따른 동특성 인자를 평가하였으며 결과는 해석해와 잘 일치하였다. 또한 기존의 기여자 모의법과 성능을 비교했을 때 임계에 가까운 문제에서는 1,000배가 넘는 계산 효율을 보였다. 다음으로 계산된 시간중속 동특성 인자의 적용성을 확인하기 위해 이를 이용하여 일점운동방정식을 세우고 시스템의 과도상태 거동을 예측하였다. 일점운동해석은 초기 상태가 임계인 C5G7-TD 문제와 초기 상태가 미임계인 KUCA의 토륨장전 가속기 구동 시스템의 빔 트립 모의 실험에 대해 수행되었으며  $k$  고유치 계산과 고정 선원 계산, TDMC 계산으로 추정된 동특성 인자를 이용하여 서로 다른 일점운동방정식을 비교하였다. 개발된 방법은 시스템에 상관없이 정확한 중성자속 분포를 반영하여 동특성 인자를 계산할 수 있으며 기존의 정상상태를 기준으로 수행되던 일점운동해석을 일반화하여 임의의 상태를 기준으로

일점운동해석을 수행할 수 있는 해석 체계를 제공한다는 점에서 큰 의의가 있다.

마지막으로 열수력 변환 효과를 고려한 보다 실제적인 문제에 대한 과도해석능을 갖추기 위해 TCP/IP 소켓 통신을 이용하여 McCARD/CUPID 연계 과도해석 체계를 구축하였다. CUPID는 한국원자력연구원에서 개발한 3차원 부수로 코드로 이를 연계함으로써 부수로에서의 냉각재 섞임 효과를 고려한 과도상태 해석을 수행할 수 있다. 연계해석체계는 VERA 6번 고온전출력 집합체 문제에 대해 기존에 정상상태 해석을 위해 구축하였던 McCARD/MATRA 연계해석체계와 비교 검증하였으며, 정상상태에서 출력 분포는 0.17%, 냉각재 출구 온도는 0.06%, 핵연료 온도는 1.55%의 차이 이내에서 서로 잘 일치하였다. 과도 상태에서의 연계해석으로는 VERA 6번 문제를 수정하여 고온영출력 조건에서 간단한 제어봉 이탈사고를 가정하여 이를 해석하였다. 핵연료 온도와 출력변화로부터 핵연료 온도 변환에 의한 도플러 효과를 확인하였고 이를 통해 연계해석체계의 건전성을 확인하였다.

주요어:

시간종속 몬테칼로 중성자 수송해석법

펄스중성자선원 알파 계측

원자로 과도해석

진분산 추정

시간종속 동특성 인자 추정

열수력 연계 과도해석 체계

학번: 2014-21424